



Title	Plasma-Assisted Pulsed Laser Deposition of Carbon Nanomaterials
Author(s)	Suda, Yoshiyuki
Citation	北海道大学. 博士(工学) 乙第6441号
Issue Date	2006-03-24
DOI	10.14943/doctoral.r6441
Doc URL	<a href="http://hdl.handle.net/2115/32698">http://hdl.handle.net/2115/32698</a>
Type	theses (doctoral)
File Information	6441.pdf



[Instructions for use](#)

Plasma-Assisted Pulsed Laser Deposition of  
Carbon Nanomaterials

炭素ナノ材料のプラズマ支援パルスレーザ堆積

by

Yoshiyuki Suda

A dissertation submitted in partial fulfillment

of the requirements for the degree of

Doctor of Philosophy (Engineering)

in Hokkaido University

2006

Dissertation Supervisor

Professor **Yosuke Sakai**

## Abstract

Plasma-Assisted Pulsed Laser Deposition of Carbon Nanomaterials

by

Yoshiyuki Suda

Pulsed laser deposition (PLD) utilizes a laser ablation plume to fabricate various carbon nanomaterials, such as amorphous carbon (a-C), carbon nanotubes (CNTs) and carbon nanofibers (CNFs). In this study, amorphous carbon (a-C) thin films and nanometer-sized particles (nanoparticles) were prepared by pulsed laser deposition (PLD) assisted by radio frequency (RF) plasma (plasma-assisted PLD) and compared with those deposited by PLD without plasma. O<sub>2</sub> and Ar gases were used as ambient. The laser ablation plume was diagnosed by optical emission spectroscopy and its current waveform. The effect of plasma in plasma-assisted PLD on the properties of a-C films and nanoparticles was discussed.

For the case of Ar, experiments were carried out in Ar gas pressures  $p_{\text{Ar}}$  ranging from 1 to 1600 mTorr and RF input powers of 0–150 W. The film surfaces deposited were examined with scanning electron microscopy (SEM) and atomic force microscopy (AFM). In Ar plasma-assisted PLD, the number of micron-sized carbon droplets deposited on substrates was reduced as RF input power increased. This reduction was explained semiquantitatively by a model, in which the droplets are charged negatively in

the plasma and the electrostatic force due to a strong electric field in the plasma-sheath region prevents them from depositing on substrates. The size of a-C nanoparticles deposited in Ar plasma-assisted PLD and Ar gas PLD increased with  $p_{\text{Ar}}$ . The number density of nanoparticles in the Ar plasma-assisted PLD, which went through the aforementioned plasma-sheath region, was larger than that obtained in the Ar gas PLD. An X-ray photoelectron spectroscopy (XPS) showed that the nanoparticles were in an amorphous state. The  $\text{sp}^3/\text{sp}^2$  carbon ratio was 0.4 in the Ar gas and Ar plasma at  $p_{\text{Ar}} = 1$  mTorr and decreased monotonously as the particle size increased.

In  $\text{O}_2$  plasma-assisted PLD, a-C films were deposited at an oxygen pressure  $p_{\text{O}_2} = 0.4$  mTorr and compared with those deposited in vacuum and 0.4-mTorr  $\text{O}_2$  gas. The substrate temperature  $T_{\text{sub}}$  was varied between room temperature and  $480^\circ\text{C}$ . An XPS analysis evaluated that the highest  $\text{sp}^3$  content among the films deposited was 58% in  $\text{O}_2$  plasma-assisted PLD at  $T_{\text{sub}} = 410^\circ\text{C}$ . The etching of a-C films by  $\text{O}_2$  plasma was confirmed by optical emission spectroscopy. The film surface deposited under this condition was shown to be quite smooth with a roughness of about 5 nanometers, by SEM and AFM.

Multi-walled carbon nanotubes (CNTs) were synthesized inside a quartz tube operated at  $1000^\circ\text{C}$  by PLD. A graphite target containing 1 at. % Ni and minute quantities of Y was used as metal catalysts. SEM, transmission electron microscopy (TEM) and Raman spectroscopy analyses revealed that the CNTs grown were multi-walled structure



with diameters of 20–50 nm. Ni/Y nanoparticle was found in the CNTs by TEM observation; however, an energy dispersive X-ray analyser (EDX) measurement showed that the Ni content in the CNTs was lower than 0.1 at. %. Increase in the laser repetition rate effectively elongated CNTs.

Carbon nanofibers (CNFs) were grown on Ni- and Fe-coated SiO<sub>2</sub>/Si substrates in the same apparatus for CNTs. The CNFs grown were analysed by SEM. It is speculated that the CNFs grow out from the metal nanoparticle after laser-ablated carbon particles have been dissolved in it. In a range of oven temperatures between 800 and 1100°C, CNFs were grown at a temperature  $\geq 1000^{\circ}\text{C}$ . The thickness of the Ni film controlled the CNFs diameter.

Dedicated to my wife, Eri Suda,  
and to my parents, Eikichi Suda and Masako Suda  
to acknowledge their constant encouragement and enthusiasm.

## Acknowledgements

I would begin by thanking Professor Yosuke Sakai. His proactive personality always encouraged me. This work would not have been possible without his experience and intelligence.

I would also like to thank Professor Hirotake Sugawara for his deep knowledge about plasma electronics and encouragement. Thanks also to Dr. Maria-Antoaneta Bratescu at *n*-factory for sharing her experience in plasma spectroscopy, cheerfully. I would like to thank Dr. Cristian P. Lungu at National Institute for Lasers, Plasma and Radiation Physics, Romania and Dr. Costel Biloiu at West Virginia University, USA for making me a better experimentalist by accepting nothing but the best.

I would especially like to thank Prof. Kaoru Suzuki at Nihon University and Prof. Junji Nakamura at Tsukuba University for their discussions and suggestions. I would like to thank Prof. Zhifeng Ren at Boston College, USA for accepting my visit at Boston College for a month and half and fruitful discussion of carbon nanomaterials.

Thanks to Dr. Akinori Oda at Nagoya Institute of Technology, Dr. Soon-Youl So at Mokpo University, Korea, Dr. Satoshi Uchida at Tokyo Metropolitan University, Dr. Norio Homma at Hokkaido Electric Power Company, Dr. Kiyotaka Matsuura at Hokkaido Electric Power Company, Dr. Jiro Tsujino at Hokkaido Electric Power Company, Dr. Toshiki Mitsueda at Hokkaido Electric Power Company and Mr. Osamu Shiono at Hokkaido Electric Power Company for their constant encouragement and

experimental support.

I would deeply like to thank my students, Mr. Takuma Nishimura, Mr. Katsumi Itoh, Mr. Manabu Mizuno, Mr. Tomoyuki Ono, Mr. Ken Tomita, Mr. Yuya Suganuma, Mr. Kohji Utaka, Mr. Atsushi Okita, Mr. Takeshi Kojima, Mr. Akihide Tanaka, Mr. Yuki Hayakawa, Mr. Atsushi Ozeki and Mr. Takeshi Saito for their persistent efforts and ambition. I have had much to learn from guidance.

This study was supported in part by 21<sup>st</sup> century COE program, “Meme-Media Technology Approach to the R&D of Next-Generation Information Technologies” and grant-in-aids for scientific research (11750245 and 16760240) by MEXT, the Inamori foundation, Nissan science foundation and Research Foundation for the Electrotechnology of Chubu.

# Contents

<b>Dedication .....</b>	v
<b>Acknowledgements .....</b>	vi
<b>List of Figures .....</b>	xi
<b>List of Tables .....</b>	xviii
<b>Chapter 1 Introduction .....</b>	1
1.1 History and Fundamentals of Pulsed Laser Deposition (PLD) .....	1
1.2 Pulsed Laser Deposition of Amorphous Carbon (a-C) Films, Carbon Nanotubes and Nanofibers .....	5
1.3 Purpose of This Study and Synopsis of Each Chapter .....	10
<b>Chapter 2 Experimental .....</b>	12
2.1 Plasma-Assisted Pulsed Laser Deposition (PAPLD) System .....	12
2.1.1 Experimental Setup .....	12
2.1.2 Experimental Procedure .....	14
2.2 Carbon Nanotube / Nanofiber Growth System .....	16
2.2.1 Experimental Setup .....	16
2.2.2 Experimental Procedure .....	17
2.3 Lasers .....	19
2.3.1 Lasers for PLD work .....	19
2.3.2 Excimer Basics .....	20
2.4 Characterization of Ablation Plume and Carbon Nanomaterials.....	23
2.4.1 Diagnostics of Ablation Plume .....	23
2.4.2 Surface Morphology .....	23
2.4.3 Chemical Composition and Bonding State .....	23
<b>Chapter 3 Diagnostic of Laser Ablation Plume .....</b>	25
3.1 Observation of Carbon Ablation Plume .....	25
3.2 Current Waveform of Carbon Ablation Plume .....	26

3.3 Optical Emission Spectra of Carbon Ablation Plume .....	31
3.4 Evaluation of Electron Temperature .....	36
<b>Chapter 4 Syntheses and Analyses of Carbon Nanoparticles and</b>	
<b>Thin Films by PAPLD .....</b>	<b>39</b>
4.1 Deposition of a-C Films .....	39
4.1.1 Thickness of a-C Films on the Number of Laser Shots .....	39
4.1.2 Spatial Distribution of a-C Film Thickness .....	40
4.2 Surface Morphology of a-C Films and Nanoparticles .....	43
4.2.1 Obtained by PLD in Ar Gas .....	43
4.2.1.1 SEM Analysis of a-C Film Surfaces .....	43
4.2.1.2 AFM Analysis of a-C Film Surfaces .....	48
4.2.2 Obtained by Ar PAPLD .....	50
4.2.2.1 SEM Analysis of a-C Film Surfaces .....	50
4.2.2.2 AFM Analysis of a-C Film Surfaces .....	53
4.3 Comparison between Ar Gas PLD and Ar PAPLD in the Formation of a-C Nanoparticles .....	57
4.3.1 Formation of a-C Nanoparticles at Relatively High Ar Gas Pressures ( $p_{\text{Ar}} \geq 400$ mTorr) .....	57
4.3.2 Formation of a-C Nanoparticles at Relatively Low Ar Gas Pressures ( $p_{\text{Ar}} \leq 100$ mTorr) .....	59
4.3.3 Growth Model of a-C Nanoparticles by PAPLD .....	62
4.4 Reduction of Micron-Sized Carbon Droplets on substrates by PAPLD ....	64
4.4.1 Generation and Deposition of Droplets .....	64
4.4.2 Effect of RF Ar and O <sub>2</sub> Plasma on Reduction of Droplet Number Density on Substrates .....	65
4.4.3 Mechanism Droplet Reduction by PAPLD .....	70
4.5 XPS Analysis of a-C Nanoparticles and Films.....	76

4.5.1. XPS Analysis .....	76
4.5.2 Model for Deposition of a-C Nanoparticles and Films by PAPLD.....	78
4.5.3. Correlation between the AFM and XPS Results .....	80
4.6 Deposition of a-C Films by O <sub>2</sub> PAPLD .....	81
4.6.1 AFM Analysis of a-C Films .....	81
4.6.2 Raman Spectroscopy of a-C Films .....	83
4.6.3 XPS analysis of a-C films.....	85
4.6.4. Mechanism of a-C Film Deposition by O <sub>2</sub> PAPLD .....	88
<b>Chapter 5 Syntheses of Carbon Nanotubes (CNTs) and Nanofibers (CNFs)</b>	
<b>by PLD.....</b>	94
5.1 Growth of CNTs in a laser oven apparatus .....	94
5.1.1 Observation of CNTs by SEM and TEM .....	94
5.1.2 EDX analysis of CNTs .....	96
5.1.3 Difference in Ablation Lasers and Laser Fluences .....	98
5.1.4 Raman Spectroscopy .....	99
5.1.5 Effect of Laser Repetition Rate on CNT Length .....	100
5.2 CNF Growth on Metal-Catalyzed Substrates.....	102
5.2.1 Observation of CNFs by SEM and TEM .....	102
5.2.2 Optical Emission Spectroscopy of Ablation Plume of Ni/Y/C Target.....	107
<b>Chapter 6 Conclusion .....</b>	109
<b>Author's Publications Related to the Present Work .....</b>	112
<b>Bibliography .....</b>	113

## List of Figures

Figure 1.1. Evolution of laser technology and its applications.

Figure 1.2. Schematic diagram of a pulsed laser deposition apparatus.

Figure 1.3. Ternary phase diagram of amorphous carbons. The three corners correspond to diamond, graphite, and hydrocarbons, respectively.

Figure 1.4. Schematic models for single-wall carbon nanotubes with the nanotube axis normal to the chiral vector. The nanotubes are categorized into three types: (a) an “armchair” nanotube; (b) a “zigzag” nanotube and (c) a “chiral” nanotube.

Figure 2.1. Schematic diagram of plasma-assisted pulsed laser deposition system.

Figure 2.2. A photograph of RF plasma in a 500-mTorr Ar gas.

Figure 2.3. SEM micrographs of the graphite target surface: (a) laser-ablated and (b) after the treatment with an abrasive paper and cotton.

Figure 2.4. Schematic diagram of carbon nanotube / nanofiber growth system.

Figure 2.5. Schematic diagram of the electronic potential of the KrF excimer.

Figure 3.1. Photographs of carbon ablation plume in (a) vacuum and (b-c) Ar gas. The exposure time was 2 sec. The laser repetition rate was (a) 20 Hz and (b-c) 1 Hz. The laser fluence was  $3.5 \text{ J/cm}^2$ .

Figure 3.2. Measuring electrical circuit for the current waveform.

Figure 3.3. Current waveforms of carbon ablation plume: (a) “fast” waveform and (b) “slow” one.



Figure 3.4. The velocity of (a) electrons and (b) positive ions.

Figure 3.5. Charges of (a) electrons and (b) positive ions estimated by the current waveforms.

Figure 3.6. Current waveforms of carbon ablation plumes under (a) positive and (b) negative biases.

Figure 3.7. The optical emission spectra of carbon ablation plume in vacuum: (a) UV wavelength region; (b) visible wavelength region (PMA exposure time = 19 ms, laser fluence =  $4 \text{ J/cm}^2$ , repetition rate = 1 Hz).

Figure 3.8. The optical emission spectra of carbon ablation plume in Ar gas at  $p_{\text{Ar}} = 1 \text{ Torr}$ . The laser fluence and repetition rate were  $4 \text{ J/cm}^2$  and 1 Hz, respectively.

Figure 3.9. The optical emission spectra of carbon ablation plume in a 0.5-Torr He gas. The laser fluence and repetition rate were  $4 \text{ J/cm}^2$  and 1 Hz, respectively.

Figure 3.10. The optical emission spectra of carbon ablation plume in RF Ar plasma at  $p_{\text{Ar}} = 1 \text{ Torr}$  in a wavelength range of (a) 300–800 nm and (b) 300–650 nm.

Figure 3.11. (a) An example of energy diagram for calculating electron temperature  $T_e$ . (b) A demonstration of  $T_e$  evaluation. (c) The energy diagram of C II transition.

Figure 3.12. Dependence of  $T_e$  of carbon ablation plume on (a) the laser fluence, (b) distance from the target and (c) Ar gas pressure. (a)  $p_{\text{Ar}} = 0.5 \text{ Torr}$ , (b)  $p_{\text{He}} = 760 \text{ Torr}$  and (c) RF input power < 10 W.

Figure 4.1. Thicknesses of a-C films deposited in vacuum at  $T_{\text{sub}}=20^\circ\text{C}$  vs. number of laser shots. The laser fluence and  $d_{\text{st}}$  was  $2.1 \text{ J/cm}^2$  and 35 mm, respectively.

Figure 4.2. Substrate configuration for measuring the spatial distribution of a-C film thickness along the direction of LA plume (z axis).

Figure 4.3. (a) A photograph of the a-C film deposited on Si substrate in a 10-mTorr Ar gas. (b) Spatial distribution of the thickness of film (a). (c) Thicknesses of the a-C films deposited at  $p_{Ar} = 10$  (■) and 60 mTorr (●) on z-axis. The laser fluence and repetition rate were  $3.2 \text{ J/cm}^2$  and 10 Hz, respectively. The film thickness was measured by ellipsometry under the assumption that the refractive index  $n$  of films is 2.4.

Figure 4.4. Low-magnification ( $\times 250$ ) SEM micrographs of the a-C film surfaces deposited at  $p_{Ar} = 0 - 1600$  mTorr. The laser fluence and repetition rate were  $4 \text{ J/cm}^2$  and 30 Hz, respectively. The deposition time was 30 min.

Figure 4.5. High-magnification ( $\times 5,000 - \times 60,000$ ) SEM micrographs of the a-C films shown in Figure 4.4.

Figure 4.6. Number density of the particles deposited on substrates vs.  $p_{Ar}$ .

Figure 4.7. Histograms of the a-C particle size deposited on substrates.

Figure 4.8. AFM images of a-C nanoparticles deposited on substrates.

Figure 4.9. Low-magnification ( $\times 250$ ) SEM micrographs of a-C nanoparticles obtained in Ar PAPLD.

Figure 4.10. High-magnification ( $\times 25,000 - \times 80,000$ ) SEM micrographs of the particles shown in Figure 4.9. Figure 4.10 (c) was taken from a  $45^\circ$ .

Figure 4.11. Dependence of the number density of a-C nanoparticles on  $p_{Ar}$ : obtained in Ar gas (●) and plasma (●).

Figure 4.12. Histograms of the a-C nanoparticle size deposited on substrates at  $p_{Ar} = 1.5 - 1600$  mTorr.

Figure 4.13. AFM images of a-C nanoparticles obtained in Ar PAPLD at  $p_{\text{Ar}} = 1 - 100$  mTorr.  $d_{\text{st}} = 20$  mm.

Figure 4.14. AFM images of a-C nanoparticles obtained in Ar PAPLD at  $p_{\text{Ar}} = 1$  mTorr. The RF input power and  $d_{\text{st}}$  was respectively varied in a range of 20 – 100 W and 20 – 40 mm.

Figure 4.15. (a) An AFM image of a-C nanoparticles obtained in a 10-mTorr Ar plasma. A solid line cuts out the two particles for measuring its sectional view. (b) Sectional view of the particles.

Figure 4.16. (a) Radius ( $r$ ) and height ( $h$ ) of the a-C nanoparticles. (b) Number density of the particles vs. RF input power.

Figure 4.17. SEM micrographs of a-C nanoparticles obtained in (a) Ar gas and (b) Ar plasma at  $p_{\text{Ar}} = 400$  mTorr.  $d_{\text{st}} = 20$  mm. Figures (a2) and (b2) were taken at an angle of  $45^\circ$  from the substrate.

Figure 4.18. Histograms of the a-C nanoparticle size obtained in (a) Ar gas and (b) Ar plasma at  $p_{\text{Ar}} = 400$  mTorr. The RF input power was 60 W.

Figure 4.19. AFM images of the a-C thin film surface obtained in (a) Ar gas and (b) Ar plasma at  $p_{\text{Ar}} = 1$  (left) and 100 mTorr (right).

Figure 4.20.  $r$  of the a-C nanoparticles in the Ar gas (●) and plasma (●). The solid lines represent a curve fit.

Figure 4.21. An illustration of aggregation model for nanoparticle growth in  $\text{SiH}_4$  plasma [60].  $n_d$  and  $n_e$  denote particulate and electron densities, respectively.

Figure 4.22. SEM images of a-C thin film deposited in vacuum.

Figure 4.23. Low-magnification ( $\times 250$ ) SEM micrographs of a-C films deposited in a 30-mTorr Ar plasma. The RF input power was varied from 0 to 60 W.

Figure 4.24. High-magnification ( $\times 2,500$ ) SEM micrographs of Figure 4.23.

Figure 4.25. Number density of droplets deposited in 30-mTorr Ar plasmas vs. RF input power. The droplets with a diameter  $\geq 1 \mu\text{m}$  were counted, and the number density was evaluated by division of each film thickness.

Figure 4.26. SEM micrographs of the a-C film surfaces deposited in (a) vacuum, (b)  $\text{O}_2$  gas and (c)  $\text{O}_2$  plasma. The experimental results are detailed in Section 4.6.

Figure 4.27. AFM image of the film shown in Figure 4.26 (c).

Figure 4.28. Sputtering yield as a function of Ar ion incident energy [J. Ullmann, G. Schmidt, and W. Scharff, Thin Solid Films, 214 (1992) 35-43].

Figure 4.29. An illustration of behavior of negatively charged particles in PAPLD.

Figure 4.30. C (1s) XPS spectra of a-C films deposited in (a) Ar gas and (b) Ar plasma.

Figure 4.31. An example of the deconvolution of C (1s) spectra by  $\text{sp}^2$ ,  $\text{sp}^3$  and carbon oxide components.

Figure 4.32. The  $\text{sp}^3/\text{sp}^2$  ratio of the a-C nanoparticles and films deposited in Ar gas ( $\odot$ ), Ar plasma ( $\bullet$ ), and vacuum ( $\ominus$ ).

Figure 4.33. The  $\text{sp}^3/\text{sp}^2$  ratio of the a-C nanoparticles as a function of the nanoparticle radius: obtained in the Ar gas ( $\odot$ ) and Ar plasma ( $\bullet$ ).

Figure 4.34. AFM images of the a-C films deposited in (a) vacuum, (b)  $\text{O}_2$  gas, and (c)  $\text{O}_2$  plasma at  $T_{\text{sub}} \sim 400^\circ\text{C}$ . The  $\text{O}_2$  gas pressure,  $p_{\text{O}_2}$  was 0.4 mTorr.

Figure 4.35. Raman spectra of the a-C films deposited in (a) vacuum, (b)  $\text{O}_2$  gas and (c)  $\text{O}_2$  plasma at  $T_{\text{sub}}$  between  $25^\circ\text{C}$  and  $480^\circ\text{C}$ .

Figure 4.36. C (1s) XPS spectra of the a-C films deposited in (a) vacuum, (b) O<sub>2</sub> gas and (c) O<sub>2</sub> plasma.

Figure 4.37. (a) sp<sup>3</sup> and (b) sp<sup>2</sup> contents as a function of  $T_{\text{sub}}$ .

Figure 4.38. Formation process of sp<sup>3</sup> and sp<sup>2</sup> bonds in a-C films explained by sub-plantation model [15].

Figure 4.39. Variation of the sp<sup>3</sup> content of the a-C films deposited at 25°C, as a function of laser fluence [86].

Figure 4.40. Optical emission spectra of the graphite target surface in O<sub>2</sub> plasma: (a) without and (b) with laser ablation.

Figure 4.41. Deposition rate of a-C films deposited in (a) vacuum, (b) O<sub>2</sub> gas and (c) O<sub>2</sub> plasma as a function of  $T_{\text{sub}}$ .

Figure 5.1. Micrographs of the CNTs deposited in area (3) by (a) SEM, (b) and (c) TEM. Ar gas flow rate and laser repetition rate were 750 sccm and 10 Hz, respectively.

Figure 5.2. TEM micrograph of CNTs. The white arrow indicates a catalyst particle.

Figure 5.3. SEM micrographs of the surfaces of Ni/Y/C target: (a) before and (b) after LA at a repetition rate of 10 Hz for 120 minutes.

Figure 5.4. Raman spectra of the CNTs synthesized at different Ar gas flow rates. The laser repetition rate was 10 Hz.

Figure 5.5. TEM micrographs of the CNTs deposited at a laser repetition rate of 50 Hz in two different areas, (a) area (3) and (b) area (5), where  $T$  is 1000°C and ~800°C, respectively.

Figure 5.6. SEM micrographs of the CNFs grown on (a) Ni/SiO<sub>2</sub>/Si and (b) Fe/SiO<sub>2</sub>/Si substrates. (a2) backscattered electron image of (a1). The thicknesses of Ni and Fe films are 350 nm and 300 nm, respectively. The Ni/Y/C target was used.

Figure 5.7. TEM micrograph of CNFs grown from Pd/Ni catalyst.

Figure 5.8. Dependence of CNF diameter on Ni film thickness.

Figure 5.9. Optical emission spectra of the laser ablation plume of Ni/Y/C target in Ar gas at a pressure range of 0 – 600 Torr at  $T = \text{RT}$  and 1000°C.

## **List of Tables**

Table 2.1. Excimer laser operating wavelength.

Table 2.2. The specification of the ArF excimer laser used in this study.

Table 3.1. The experimental condition for measuring the current waveform.

Table 4.1. The experimental conditions taken throughout Chapter 4.

Table 4.2. Tidemarks of droplets of 100 nm – 10  $\mu$ m in diameter with an initial velocity = 5 – 100 m/s. The colored area represents that droplet stops prior to reaching the substrate.

Table 5.1. The experimental condition for CNT growth.

Table 5.2. EDX analyses of CNTs as shown in Figures 5.1 (b) and 5.2.

Table 5.3. The experimental condition for CNF growth.

# Chapter 1

## Introduction

### 1.1 History and Fundamentals of Pulsed Laser Deposition (PLD)

The laser, as a source of “pure” energy, increases popularity in broad applications. In many areas, such as metallurgy, medical technology, and electronics industry, the laser has become an irreplaceable tool. In material science, lasers also play a significant role either as a passive component for process monitoring or as an active tool by coupling its radiation energy into the material being processed, leading to various applications such as localized melting during optical fiber pulling, laser annealing of semiconductors, surface cleaning by desorption and ablation, laser-induced rapid quench to improve surface hardening, and most recently, pulsed laser deposition (PLD) for growing thin films.

Figure 1.1 illustrates the history of the development of laser technology from its initial discovery to current practical applications. In this tree of evolution, PLD is only a small branch that remained relatively obscure for a long time. This branch has started to blossom in the last dozen years or so.

Conceptually and experimentally, PLD is extremely simple, probably the simplest among all thin film growth techniques. Figure 1.2 shows a schematic diagram of an experimental setup. It consists of a target holder and a substrate holder housed in a



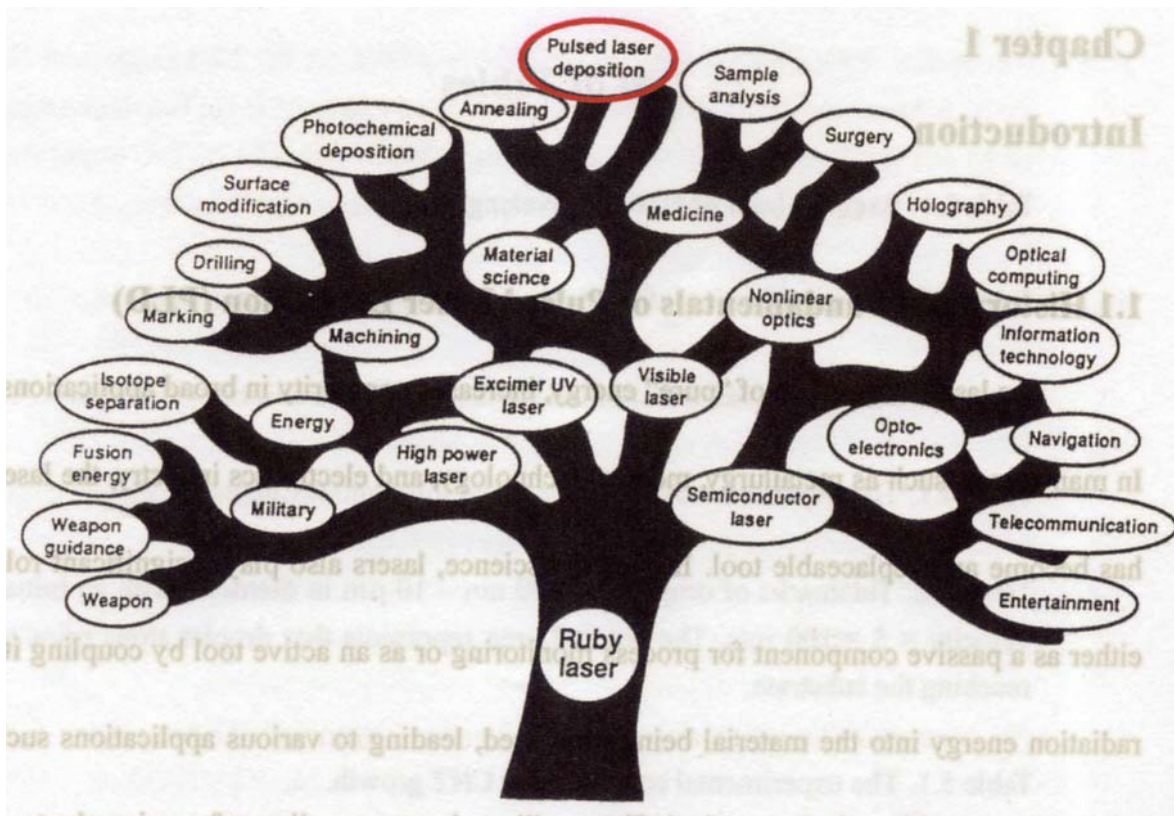


Figure 1.1. Evolution of laser technology and its applications [1].

vacuum chamber. A high-power laser is used as an external energy source to vaporize materials and to deposit thin films. A set of optical components is used to focus and raster the laser beam over the target surface. Film growth can be carried out in a reactive environment containing any kind of gas with or without plasma excitation. It can also be operated in conjunction with other types of evaporation sources in a hybrid approach.

In contrast to the simplicity of the hardware, the laser-target interaction is a very complex physical phenomenon. The mechanism that leads to material ablation depends on laser characteristics, as well as the optical, topological, and thermodynamical properties of the target. When the laser irradiation is absorbed by a solid surface,

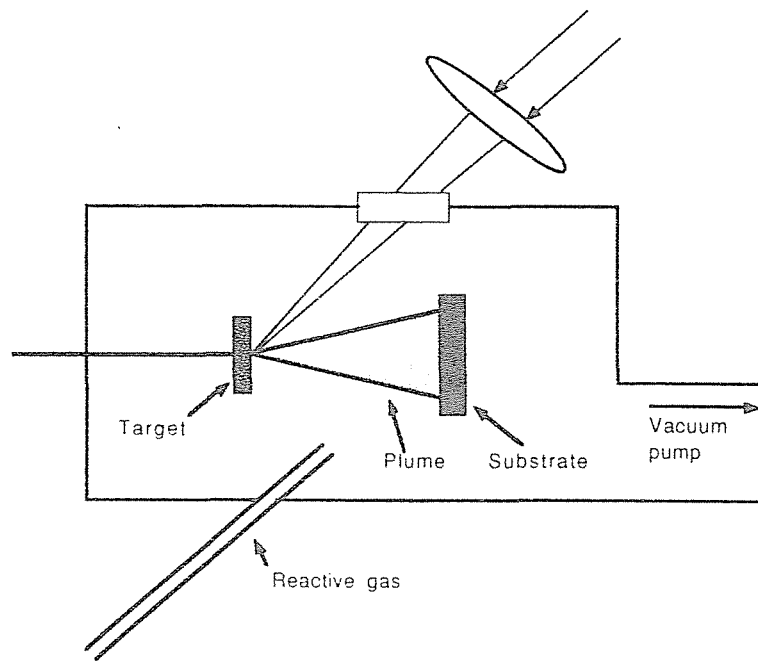


Figure 1.2. Schematic diagram of a pulsed laser deposition apparatus [1].

electromagnetic energy is converted first into electronic excitation and then into thermal, chemical, and even mechanical energy to cause evaporation, ablation, excitation, plasma formation, and exfoliation. This process is called as laser ablation. Evaporants form a “plume” consisting of a mixture of energetic species including atoms, molecules, electrons, ions, clusters and micron-sized droplets. The collisional mean free path inside the dense plume is very short. As a result, immediately after the laser irradiation, the plume rapidly expands into the vacuum from the target surface to form a nozzle jet with hydrodynamic flow characteristics. This process attributes to many advantages as well as disadvantages. The advantages are flexibility, fast response, energetic evaporants, and congruent evaporation. The disadvantages are the presence of micron-sized droplets, and

the narrow forward angular distribution that makes large area scale-up a very difficult task.

This technique has been used in a wide area of material science without a common name and acronym for a long time. The name, pulsed laser deposition (PLD), was designed by official voting from the participants of the first Material Research Society Symposium on Pulsed Laser Ablation held in San Francisco in April 1989. Based on the need of rising interest, commercial PLD systems and components have also reached the market. In order to incorporate this technique into the main stream of solid-state-device technology, the feasibility of large-area scale-up was demonstrated by beam scanning and by substrate scanning.

The success of in situ growth of high-temperature superconducting films by PLD brought an overwhelming interest to this field [2]. PLD has even been applied to the synthesis of buckminster fullerenes (i.e.,  $C_{60}$ ) [3, 4] and  $\beta$ - $C_3N_4$  films [5]. The total number of publications in PLD since 1987 is more than 10 times the combined publications in the past 25 years.

In PLD, because of the fast and very directional plume, attenuation due to trajectory change as a result of collisions with the background is small. Consequently, the pressure of the reactive gas during the film growth can be as high as 1 Torr, which is at least an order of magnitude higher than any other physical vapor deposition technique.

“Splashing” which denotes the generation and deposition of micron-sized

droplets, is considered to be one of the two major drawbacks of PLD. The other one is the lack of uniformity over a large area due to narrow angular distribution of the plume. The large area scale-up has many engineering solutions by rastering the laser or the substrate using rotation and translation. Splashing, however, is an intrinsic problem, therefore it is much more difficult to overcome. It is particularly problematic for electronic device quality semiconductor films and optical films where the droplets can induce the formation of defects and scattering centers that lower carriers' mobility, shorten the minority lifetime, and downgrade the damage threshold of optical films. The occurrence of splashing has many origins: subsurface boiling; expulsion of the liquid layer by the shock wave recoil pressure; exfoliation. For more than 20 years, numerous attempts were made to improve the film morphology by reducing or completely eliminating splashing [1].

## **1.2 Pulsed Laser Deposition of Amorphous Carbon (a-C) Films, Carbon Nanotubes and Nanofibers**

Elemental carbon has the ability to form a wealth of noncrystalline solids with a variety of properties. The great versatility of carbon materials arises from the strong dependence of their physical properties on the ratio of  $sp^2$  (graphitelike) to  $sp^3$  (diamondlike) bonds [6]. There are many forms of  $sp^2$ -bonded carbons with various degrees of graphitic ordering, ranging from microcrystalline graphite to glassy carbon. In

general, an amorphous carbon can have any mixture of  $sp^3$ ,  $sp^2$ , and even  $sp^1$  sites, with the possible presence of up to 60 at.% hydrogen. The compositions are conveniently shown on the ternary phase diagram, Figure 1.3.

Diamondlike carbon (DLC) is defined on this diagram as amorphous carbon with a significant fraction of  $sp^3$  bonds. The hydrogenated amorphous carbons (a-C: H) have a rather small C-C  $sp^3$  content. DLC's with higher  $sp^3$  content are termed tetrahedral amorphous carbon (ta-C) and its hydrogenated analog ta-C: H. Another crucial parameter is the degree of clustering of the  $sp^2$  phase, which should be added as a fourth dimension in the ternary phase diagram. Amorphous carbons with the same  $sp^3$  and H content show different optical, electronic, and mechanical properties according to the clustering of the  $sp^2$  phase.

Amorphous carbon films produced by PLD at room temperature have actually showed very good physical properties, e.g. high hardness, high electrical resistivity, high thermal conductivity, and high optical transparency [8, 9] and then expected to be applied in various fields of industrial applications, such as field electron emitters, surface coatings and tribological materials [10-17]. In plasma-enhanced chemical vapor deposition (PECVD) of a-C films, atomic oxygen generated by electron impact dissociation is known to remove the nondiamond component and hence to cause selective diamond component growth [18-20]. In PLD, as well, when oxygen is introduced into a reactor, excited atomic oxygen enhances diamond formation [21, 22].

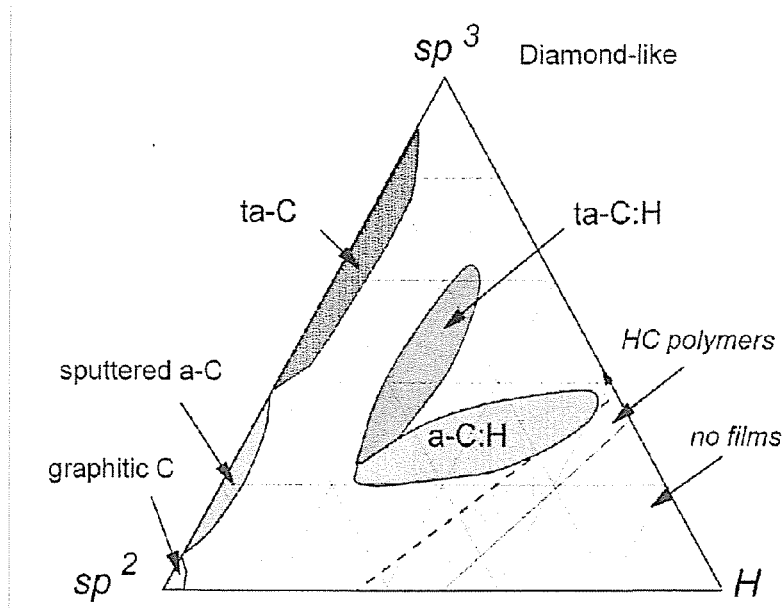


Figure 1.3. Ternary phase diagram of amorphous carbons. The three corners correspond to diamond, graphite, and hydrocarbons, respectively [7].

PLD in rare gases have been used for nanometer-size particle (nanoparticle) preparation, multi-component thin film deposition and carbon nanotube syntheses [23-27]. As a result of frequent collisions of ablated particles with gas atoms in plume, the particles cool down and form nanoparticles [23, 24]. Nanoparticle size was controlled by varying ambient gas pressure [24]. These nanoparticles are of interest for various fields of device applications, for example, silicon and gallium nitride nanoparticles for luminescent devices [23, 28]. The wavelength of the PL was shortened as their size decreased [23].

Recently, carbon nanoparticles have shown the remarkable performance in microelectronics and nonlinear optics [29, 30]. Experimental techniques such as sol-gel

method [29], chemical vapor deposition (CVD) [30] and pulsed laser deposition [31,32] were used to grow carbon nanoparticles. PLD has advantages in generating energetic species without any chemical contamination and convenience in operation [1]. During the PLD process, background pressure and substrate temperature affect nanoparticle growth and carbon bonding.

Carbon nanotubes (CNTs) were discovered by Iijima of the NEC Laboratory, Tsukuba, Japan in carbon soot deposited on graphite electrode of arc discharge [33, 34]. The structure of CNTs has been explored early on by high-resolution transmission electron microscopy (TEM) and scanning tunneling microscopy (STM) techniques [35], yielding direct confirmation that the nanotubes are seamless cylinders derived from the honeycomb lattice representing a single atomic layer of crystalline graphite, called a graphene sheet. Figure 1.4 shows schematic models for single-wall carbon nanotubes [36]. Since CNTs have excellent physical and electronic properties, such as field emission property, high electrical conductivity and high tensile strength, they have been widely studied for various applications to field electron emitters, scanning probes and electronic devices [36]. Several techniques, laser ablation [26, 27], arc discharge [37] and chemical vapor deposition (CVD) [38], have been developed for the production of single-walled CNTs (SWNTs). Laser ablation of metal-catalyzed graphite is known to synthesize highly crystallized single-wall CNTs in gas phase with high yield [27].

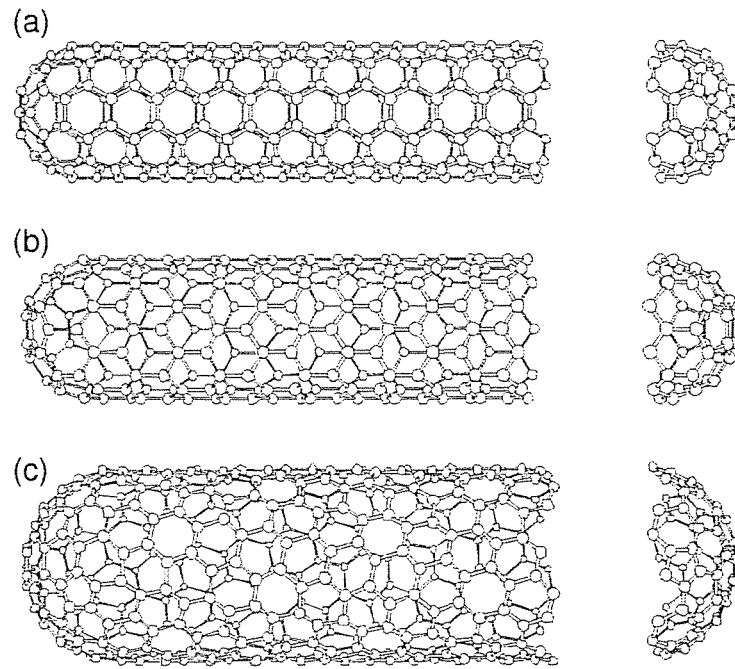


Figure 1.4. Schematic models for single-wall carbon nanotubes with the nanotube axis normal to the chiral vector. The nanotubes are categorized into three types: (a) an “armchair” nanotube; (b) a “zigzag” nanotube and (c) a “chiral” nanotube [36].

Recently, carbon nanofibers (CNFs) have been also recognized as a nanometer-sized carbon material. Very small diameter (less than 10 nm) carbon filaments were prepared in the 1970’s and 1980’s through the synthesis of vapor grown carbon fibers by the decomposition of hydrocarbons at high temperatures in the presence of transition metal catalyst particles  $< 10$  nm diameter [39-43]. However, no detailed systematic studies of such very thin filaments were reported in these early years [36]. CNFs are promising materials, and are expected to be applied to field-emission electron sources, intercellular gene delivery devices and nanoporous membranes [44].



### 1.3 Purpose of This Study and Synopsis of Each Chapter

The purpose of this study is to synthesis carbon nanomaterials, such as amorphous carbon (a-C) thin films, a-C nanoparticles, CNTs and CNFs by gas-phase and plasma-assisted PLD, and to evaluate how plasma affects their growth kinetics and properties. In order to achieve the goals the following were performed:

- (1) The effect of RF Ar plasma on the growth kinetics of carbon nanoparticles was examined. The size and bonding states of the nanoparticles were analyzed with atomic force microscopy (AFM) and X-ray photoelectron spectroscopy (XPS).
- (2) Reduction of micrometer-sized carbon droplets, which deteriorate the quality of film deposited, was examined by the plasma-assisted PLD. The number density of droplets was analyzed with SEM.
- (3) O<sub>2</sub> plasma-assisted PLD of a-C films was carried out and the sp<sup>3</sup> content in the films were evaluated by XPS.
- (4) Carbon nanotubes were grown by PLD using ArF excimer laser ( $\lambda=193$  nm) in an electric furnace. The CNTs grown were analyzed with transmission electron microscopy (TEM) and Raman spectroscopy.
- (5) Laser-thermal chemical vapor deposition (LTCVD) technique was studied for CNF growth. LTCVD is a combination of PLD and CVD. The CNFs grown were analyzed with SEM and TEM.

The dissertation contains six chapters. In chapter 1, the background of PLD and purpose of this study are presented. In chapter 2, the experimental configurations used in this study are presented. In chapter 3, the diagnostics of laser ablation plume by current waveform and optical emission spectroscopy are presented. In chapter 4, the deposition of a-C films and nanoparticles by gas-phase and plasma-assisted PLD and their properties are presented. In chapter 5, syntheses of CNTs and CNFs by PLD are presented. In chapter 6, this study is summarized.

## Chapter 2

### Experimental

#### 2.1 Plasma-Assisted Pulsed Laser Deposition (PAPLD) System

##### 2.1.1 Experimental Setup

Figure 2.1 shows a schematic diagram of plasma-assisted PLD (PAPLD) system (Pascal Co. Ltd.). The PAPLD chamber is 350 mm in diameter and 600 mm in height and contains a substrate and six target holders. The target holders are surrounded by a gold-coated coil with a diameter of 113 mm and a height of 25 mm. The chamber is evacuated by a turbo molecular pump followed by a rotary pump up to  $2.0 \times 10^{-8}$  Torr. When an RF ( $f = 13.56$  MHz) power is input to the coil, plasma is generated as shown in Figure 2.2. An infrared lamp is mounted behind the substrate holder and controls the substrate temperature ranging from room temperature to 800°C. A shutter, which is introduced between the substrate and targets, collects electric charges in a plume as well as intercepts a laser ablation plume.

An ArF excimer laser (LAMBDA PHYSIK Co., Ltd., COMpex 205; wavelength = 193 nm; pulse duration = 20 ns; repetition rate = 1–50 Hz; and maximum pulse energy = 400 mJ) was used in this study. The discharge tube of laser was filled with Ar (purity = 99.999%), F<sub>2</sub> (5% diluted with He) and Ne (purity = 99.999%) gases once a week for maintaining high laser energy. The laser beam was reflected by two multilayered

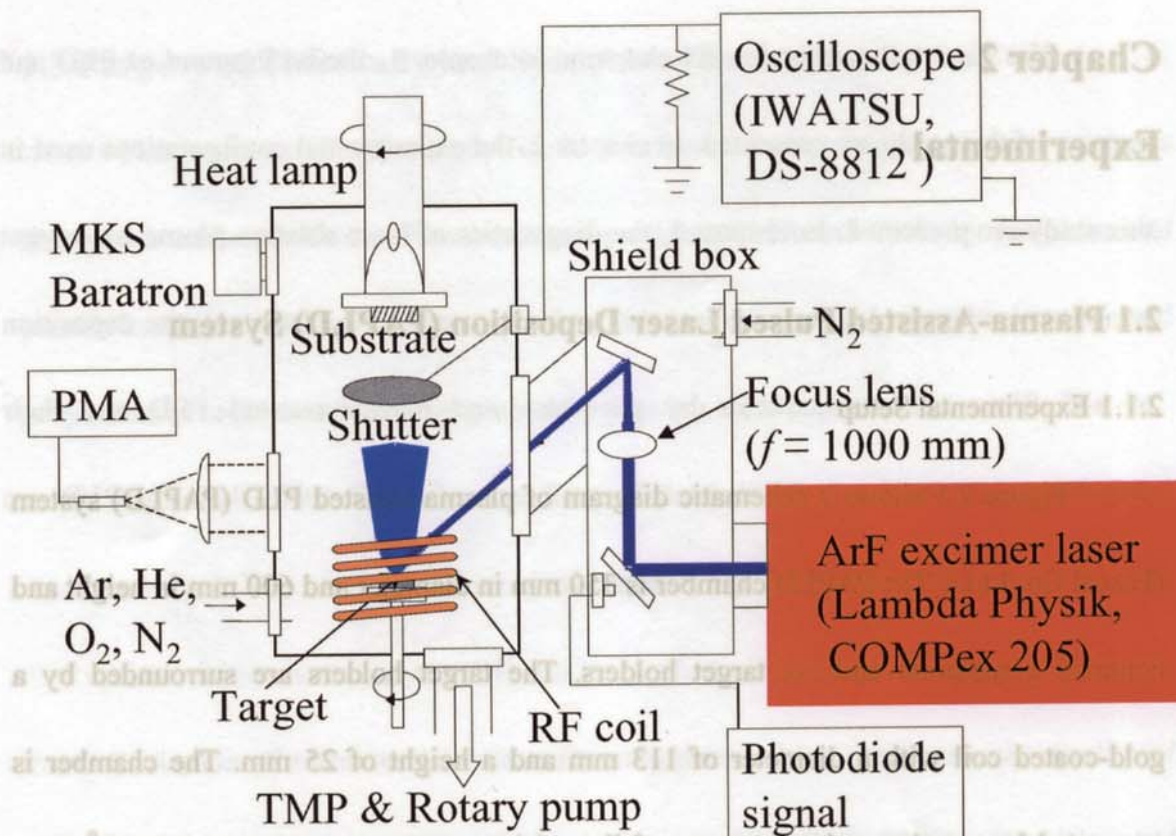


Figure 2.1. Schematic diagram of plasma-assisted pulsed laser deposition system.



Figure 2.2. A photograph of RF plasma and a laser ablation plume at an Ar gas pressure of 500 mTorr.

dielectric mirrors (CVI Laser, LLC) and irradiated onto a sintered graphite target at an incident angle of  $37^\circ$ . A plane-convex lens (focal length =  $\sim 800$  mm) or two cylindrical lenses (focal length = 381.4 and 203.4 mm) were used for focusing. Dimension of the focused laser beam was  $1\text{ mm} \times 5\text{ mm}$  for a plane-convex lens and  $1\text{ mm} \times 3\text{ mm}$  for two cylindrical ones. The laser energy was measured by a pyrometer, and the fluence ( $\text{J}/\text{cm}^2$ ) was evaluated. The laser energy at the target was reduced down to  $\sim 50\%$  from that at the laser beam window due to the reflectivity of mirrors and the absorption loss by oxygen molecules in the air.

A sintered graphite target (Kojundo Chemical Laboratory Co., Ltd.; Furuuchi Chemical Corp., 20 mm in diameter and 5 mm in thickness, purity = 99.999%) and n-type Si (100) substrate were used. The substrate and target holders were respectively rotated at  $\sim 10$  rpm and  $\sim 25$  rpm. The distance between the substrate and target  $d_{\text{st}}$  was changed between 20 and 35 mm. High-purity gases ( $\text{Ar} = 99.999\%$ ;  $\text{O}_2 = 99.999\%$ ;  $\text{He} = 99.9999\%$ ; and  $\text{N}_2 = 99.999\%$ ) were used as an ambient gas and introduced through mass flow controllers. The gas pressure was measured with a MKS Baratron<sup>®</sup> Capacitance Manometer.

### 2.1.2 Experimental Procedure

The experiment was performed as the following procedure.

#### (1) Cleaning of Si substrate

A Si substrate (approx. 10-mm-square) was cleaned with acetone and then ethanol using an ultrasonic cleaner. After blowing off the ethanol, the substrate was immersed in a solution of hydrofluoric acid for ~1 min to eliminate a native-oxide layer on Si. Then, the substrate was rinsed with extra-pure water and dried.

## (2) Preparation of graphite target

In PLD, target surface becomes bumpy as it is ablated for a while (see Figure 2.3 (a)). To keep ablation plume constant, the following preparation of targets were performed prior to experiment: the target surface was first polished with an abrasive paper and cotton, then rinsed by acetone in an ultrasonic cleaner and dried.

## (3) PLD experiment

After introducing a substrate and targets, the chamber was evacuated up to the base pressure ( $< 10^{-7}$  Torr) for several hours. The excimer laser was warmed up at a “high voltage” of 25 kV and a repetition rate of 1 Hz for 30 min or more. The ambient gas (Ar

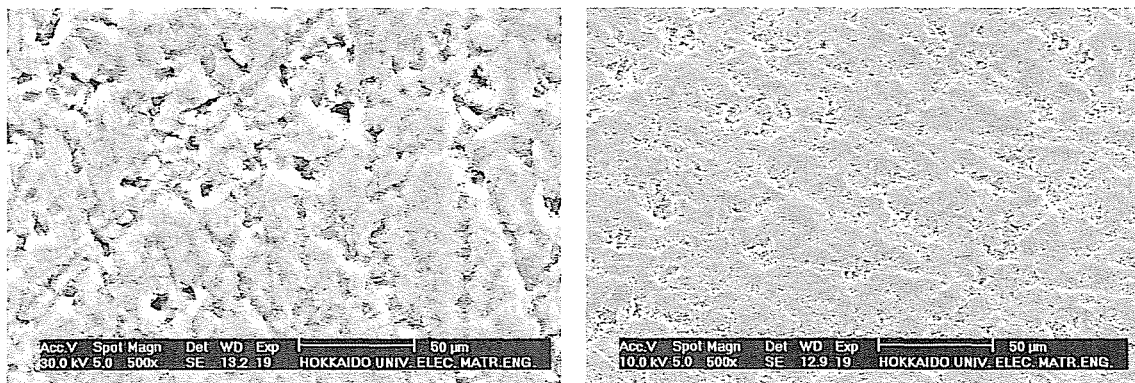


Figure 2.3. SEM micrographs of the graphite target surface: (a) laser-ablated and (b) after the treatment with an abrasive paper and cotton.

and so forth) was introduced through a mass flow controller, and the gas pressure was kept by using a butterfly valve. When an RF power was input to the coil, plasma was generated around the coil. In order to eliminate a contamination on the target surface, the target surface was ablated for ~10 min masking the substrate by the shutter before deposition. The target was kept moving in x and y directions to ablate the whole area of target.

## 2.2 Carbon Nanotube / Nanofiber Growth System

### 2.2.1 Experimental Setup

The schematic diagram of carbon nanotube / nanofiber growth system is shown in Figure 2.4. The set-up (AL039, SUGA Co., Ltd.) consists of an alumina or quartz tube of 60 mm in inner diameter and 620 mm in length, an electrical furnace (360 mm in length) operated at 800–1100°C, and the ArF excimer laser used as well as in the PAPLD experiments. The alumina tube was used when the oven temperature  $T$  was raised up to

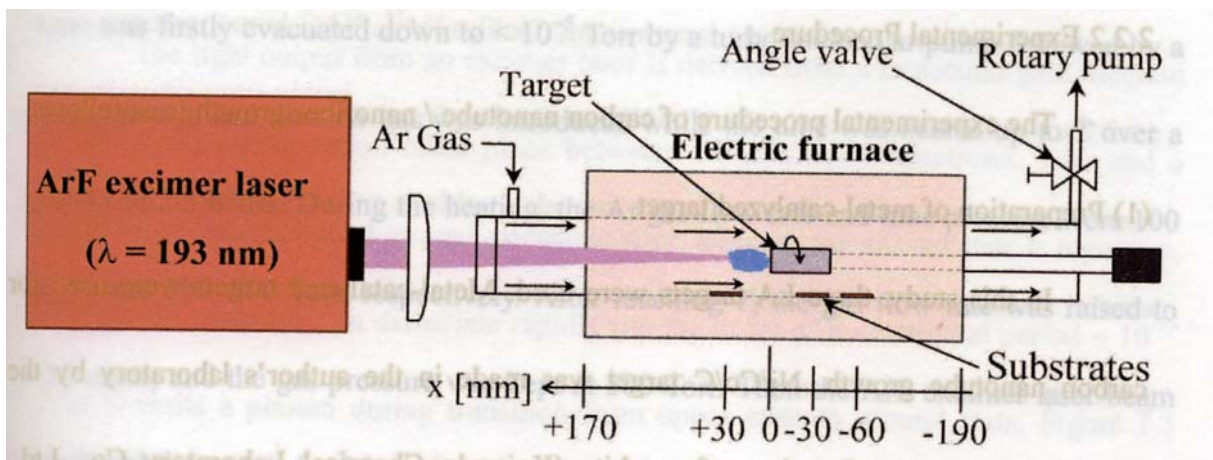


Figure 2.4. Schematic diagram of carbon nanotube / nanofiber growth system.

1100°C.  $T$  in the span of ~100 mm at the center of the furnace was kept constant and dropped gradually down to ~700°C at the front end and ~800°C at the back end when  $T$  was 1100°C. Inside the tube, an LA target was mounted at the center of the furnace and rotated at 40 rpm.

The ArF laser beam was reflected at a right angle by a quartz prism and irradiated onto an LA target at normal angle. A plane-convex lens (focal length = ~800 mm) was used for focusing. Dimension of the focused laser beam was 1 mm × 5 mm. Sintered graphite targets with 1.2 at. % Ni and 1.2 at. % Co (Ni/Co/C), with 1 at. % Ni and a small amount of Y (Ni/Y/C target, TOYO TANSO Co., Ltd.) and without them (pure graphite, Kojundo Chemical Laboratory Co., Ltd.; Furuuchi Chemical Corp.) were used as an LA target. Ar and H<sub>2</sub> (purity = 99.99999%) gases were introduced into the chamber from the laser irradiation window side and pumped out through an angle valve. The gas flow rates of Ar and H<sub>2</sub> were controlled by a flow meter and mass flow controller, respectively.

### 2.2.2 Experimental Procedure

The experimental procedure of carbon nanotube / nanofiber growth is as follows.

#### (1) Preparation of metal-catalyzed target

In this study, three LA targets were used. Metal-catalyzed targets were used for carbon nanotube growth. Ni/Co/C target was made in the author's laboratory by the following procedure. Powders of graphite (Kojundo Chemical Laboratory Co., Ltd.,



grain diameter = 20  $\mu\text{m}$ , 99.9%), Ni (The Nilaco Corp., 3–7  $\mu\text{m}$ , 99.8%) and Co (Kojundo Chemical Laboratory Co., Ltd., 5  $\mu\text{m}$ , 99%up) were stirred in a glass vessel for some time in order that the Ni and Co concentration resulted in 1.2 at. % each and then mixed with a graphite bond (The Nilaco Corp., 551-F). This mixture was cast in a graphite mold with a 20-mm diameter hole and calcined in the chamber at 1000°C with an Ar gas flow rate of 500 sccm.

## (2) Preparation of catalysts on substrates

To grow carbon nanofibers on substrates, Ni and Fe catalyst films with thicknesses of 1–350 nm were respectively deposited on  $\text{SiO}_2$  (thickness = 200 nm)/Si substrates by DC sputtering.

## (3) Growth experiment

An LA target was placed inside the alumina/quartz tube, and Si substrates with the metal catalysts (Ni/ $\text{SiO}_2$ /Si and Fe/ $\text{SiO}_2$ /Si) and without them ( $\text{SiO}_2$ /Si) placed at between –60 and +30 mm from the target surface (+: upstream of the Ar gas flow). The tube was firstly evacuated down to  $< 10^{-5}$  Torr by a turbo-molecular pump followed by a rotary pump, and then Ar gas was introduced while the tube was heated up to  $T$  over a period of 2.5 hours. During the heating, the Ar gas flow rate and tube pressure were 100 sccm and 300–500 Torr, respectively. After reaching  $T$ , the gas flow rate was raised to 750 sccm, and the gas pressure was kept at 500 Torr. Then the ArF excimer laser beam irradiated the targets for 2 hours.

## 2.3 Lasers

### 2.3.1 Lasers for PLD work

In general, the useful range of laser wavelengths for thin-film growth by PLD lies between 200 nm and 400 nm. Most materials used for deposition work exhibit strong absorption in this spectral region. Absorption coefficients tend to increase as one moves to the short wavelength end of this range and the penetration depth into the target materials are correspondingly reduced. This is a favorable situation because thinner layers of the target surface are ablated as one moves closer to the 200-nm mark. The stronger absorption at the short wavelengths also results in a decrease in ablation fluence thresholds. Below 200 nm, strong absorption by the Schumann-Runge bands of molecular oxygen can make working in this part of the spectrum difficult. Within the 200-nm to 400-nm range there are few commercially available laser sources capable of easily delivering the high fluences ( $> 1 \text{ J/cm}^2$ ), in relatively large areas ( $10 \text{ mm}^2$  or larger), that are required for laser deposition work.

The excimer laser is a gas laser system. Unlike  $\text{Nd}^{3+}$ : YAG lasers, excimer lasers emit their radiation directly in the UV. High outputs delivering in excess of 1 J/pulse are commercially available. These systems can also achieve pulse repetition rates up to several hundred hertz with energies near 500 mJ/pulse. Consequently, the excimer is generally the laser of choice for PLD work.

Table 2.1 gives a list of excimer wavelength that has been developed into

Table 2.1. Excimer laser operating wavelength.

Excimer	Wavelength (nm)
F <sub>2</sub>	157
ArF	193
KrCl	222
KrF	248
XeCl	308
XeF	351

commercial laser systems. The corresponding active excimer molecule is indicated as well. Of the excimers listed, KrF and XeCl have been extensively used for PLD. KrF is the highest gain system for electrically discharged pumped excimer lasers and is the popular choice among the PLD community. In the present study, ArF was mainly used because the LA by ArF excimer produces more energetic ions than KrF does [45].

### 2.3.2 Excimer Basics

The light output from an excimer laser is derived from a molecular gain medium in which the lasing action takes place between a bound upper electronic state and a repulsive or weakly bound ground electronic state. Because the ground state is repulsive, the excimer molecule can dissociate rapidly (on the order of a vibrational period  $\sim 10^{-13}$  s) as it emits a photon during transition from upper state to ground state. Figure 2.5 shows a typical molecular potential energy diagram of an excimer system.

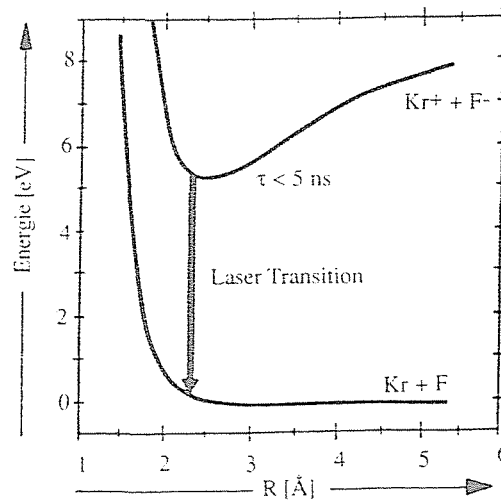


Figure 2.5. Schematic diagram of the electronic potential of the KrF excimer [1].

The excimer molecules are formed in a gaseous mixture of their component gases, such as Ar, F<sub>2</sub> (balanced with He), and Ne in the case of the ArF laser. Energy is pumped into the gas mixture through avalanche electric discharge excitation. The pumping creates ionic and electronically excited species that react chemically and produce the excimer molecules. Commercially available laser systems producing several hundred millijoules/pulse are all of the electric discharge type.

The details of the kinetics and chemical reactions leading to the formation of the excimer molecules are quite complex and can consist of many steps. Some of the more important reactions for the case of KrF are listed below where the \* denotes an electronically excited species and X denotes a third body (He, Ne).

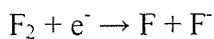
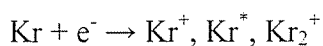
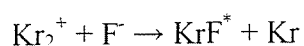
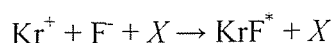


Table 2.2. The specification of the ArF excimer laser used in this study.

Pulse energy (measured at repetition rate of 5 Hz)	400 mJ
Maximum repetition rate	50 Hz
Average power (50 Hz)	4 W
Pulse duration	20 ns, FWHM
Beam dimensions (typical value, FWHM)	$24 \times 6\text{--}12 \text{ mm}^2$ (V×H)
Beam divergence (typical value, FWHM)	$3 \times 1 \text{ mrad}$ (V×H)



Once the excimer is formed, it will decay via spontaneous emission and collisional deactivation giving the molecule a lifetime of  $\sim 2.5$  ns. Moderate output energies of several hundred millijoules per laser pulse dictate an excimer population density requirement on the order of  $10^{15} \text{ cm}^{-3}$ . Therefore, in order for lasing action to occur, the formation rate of the ionic and excited precursors must be fast enough to produce excimers at a rate of several  $10^{23} \text{ cm}^{-3} \text{ s}^{-1}$  [1]. Table 2.2 shows the specification of the ArF excimer laser that is used in the present study.

## **2.4 Characterization of Ablation Plume and Carbon Nanomaterials**

### **2.4.1 Diagnostics of Ablation Plume**

Optical emission spectra of the carbon ablation plume were observed by two photonic multichannel analyzers (PMA: Hamamatsu Photonics K.K., PMA-11, wavelength resolution = 2 nm, spectral range = 300–800 nm and 200–400 nm, respectively) with an exposure time of 19 ms.

### **2.4.2 Surface Morphology**

Surface morphology of amorphous carbon films, nanoparticles, carbon nanotubes and nanofibers were examined with scanning electron microscopy (SEM), atomic force microscopy (AFM) and transmission electron microscopy (TEM). A tungsten hairpin filament type SEM (Shimadzu Corp., SUPERSCAN model 220, image resolution = 3.5 nm) and cold field emission one (Hitachi High-Technologies Corp., S-4300, image resolution = 1.5 nm at an acceleration voltage = 15 kV; S-4800, image resolution = 1.0 nm at 15 kV) were used. The AFM (Digital Instruments, Nanoscope III Dimension 3000) was calibrated by probing a standard test grating with a groove of 5  $\mu\text{m}$  in breadth and 180 nm in depth.

### **2.4.3 Chemical Composition and Bonding State**

Chemical composition of amorphous carbon films, nanoparticles and carbon

nanotubes were examined with X-ray photoelectron spectroscopy (XPS) and energy dispersive X-ray analysis (EDX). In the XPS analysis (Shimadzu Corp., ESCA-3400; X-ray radiation: Mg-K $\alpha$  X-ray radiation ( $h\nu=1253.6$  eV); pass energy = 75 eV), the binding energy of Au (4f) = 83.57 eV was referred to calibrate the binding energy of C (1s). Gold spots were deposited by vacuum evaporation in some small areas ( $\phi = \sim 100$   $\mu\text{m}$ ) on amorphous carbon films before the analysis.

Raman spectroscopy was used for the characterization of various forms of carbon.

Two Raman spectrometers (Renishaw plc., System-1000, excitation laser: Ar ion laser ( $\lambda = 514.5$  nm); JASCO Co. Ltd., NRS-1000HS, excitation laser: Green ( $\lambda = 532$  nm) and He-Ne laser ( $\lambda = 632.8$  nm)) were used in this study.

## Chapter 3

### Diagnostics of Carbon Ablation Plume

#### 3.1 Observation of Carbon Ablation Plume

Figure 3.1 shows photographs of carbon ablation plume. The plume was generated by the ArF laser ablation at a frequency of (a) 20 Hz and (b-c) 1 Hz. Figure 3.1 (a) clearly shows that an ablation plume in vacuum flies at right angle to the target with strong directivity. This is a typical behavior of laser ablation plume. In order to explain

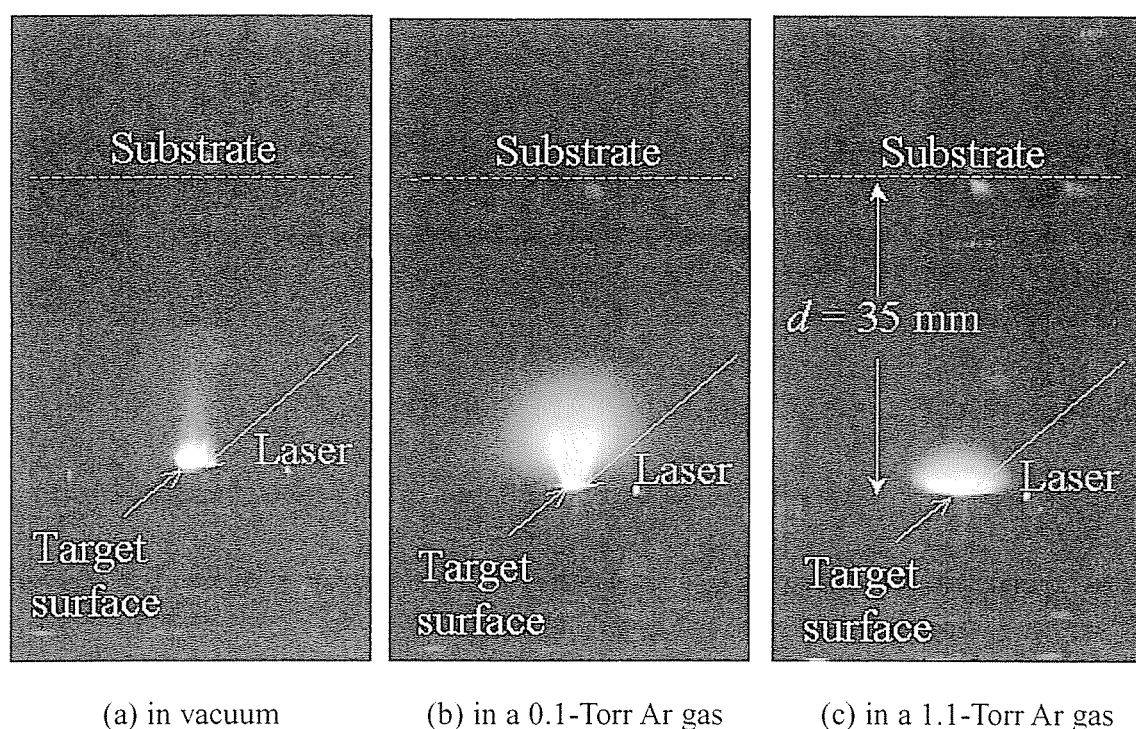


Figure 3.1. Photographs of carbon ablation plume in (a) vacuum and (b-c) Ar gas. The exposure time was 2 sec. The laser repetition rate was (a) 20 Hz and (b-c) 1 Hz. The laser fluence was  $3.5 \text{ J/cm}^2$ .



this behavior, a model is proposed by Ohtsubo, et al as follows [46]. When laser energy is absorbed into the target surface, the surface temperature is raised. If the optical absorbance of target is high, the temperature at the sub-surface becomes higher than that of the surface, then the domain of sub-surface melts and evaporates because the surface temperature does not exceed the boiling temperature of target material. Consequently, an explosive removal by the generation of high pressure in the sub-surface can occur.

Unlike the LA plume in vacuum, the plume emission in Ar gas spreads and forms an oval figure. It is thought that the ablated particles, such as, electrons, carbon ions, atoms and molecules collide with Ar gas atoms, and then diffuse and decelerate. The Ar gas atoms emit light as well as carbon because they were excited due to the collision with electrons in the plume [47]. It was confirmed that as Ar gas pressure increases up to several tens Torr, the plume emission was crushed and became flat.

### **3.2 Current Waveform of Carbon Ablation Plume**

The current waveform of carbon ablation plume was measured with an oscilloscope (Iwatsu Electric Co. Ltd., DS-8812). The experimental condition is shown in Table 3.1. Figure 3.2 shows the measuring electrical circuit. A shutter, which was inserted between the target and substrate, was used as a collector electrode. Figure 3.3 shows current waveforms on the (a) nano- and (b) micro-second time scales. The waveform shown was averaged over the 10 measurements. Launch of the ablation plume

Table 3.1. The experimental condition for measuring the current waveform.

Ar gas pressure $p_{Ar}$	0 – 10 Torr
Shutter diameter	70 mm
Distance between the target and shutter	18, 25 mm
Bias voltage	-10 – 10 V
Laser fluence	4 J/cm <sup>2</sup>

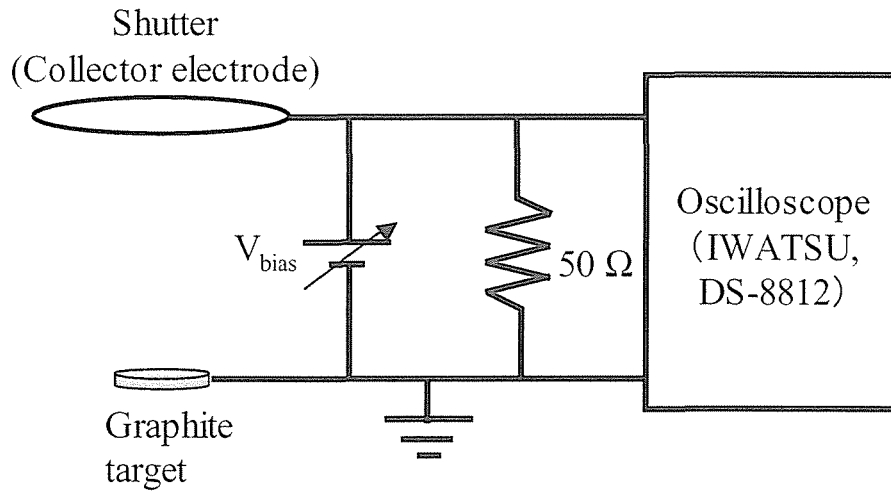


Figure 3.2. Measuring electrical circuit for the current waveform.

was determined by coupling the photo diode signal, which responded to the excimer laser irradiation as shown in Figure 2.1. The current was first negative, then turned to positive and finally attenuated. It is believed that the negative portion with a time scale of  $\sim 100$  ns is due to electron conduction and the positive one with that of  $\sim 10$   $\mu$ s is due to positive ion conduction.

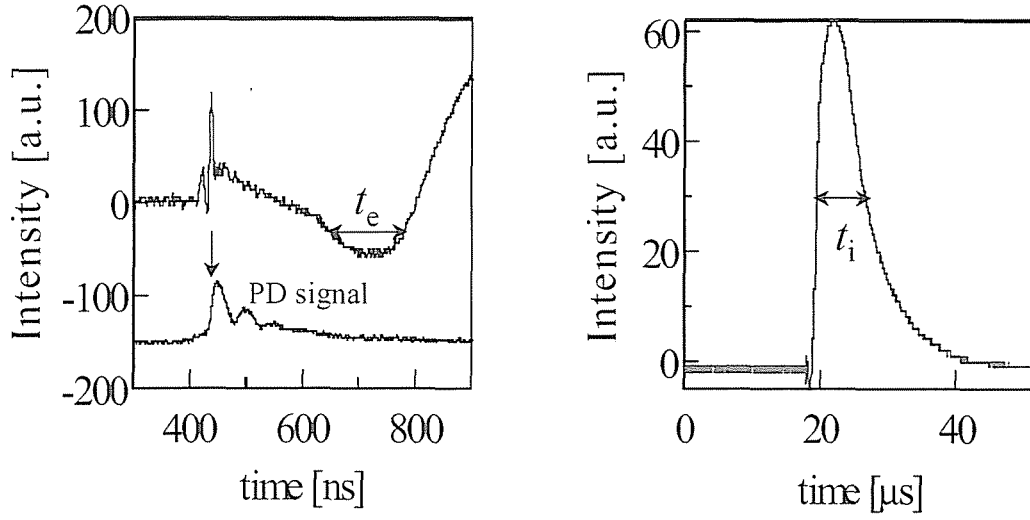


Figure 3.3. Current waveforms of carbon ablation plume: (a) “fast” waveform and (b) “slow” one.

Let me call the negative current “fast waveform” and the positive one “slow waveform”. “Fast” and “slow” waveforms are ascribed to the conduction of carbon ions ( $C_n^+$ ) and electrons, respectively. By analyzing the full width at half maximum of these waveforms, the velocity of electrons and positive ions was evaluated to be  $1.8 \times 10^5$  m/s and  $1.2 \times 10^4$  m/s, respectively. The ion velocity measured in this study is about 3-4 times higher than the result by Kokai, et al who measured velocities of  $C_3^+$  and  $C^+$  with time-of-flight mass spectrometry to be  $4.5 \times 10^3$  m/s and  $3.0 \times 10^3$  m/s, respectively at a laser fluence of  $1.3 \text{ J/cm}^2$  [48]. As shown in Figure 3.4, the electron velocity increased with laser fluence, however the velocity of carbon ions did not show clear dependence on the fluence. It is known that carbon ablation plume contains many carbon ions with

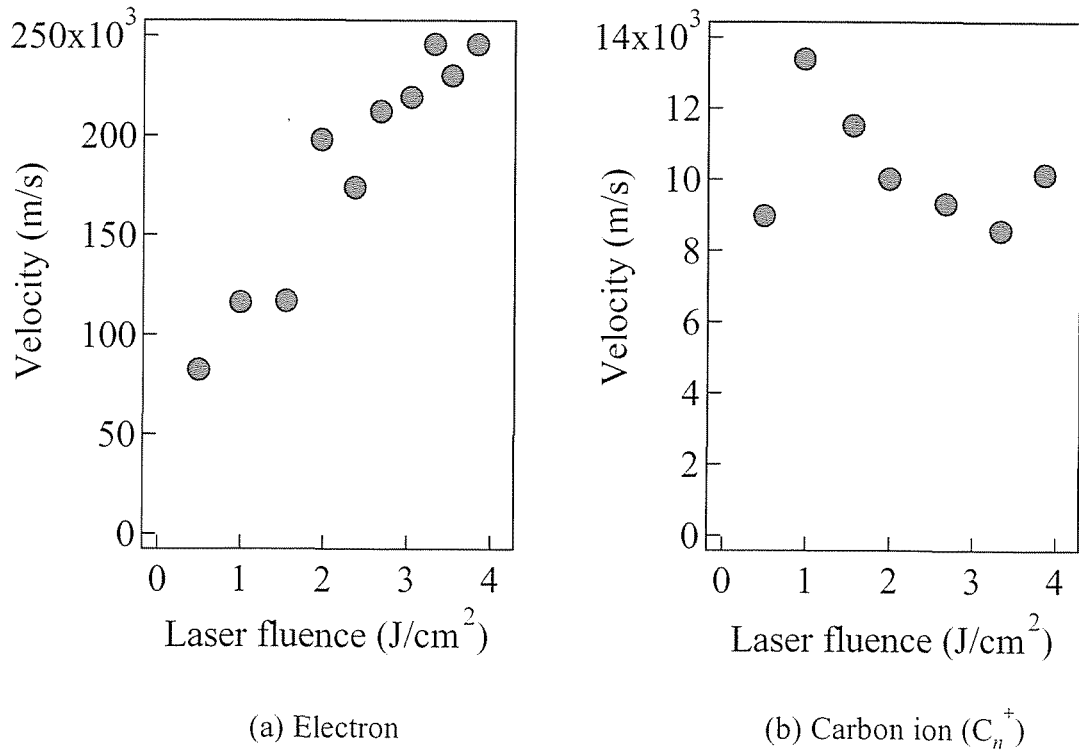
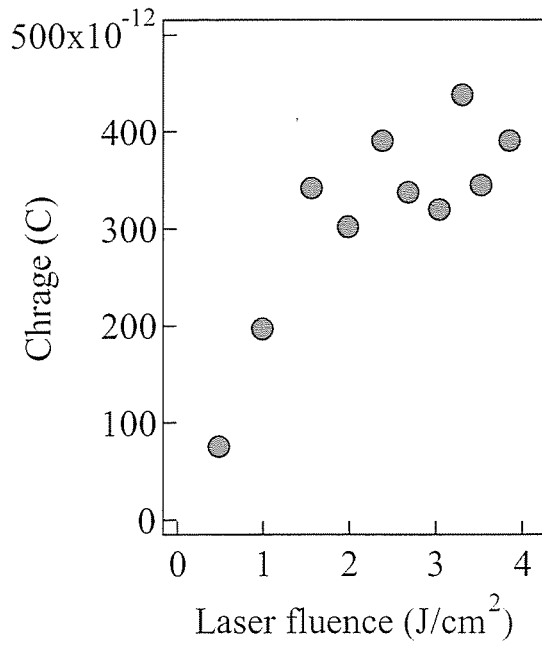


Figure 3.4. The velocity of (a) electrons and (b) positive ions.

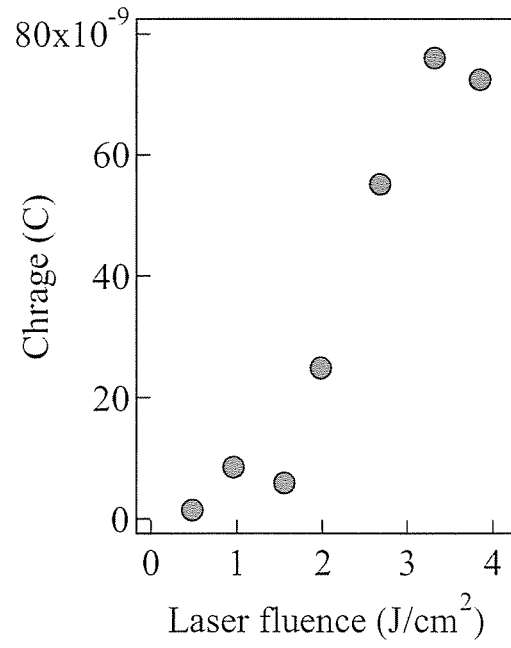
different masses (C<sub>n</sub><sup>+</sup>). In this measurement, it was difficult to distinguish them in the current waveform.

The positive and negative charges in one ablation plume were evaluated by an integration of the dimension of “fast” and “slow” waveforms. As shown in Figure 3.5, the both charges linearly increased with laser fluence in the range of 0 – 4 J/cm<sup>2</sup>. This graph also indicates that the laser ablation of graphite requires a threshold laser fluence of ~0.5 J/cm<sup>2</sup>.

Figure 3.6 shows the current waveforms of carbon ablation plumes under (a) positive and (b) negative biases applied to the shutter. The current intensity is shown in



(a) Charge of electrons



(b) Charge of  $C_n^+$

Figure 3.5. Charges of (a) electrons and (b) positive ions estimated by the current waveforms.

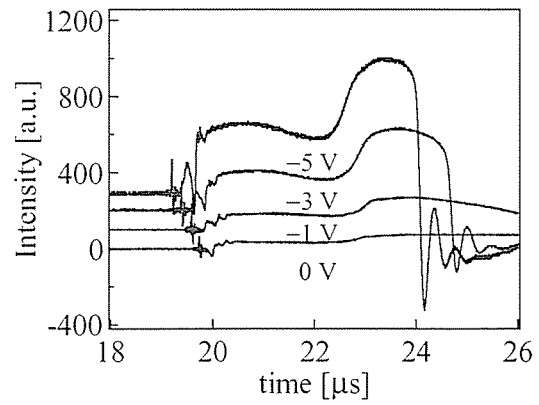
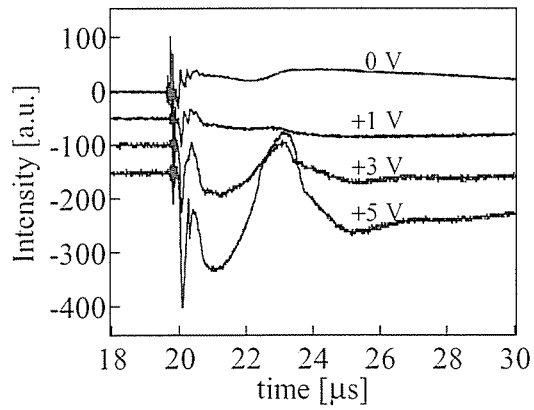


Figure 3.6. Current waveforms of carbon ablation plumes under (a) positive and (b) negative biases.

arbitrary unit. These clearly show that the positive and negative ions in the plume were influenced by the electric field generated between the target and shutter. As the positive bias increased, positive component in the waveform disappeared, and the negative one appeared instead. On the contrary, only the positive component appeared when negative bias was applied. The duration of current waveform shortened as the negative bias increased. These results ensure that carbon ablation plume contains electrons, positive and negative ions.

### 3.3 Optical Emission Spectra of Carbon Ablation Plume

Figure 3.7 shows the optical emission spectra of carbon ablation plume in vacuum. Two photonic multichannel analyzers were used to obtain the spectra in UV (200 – 400 nm) and visible wavelength (300 – 800 nm) regions. The exposure time was 19 ms. In UV region (Figure 3.7 (a)), the emission peaks from the carbon atom (CI,  $3s^1P_1^0 \rightarrow 2p^2^1S_0$  at 247.9 nm) and molecule ( $C_2$ ,  $C^1\Pi_g - A^1\Pi_u$  at 385.2 nm) were observed [49, 50]. The CI emission is ascribed to recombination of singly ionized carbon ions with electrons [49]. There are a lot of emission peaks of carbon ions (C II and C III) in a wavelength range of 200 – 400 nm, but these were not observed. This would be reasonable because the upper levels of almost all of these peaks are higher than 20 eV. In visible wavelength region (Figure 3.7 (b)), several emission peaks from C I, C II and  $C_2$  appeared: C II peaks at 426.7 nm ( $4f^2F^0 \rightarrow 3d^2D$ ), 589.1 nm ( $4p^2P^0 \rightarrow 3d^2D$ ), 657.8 nm ( $3p^2P^0 \rightarrow 3s^2S$ ) and

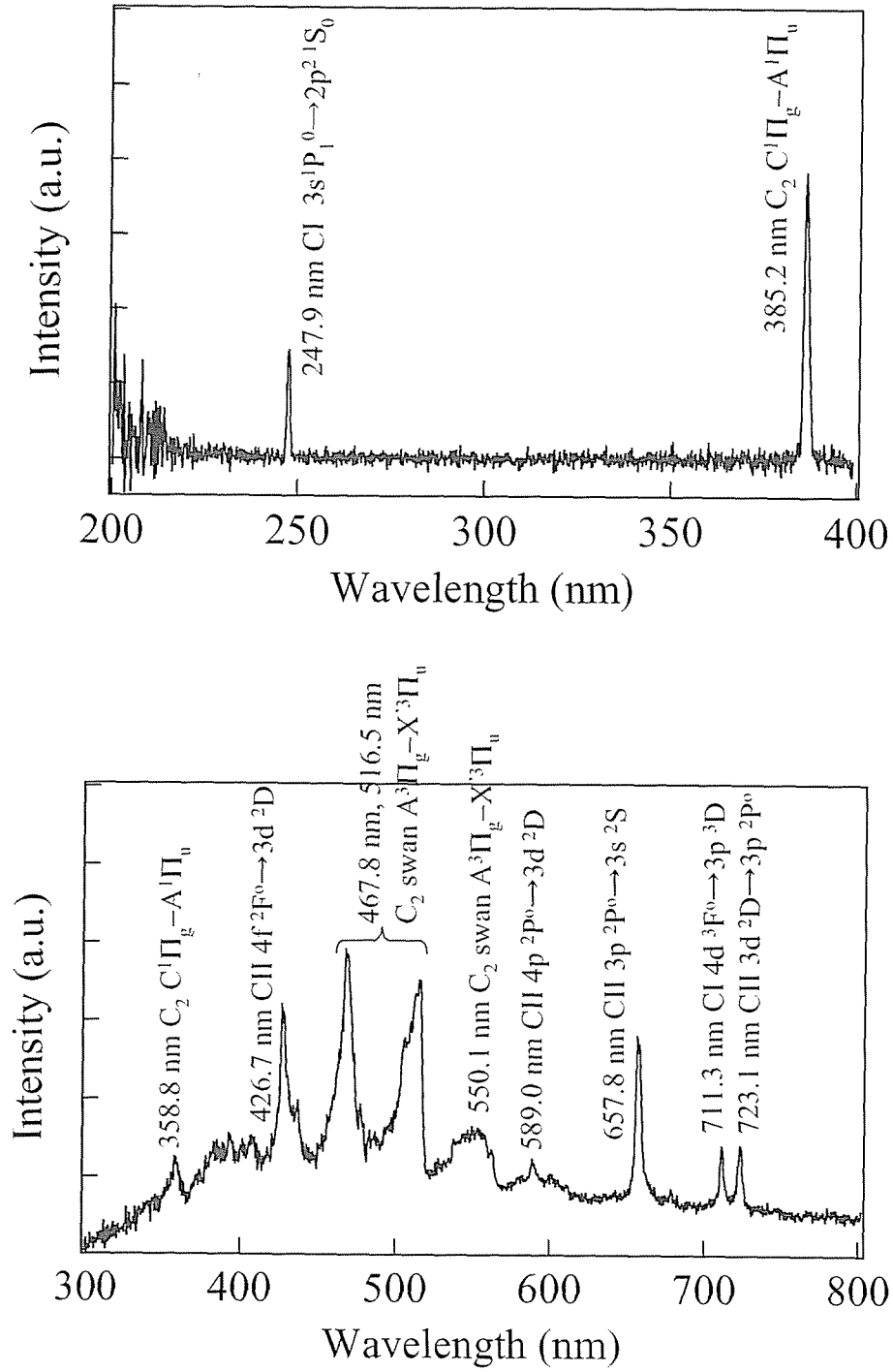


Figure 3.7. The optical emission spectra of carbon ablation plume in vacuum: (a) UV wavelength region; (b) visible wavelength region (PMA exposure time = 19 ms, laser fluence =  $4 \text{ J/cm}^2$ , repetition rate = 1 Hz).

723.1 nm ( $3d\ ^2D \rightarrow 3p\ ^2P^o$ ); Cl peak at 711.3 nm ( $4d\ ^3F^o \rightarrow 3p\ ^3D$ );  $C_2$  peaks at 358.8 nm ( $C^1\Pi_g - A^1\Pi_u$ ), 467.8 nm, 516.5 nm and 550.1 nm ( $A^3\Pi_g - X^3\Pi_u$ ) [49, 51]. These emission peaks appeared here are mainly from not carbon atoms but carbon ions and molecules ( $C_2$ ). This indicates that the laser ablation plume has a high ionization degree.

When Ar gas was introduced into the PLD chamber, the emission peaks of Ar as well as carbon were observed. The Ar peaks appeared at  $p_{Ar} \geq 50$  mTorr, and their intensity increased with  $p_{Ar}$  in the present experimental condition. Figure 3.8 shows the

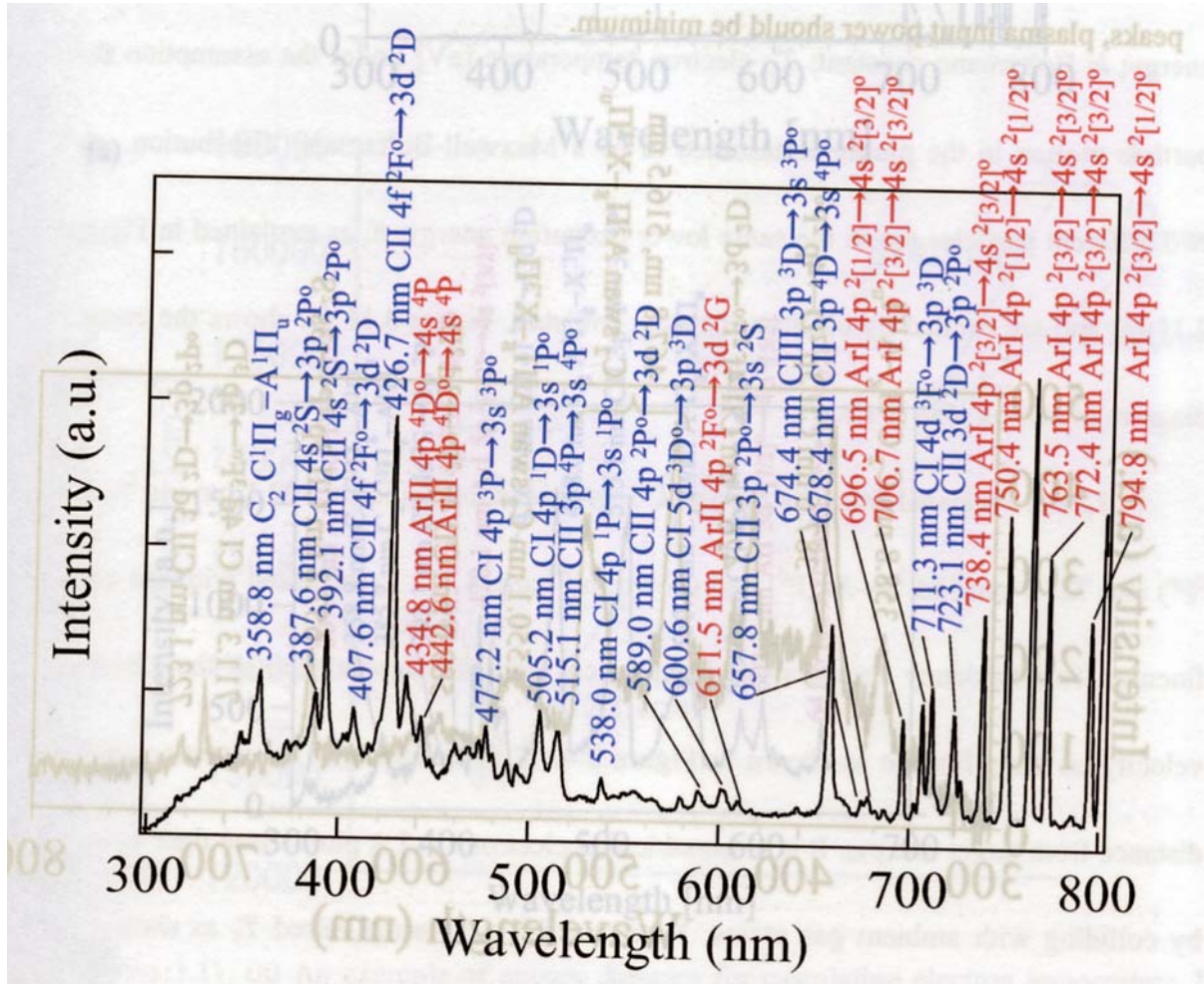


Figure 3.8. The optical emission spectra of carbon ablation plume in Ar gas at  $p_{Ar} = 1$  Torr. The laser fluence and repetition rate were  $4\text{ J/cm}^2$  and 1 Hz, respectively.



optical emission spectra at  $p_{\text{Ar}} = 1$  Torr. The emissions from C I, C II, Ar I and Ar II were observed. The optical emission spectra in a 0.5-Torr He gas is shown in Figure 3.9. It is similar to that in vacuum, and no emission peaks from He was observed. This seems reasonable because the excitation energy of He is higher than that of Ar.

When Ar plasma was generated with an input power  $< 10$  W, the emission intensity of Ar atoms in a range of 700 – 800 nm was much higher than those of carbon atoms and molecules as shown in Figure 3.10. In order to observe the both Ar and carbon emission peaks, plasma input power should be minimum.

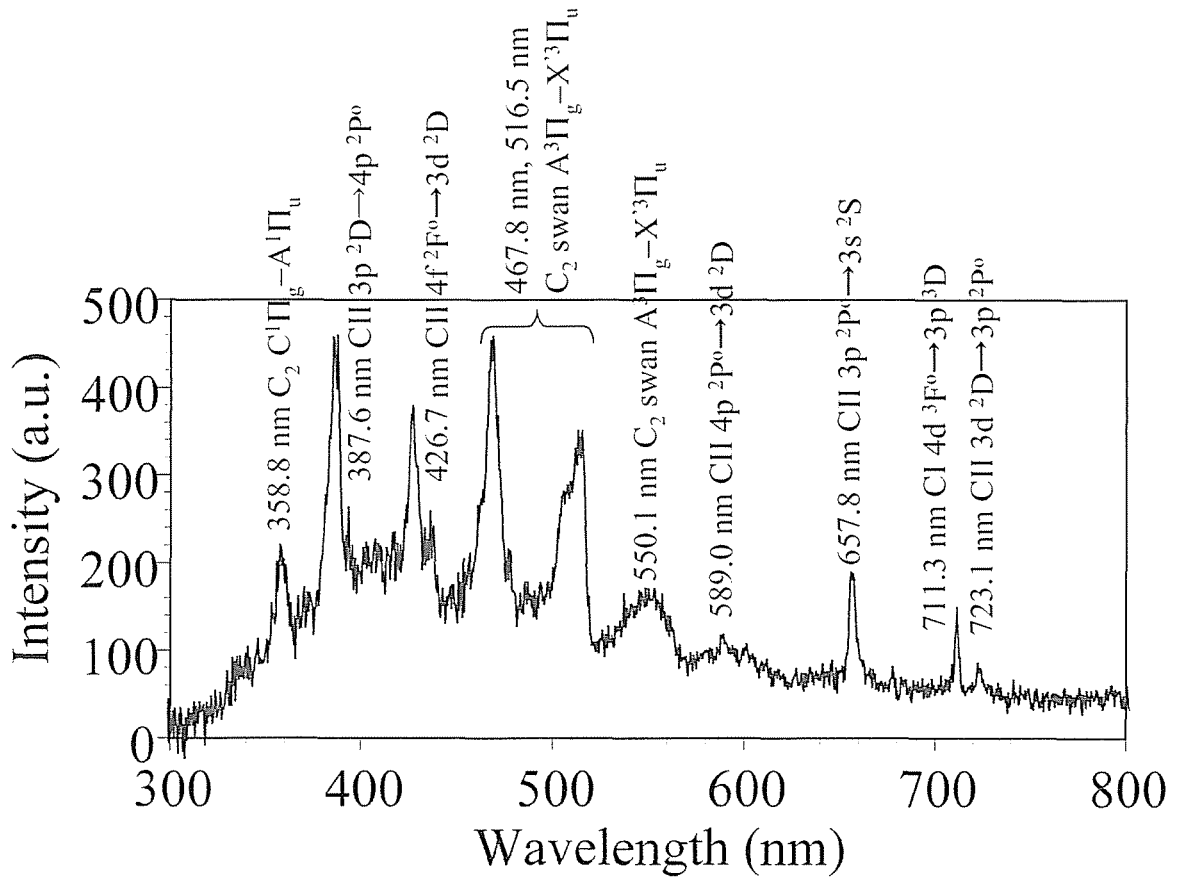


Figure 3.9. The optical emission spectra of carbon ablation plume in a 0.5-Torr He gas.

The laser fluence and repetition rate were  $4 \text{ J/cm}^2$  and 1 Hz, respectively.

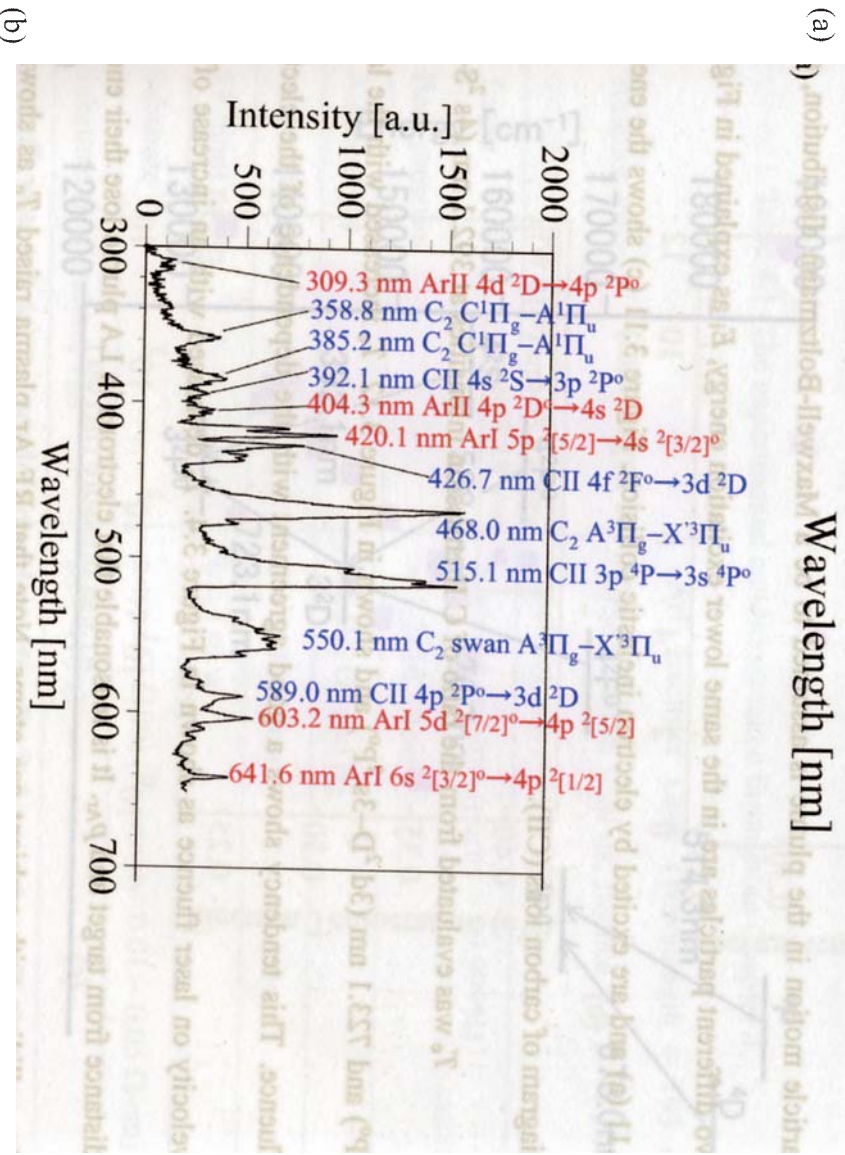
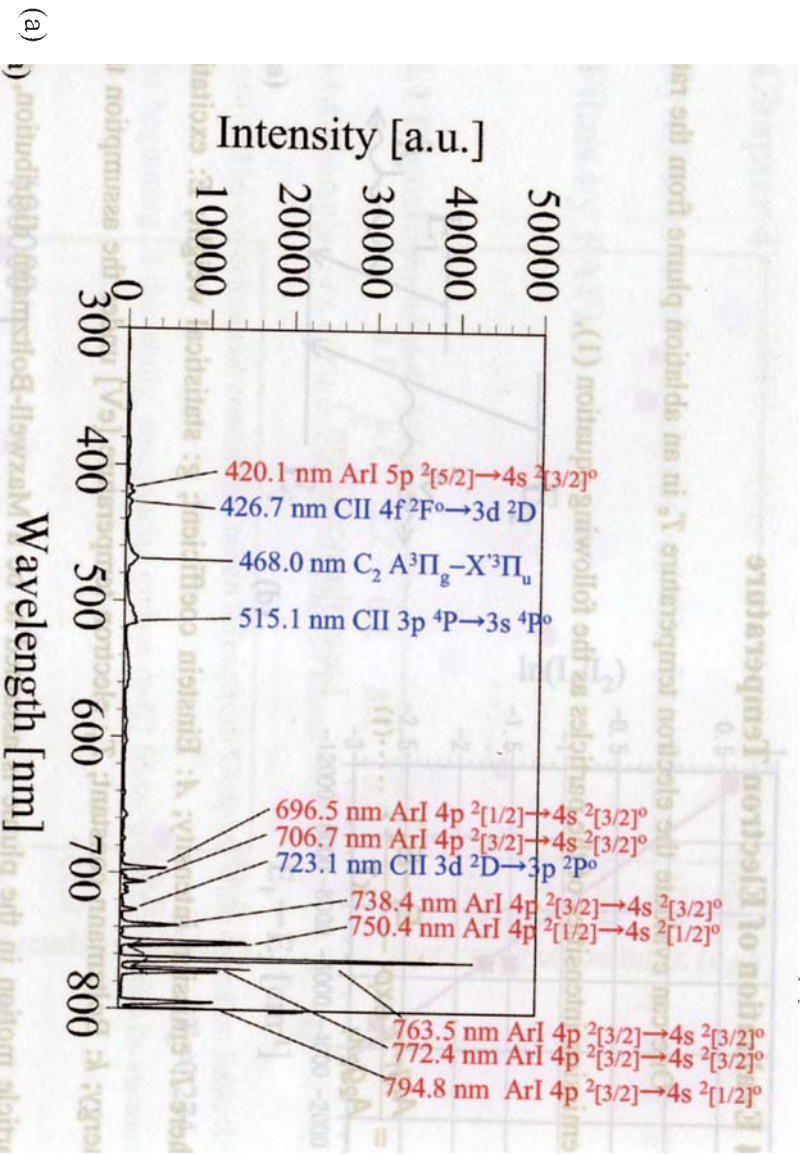


Figure 3.10. The optical emission spectra of carbon ablation plume in RF Ar plasma at

$P_{Ar} = 1$  Torr in a wavelength range of (a) 300–800 nm and (b) 300–650 nm.

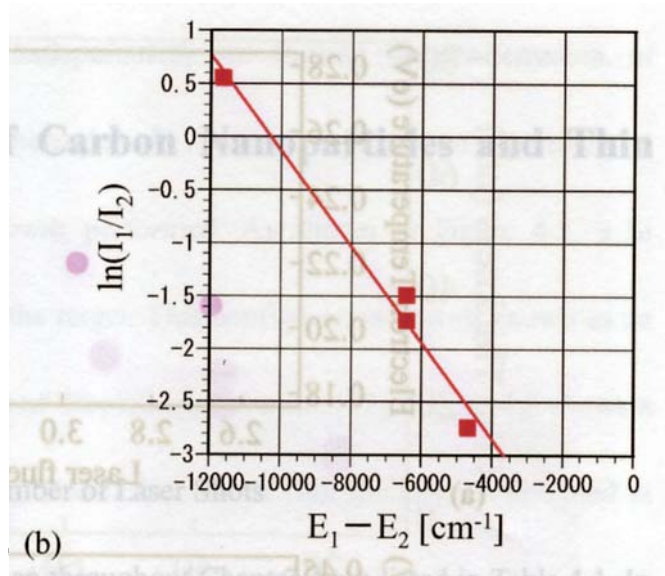
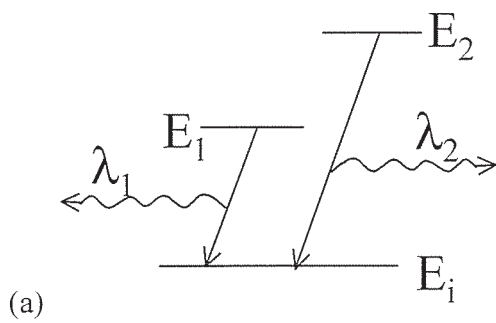
### 3.4 Evaluation of Electron Temperature

One can evaluate the electron temperature  $T_e$  in an ablation plume from the ratio of emission intensities of the particles as the following equation (1),

$$\frac{I_1}{I_2} = \frac{A_1 g_1 \lambda_2}{A_2 g_2 \lambda_1} \exp\left\{-\frac{E_1 - E_2}{kT}\right\} \dots\dots(1)$$

where  $I$ : emission intensity;  $A$ : Einstein coefficient;  $g$ : statistical weight;  $E$ : excitation energy;  $k$ : Boltzmann constant;  $T_e$ : electron temperature [eV] under the assumption that particle motion in the plume is assumed to be a Maxwell-Boltzmann distribution, and two different particles are in the same lower excitation energy,  $E_i$  as explained in Figure 3.11 (a) and are excited by electron inelastic collision. Figure 3.11 (c) shows the energy diagram of carbon ions (CII).

$T_e$  was evaluated from the ratio of C II emission intensities at 392.1 nm ( $4s\ ^2S-3p\ ^2P^o$ ) and 723.1 nm ( $3d\ ^2D-3s\ ^2P^o$ ) and shown in Figure 3.12.  $T_e$  increased with the laser fluence. This tendency shows a good agreement with the dependence of the electron velocity on laser fluence as shown in Figure 3.4.  $T_e$  decreased with an increase of the distance from target and  $p_{Ar}$ . It is reasonable that electrons in LA plume lose their energy by colliding with ambient gas atoms. Note that RF Ar plasma raised  $T_e$  as shown in Figure 3.12 (c). This is an effect of plasma in plasma-assisted PLD.



$$T_e = 0.274 \text{ eV}$$

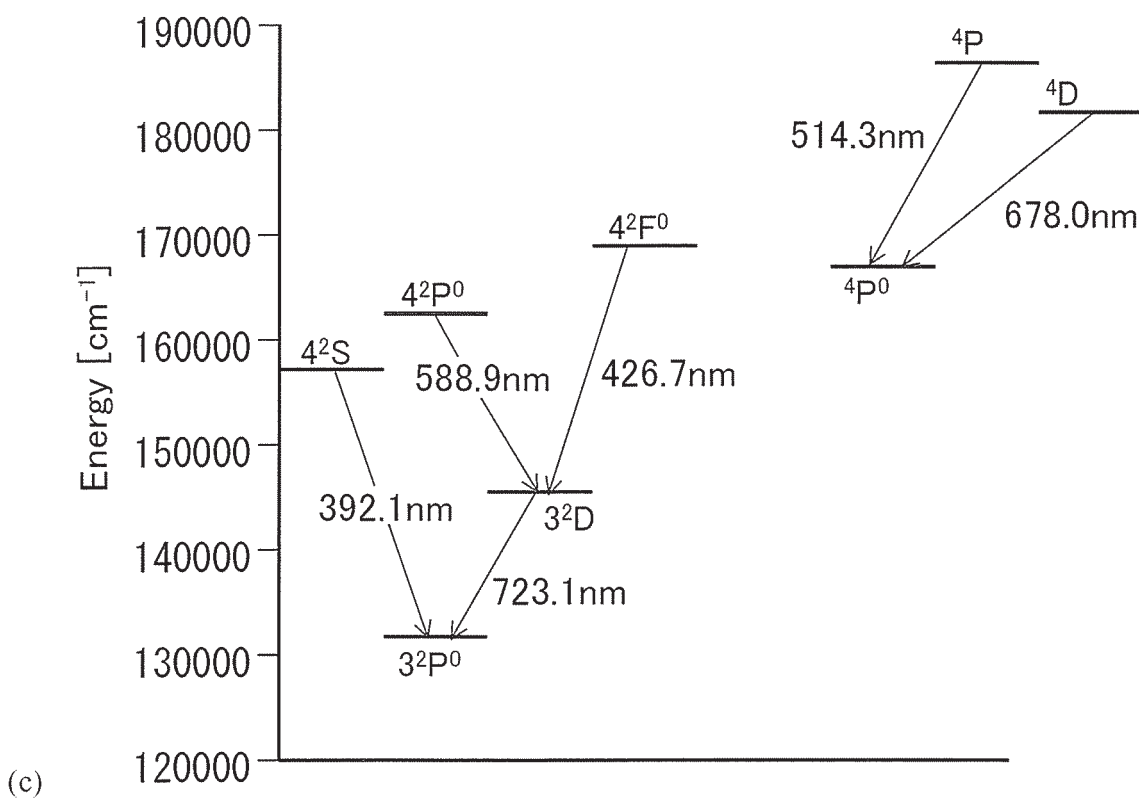


Figure 3.11. (a) An example of energy diagram for calculating electron temperature  $T_e$ .

(b) A demonstration of  $T_e$  evaluation. (c) The energy diagram of C II transition.



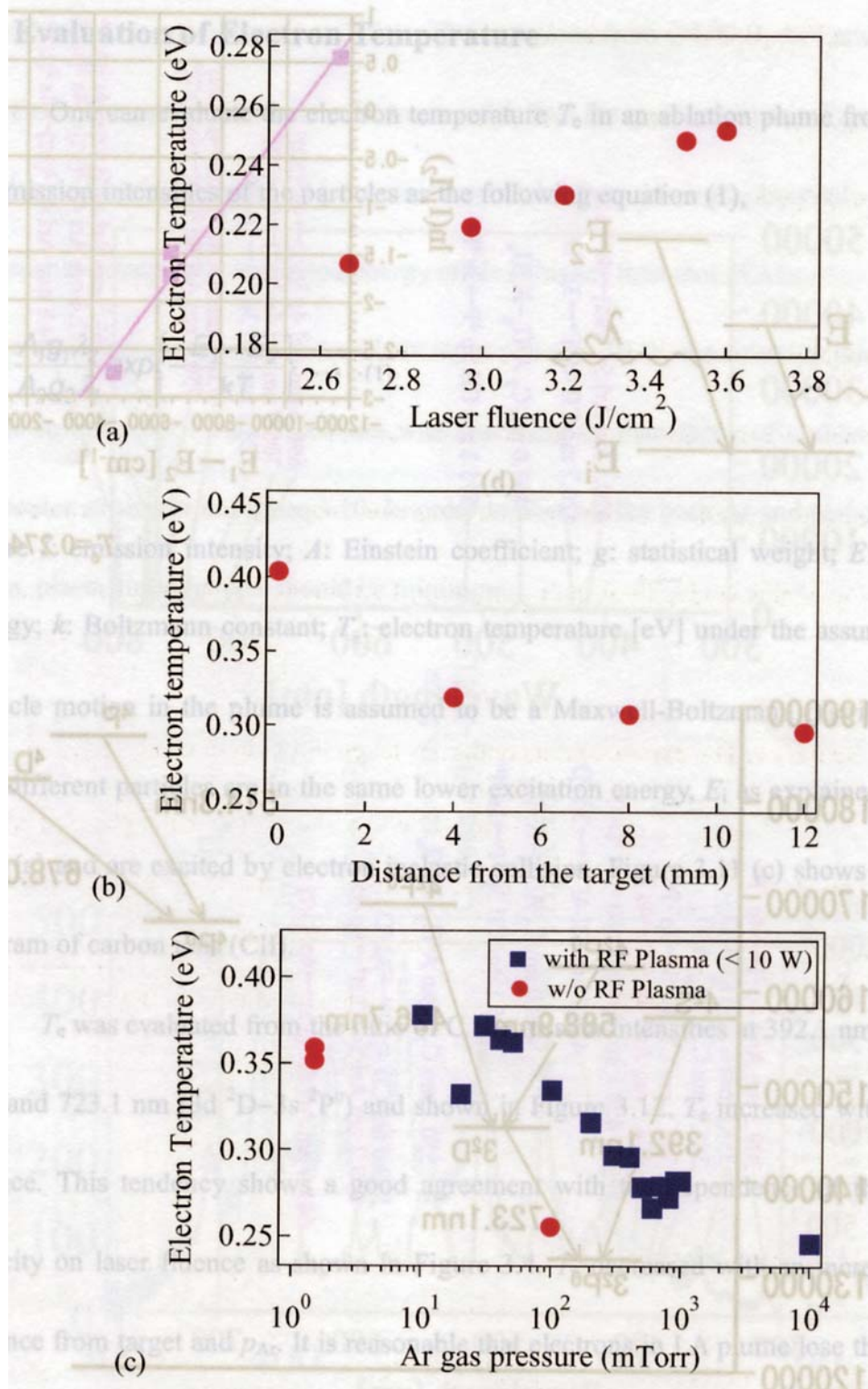


Figure 3.12. Dependence of  $T_e$  of carbon ablation plume on (a) the laser fluence, (b) distance from the target and (c) Ar gas pressure. (a)  $p_{\text{Ar}} = 0.5$  Torr, (b)  $p_{\text{He}} = 760$  Torr and (c) RF input power < 10 W.

## Chapter 4

# Syntheses and Analyses of Carbon Nanoparticles and Thin Films by PAPLD

### 4.1 Deposition of a-C Films

#### 4.1.1 Thickness of a-C Films on the Number of Laser Shots

The experimental conditions taken throughout Chapter 4 are listed in Table 4.1. In the beginning of this study, amorphous carbon (a-C) films were deposited in vacuum by

Table 4.1. The experimental conditions taken throughout Chapter 4.

Ablation laser	ArF Excimer Laser (Wavelength = 193 nm; pulse duration = 20 ns; fluence = 2.1 – 4 J/cm <sup>2</sup> ; repetition rate = 10 – 30 Hz)
Target	Sintered graphite (purity = 99.999%)
Base pressure	$< 1.7 \times 10^{-7}$ Torr
Ambient gas	Ar, He, O <sub>2</sub> and N <sub>2</sub>
Ambient gas pressure, $p_{\text{Ar, He and O}_2}$	0 – 1600 mTorr
RF input power	0 – 150 W
Substrate	n-type Si (100) (resistivity=0.01 – 0.05 $\Omega$ ·cm)
Substrate temperature, $T_{\text{sub}}$	20 – 410°C
Distance between the target and substrate, $d_{\text{st}}$	20 – 70 mm
Deposition time	10 – 60 min

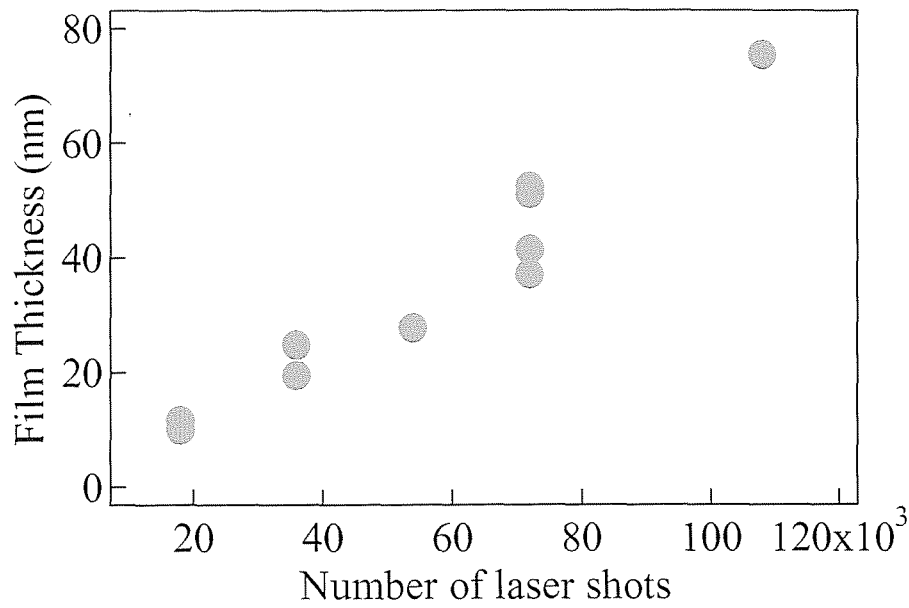


Figure 4.1. Thicknesses of a-C films deposited in vacuum at  $T_{\text{sub}}=20^{\circ}\text{C}$  vs. number of laser shots. The laser fluence and  $d_{\text{st}}$  were  $2.1 \text{ J/cm}^2$  and 35 mm, respectively.

PLD. Figure 4.1 shows the correlation between the thicknesses of a-C films and number of laser shots. The thickness was measured with an ellipsometer (Mizojiri Optical Co., Ltd., DVA-FL3, excitation laser: He-Ne laser ( $\lambda = 632.8 \text{ nm}$ )). The film thickness shown is averaged over the nine points at every 3 mm in x- and y-axes. The film thickness increased in proportion to the number of laser shots. It is reasonable that PLD can control film thickness by number of laser shots.

#### 4.1.2 Spatial Distribution of a-C Film Thickness

When a LA plume is ejected from a target and goes straightforward in a gas ambient, particles in the plume collide with the gas atoms and decelerate. In a high gas

pressure, nanometer-sized particles (nanoparticles) are formed by condensation of particles in a plume. To understand the behavior of LA plume, a deposition experiment in the following substrate configuration was performed. As shown in Figure 4.2, a Si substrate was located perpendicular to the target. This configuration is well known as an “off-axis” one for reducing the number of droplets on substrate [52]. Figure 4.3 shows a photograph of the a-C film and the spatial distributions of film thicknesses obtained at different  $p_{Ar}$ . The deposition area was  $\sim 10$  mm (y)  $\times$   $\sim 50$  mm (z) in a 10-mTorr Ar gas and became narrower as  $p_{Ar}$  increased. Note that the film outline is similar to that of the plume emission (see Figure 3.1.). The thicknesses decreased exponentially on the distance from the target  $z$  and with an increase of  $p_{Ar}$ .

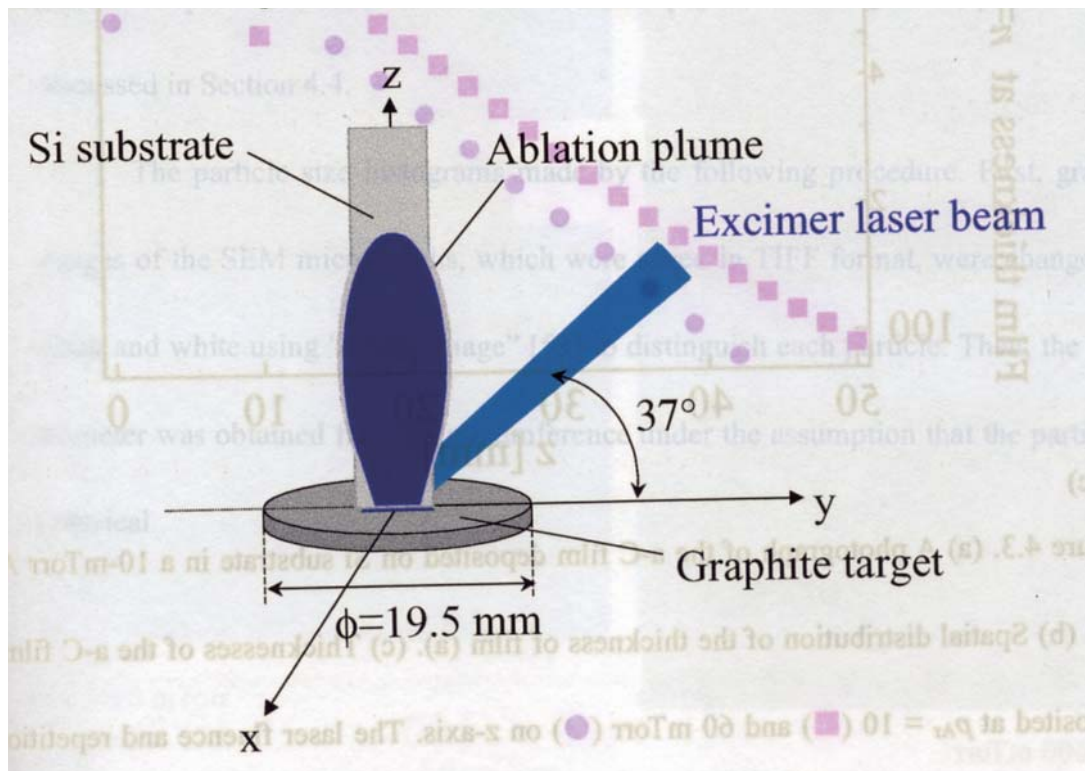


Figure 4.2. Substrate configuration for measuring the spatial distribution of a-C film thickness along the direction of LA plume ( $z$  axis).



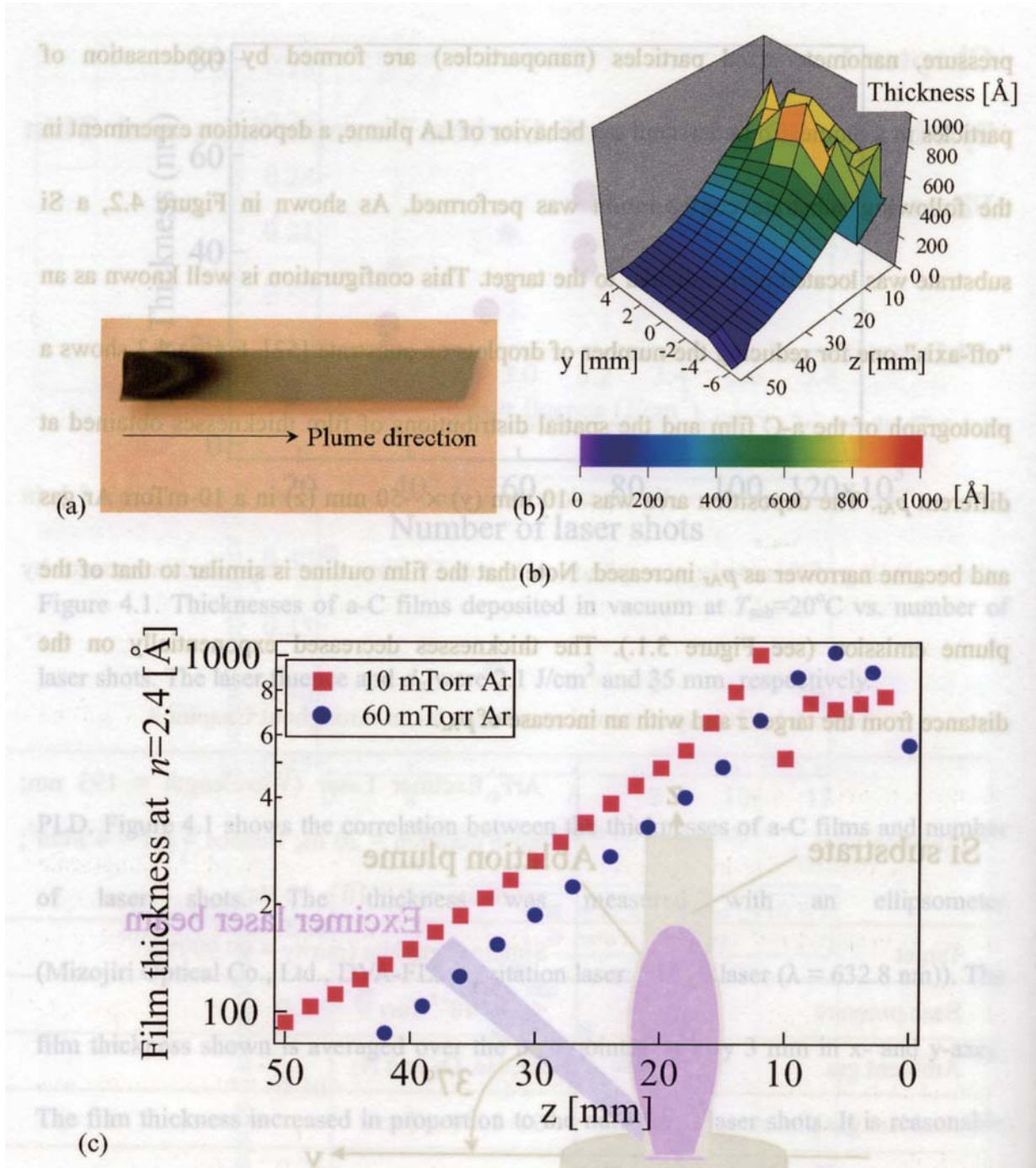


Figure 4.3. (a) A photograph of the a-C film deposited on Si substrate in a 10-mTorr Ar gas. (b) Spatial distribution of the thickness of film (a). (c) Thicknesses of the a-C films deposited at  $p_{\text{Ar}} = 10$  (■) and 60 mTorr (●) on z-axis. The laser fluence and repetition rate were  $3.2 \text{ J/cm}^2$  and 10 Hz, respectively. The film thickness was measured by ellipsometry under the assumption that the refractive index  $n$  of films is 2.4.

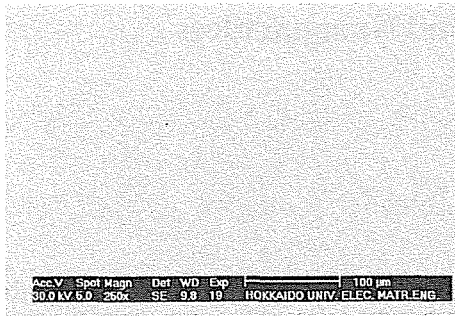
## 4.2 Surface Morphology of a-C Films and Nanoparticles

### 4.2.1 Obtained by PLD in Ar Gas

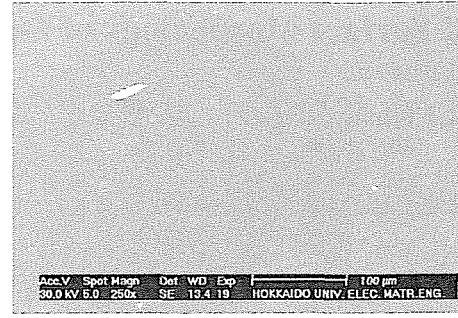
#### 4.2.1.1 SEM Analysis of a-C Film Surfaces

Amorphous carbon (a-C) films and nanoparticles were deposited on Si substrates by PLD at  $p_{Ar} = 0\text{--}1600$  mTorr. Figure 4.4 shows SEM micrographs of the a-C film surfaces. Their high-magnification images are shown in Figure 4.5. The surface of the film deposited in vacuum contains a lot of particles with a variety of shape and size from  $\sim 10$  nm to several  $\mu\text{m}$  as shown in Figure 4.5 (a). The non-spherical particles were two orders of magnitude larger than the spherical ones. It seems that the number density of particles deposited on substrates increased with  $p_{Ar}$ . The variety of the particles will be discussed in Section 4.4.

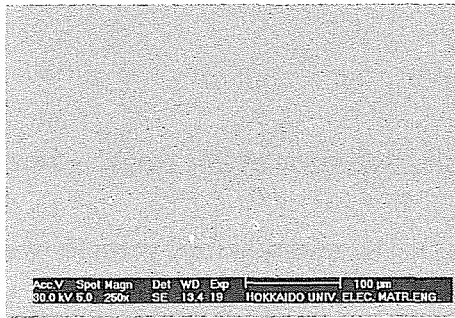
The particle size histograms made by the following procedure. First, gray-scale images of the SEM micrographs, which were saved in TIFF format, were changed to be black and white using “Scion Image” [53] to distinguish each particle. Then, the particle diameter was obtained from its circumference under the assumption that the particle was spherical.



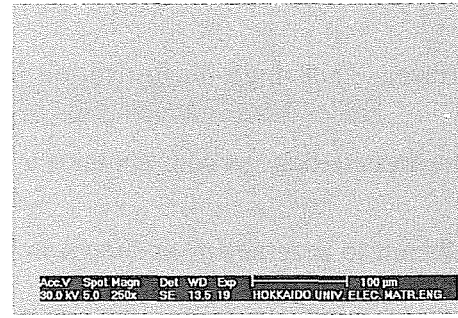
(a) vacuum



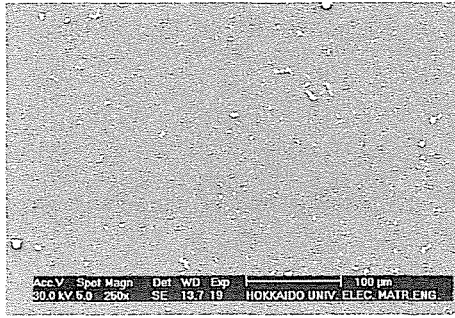
(b) 1.5 mTorr



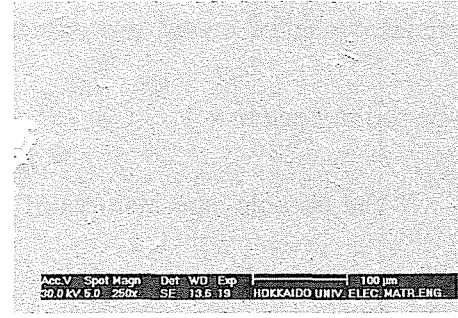
(c) 30 mTorr



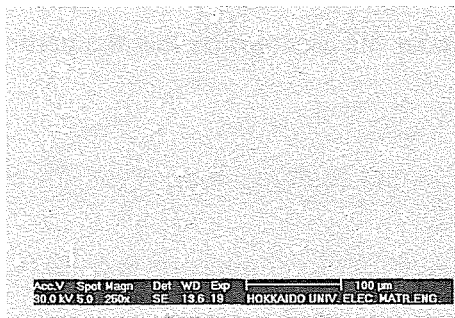
(d) 100 mTorr



(e) 400 mTorr



(f) 800 mTorr



(g) 1600 mTorr

Figure 4.4. Low-magnification ( $\times 250$ ) SEM micrographs of the a-C film surfaces deposited at  $p_{Ar} = 0 - 1600$  mTorr. The laser fluence and repetition rate were  $4 \text{ J/cm}^2$  and 30 Hz, respectively. The deposition time was 30 min.

Figure 4.6 shows the dependence of the number density of particles deposited on substrates on  $p_{Ar}$ . In this analysis, SEM micrographs of the films with a magnification of  $\times 500$  were used, and the particles with a diameter ranging from 0.3 to 4  $\mu\text{m}$ , which were deposited in a surface area of 240  $\mu\text{m} \times 139 \mu\text{m}$ , were examined. Almost of all the particles deposited at higher  $p_{Ar}$  are not spherical and seem to be formed by aggregation of the finer particles with a diameter of 50–100 nm. This aggregation was enhanced at  $p_{Ar} \geq 800 \text{ mTorr}$ . A lot of particles like a long chain with a length of  $\sim 10 \mu\text{m}$  were seen at  $p_{Ar} = 1600 \text{ mTorr}$ . Increase of the particle number density with  $p_{Ar}$  indicates that formation of nanoparticles by collision between carbon particles in an ablation plume and Ar gas atoms is enhanced as  $p_{Ar}$  increases. The histogram shown in Figure 4.7 at lower

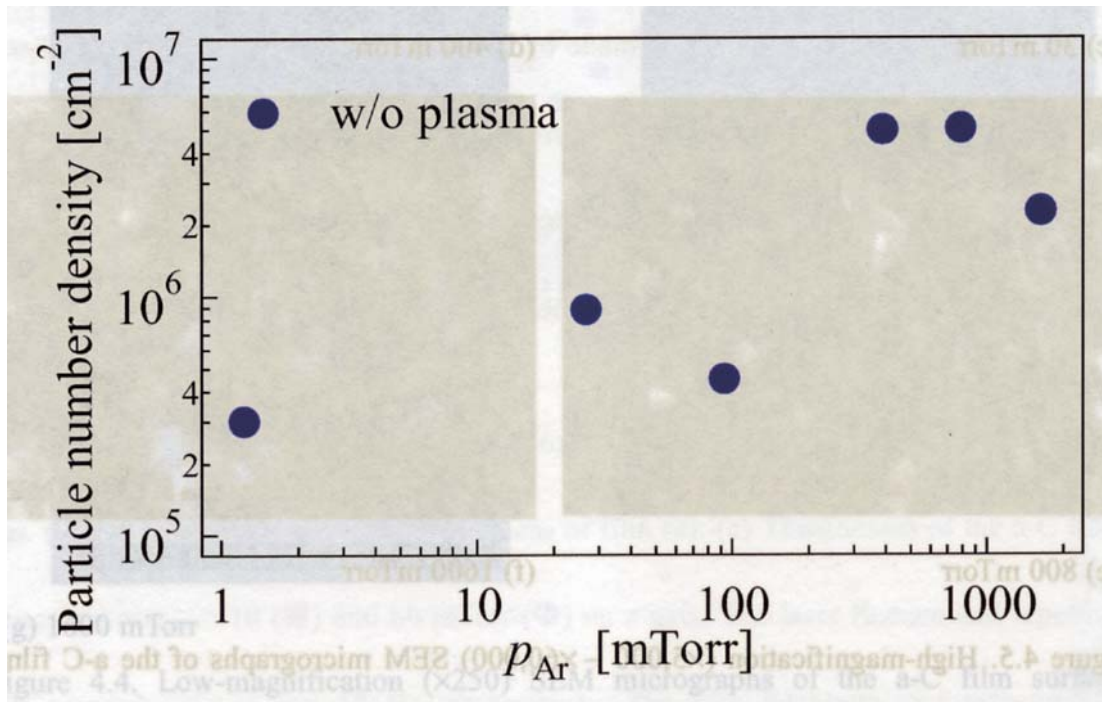


Figure 4.6. Number density of the particles deposited on substrates vs.  $p_{Ar}$ .

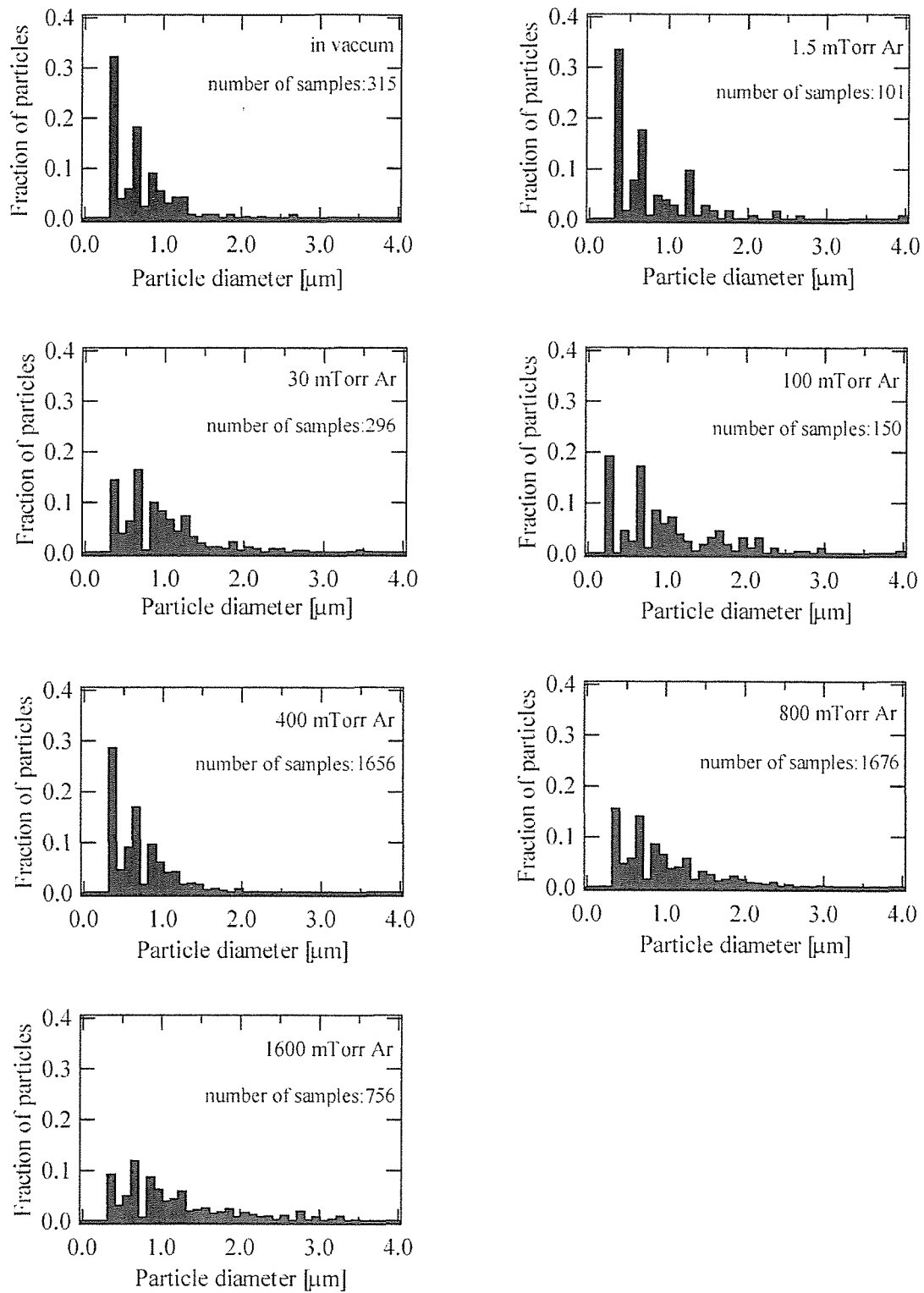


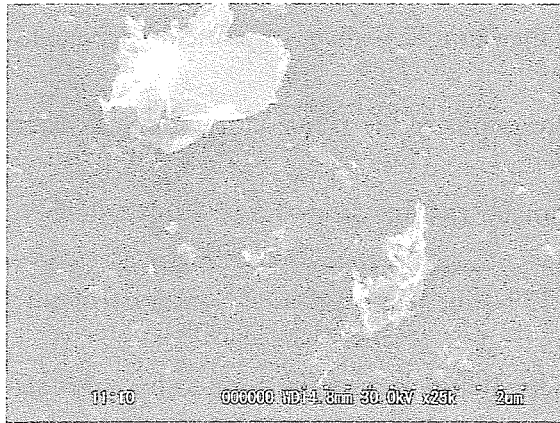
Figure 4.7. Histograms of the a-C particle size deposited on substrates.

$p_{Ar}$  ( $< 100$  mTorr) has a narrow distribution, and those at higher  $p_{Ar}$  ( $> 400$  mTorr) became broad. The particles with a diameter  $< 1 \mu\text{m}$  accounted for more than 90% in vacuum but less than 50% at  $p_{Ar} = 1600$  mTorr.

#### 4.2.1.2 AFM Analysis of a-C Film Surfaces

AFM images of the a-C film surfaces are shown in Figure 4.8. The range of  $p_{Ar}$  was between vacuum and 100 mTorr. The film surface obtained at  $p_{Ar} > 100$  mTorr was quite rough and hardly examined with an AFM. As shown in Figure 4.8, there are a lot of a-C nanoparticles on the surface. The dependence of particle size on  $p_{Ar}$  will be discussed in Section 4.3.





(a) vacuum



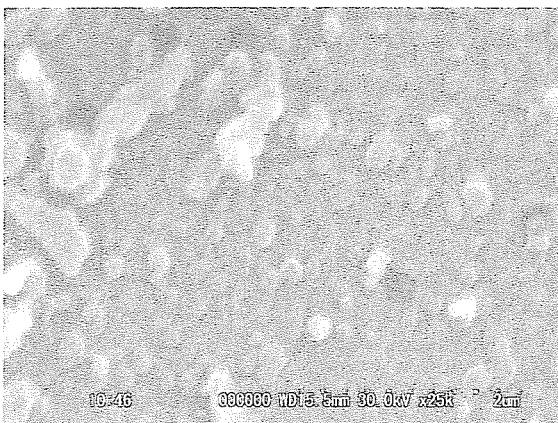
(b) 1.5 mTorr



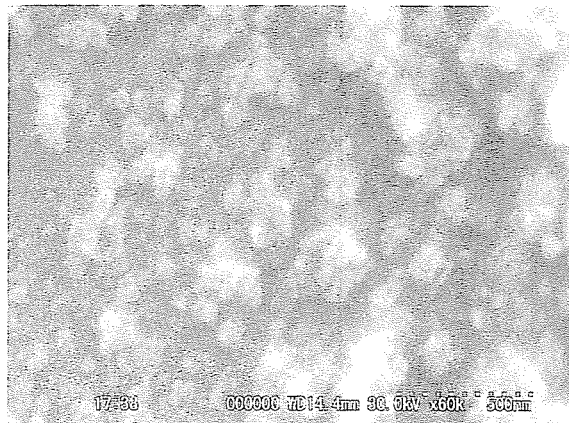
(c) 30 mTorr



(d) 400 mTorr

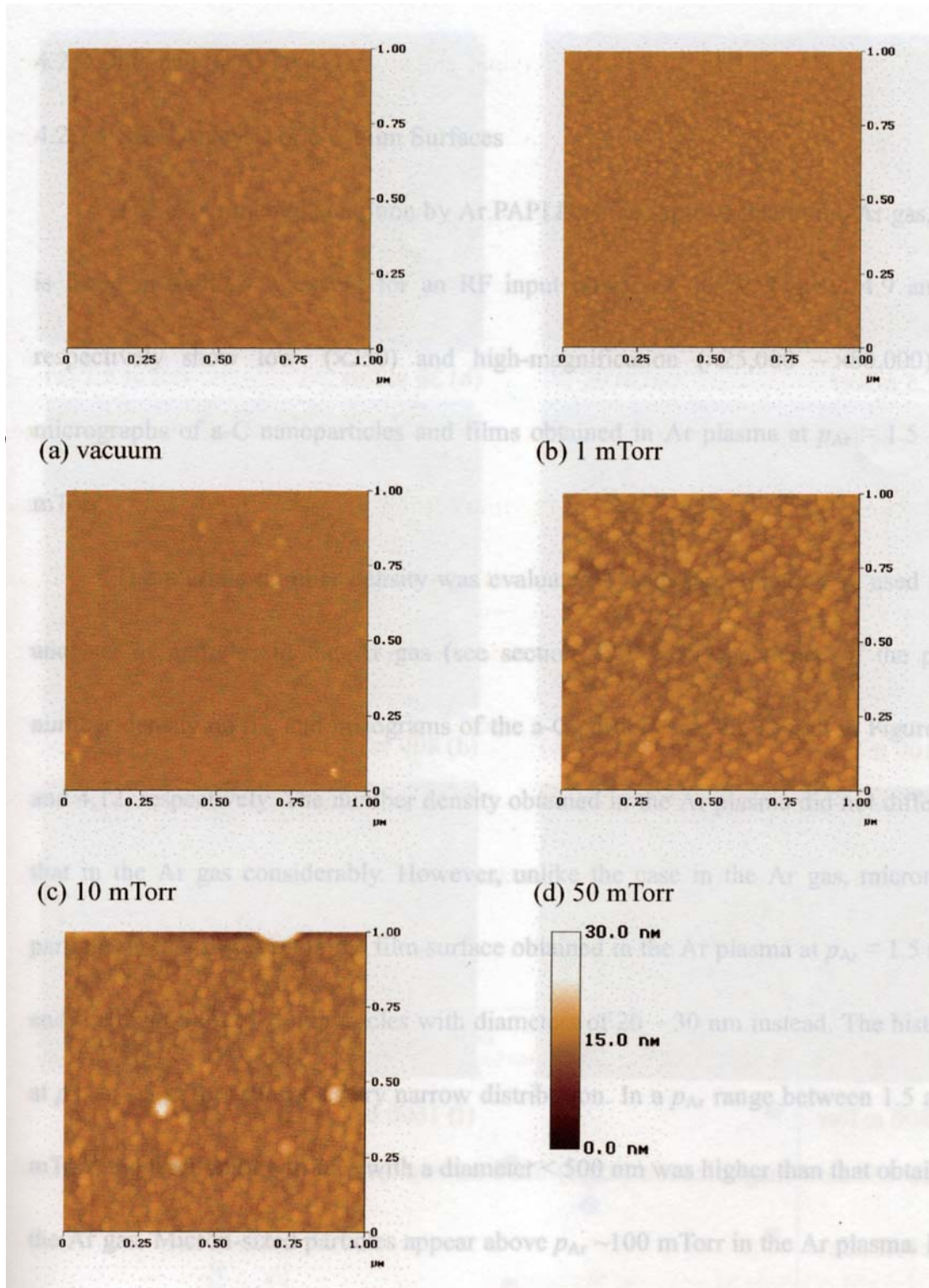


(e) 800 mTorr



(f) 1600 mTorr

Figure 4.5. High-magnification ( $\times 5,000 - \times 60,000$ ) SEM micrographs of the a-C films shown in Figure 4.4.



(e) 100 mTorr

Figure 4.8. AFM images of a-C nanoparticles deposited on substrates.

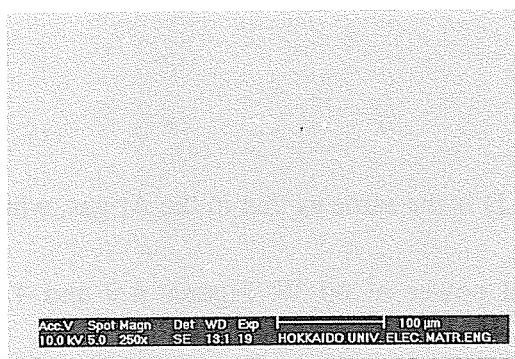


## 4.2.2 Obtained by Ar PAPLD

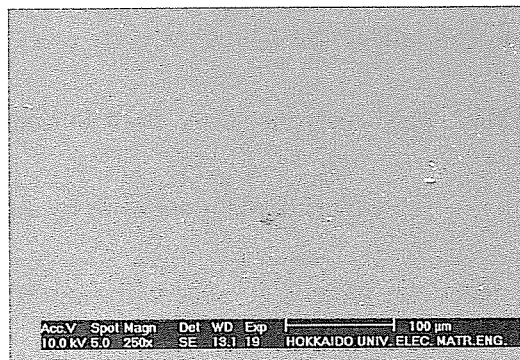
### 4.2.2.1 SEM Analysis of a-C Film Surfaces

The experimental condition by Ar PAPLD is the same as that in the Ar gas, which is listed in Table 4.1, except for an RF input power of 60 W. Figures 4.9 and 4.10 respectively show low- ( $\times 250$ ) and high-magnification ( $\times 25,000 - \times 80,000$ ) SEM micrographs of a-C nanoparticles and films obtained in Ar plasma at  $p_{\text{Ar}} = 1.5 - 1600$  mTorr.

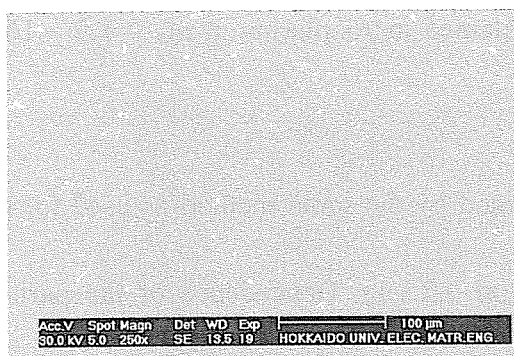
The particle number density was evaluated by the same method as used for the analysis of particles in the Ar gas (see section 4.2.1.1). Dependence of the particle number density on  $p_{\text{Ar}}$  and histograms of the a-C particle size are shown in Figures 4.11 and 4.12, respectively. The number density obtained in the Ar plasma did not differ from that in the Ar gas considerably. However, unlike the case in the Ar gas, micron-sized particles are hardly seen on the film surface obtained in the Ar plasma at  $p_{\text{Ar}} = 1.5$  mTorr, and there are a lot of nanoparticles with diameters of 20 – 30 nm instead. The histogram at  $p_{\text{Ar}} = 1.5$  mTorr shows a very narrow distribution. In a  $p_{\text{Ar}}$  range between 1.5 and 30 mTorr, the fraction of particles with a diameter  $< 500$  nm was higher than that obtained in the Ar gas. Micron-sized particles appear above  $p_{\text{Ar}} \sim 100$  mTorr in the Ar plasma. Figure 4.10 (c), which was taken from a  $45^\circ$ , shows grain boundaries on the surface of nanoparticles. The aggregation of smaller particles for synthesizing micron-sized particles will be discussed in Section 4.3.3.



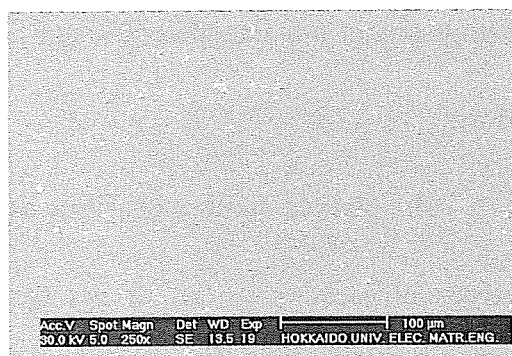
(a) 1.5 mTorr



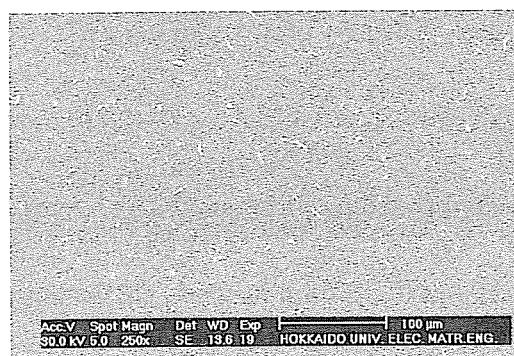
(b) 30 mTorr



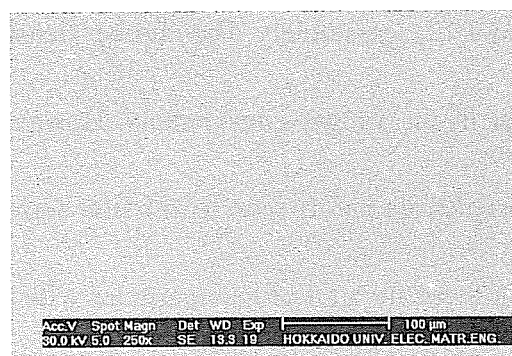
(c) 100 mTorr



(d) 400 mTorr

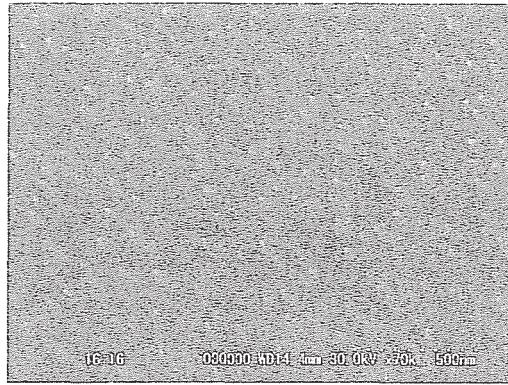


(e) 800 mTorr

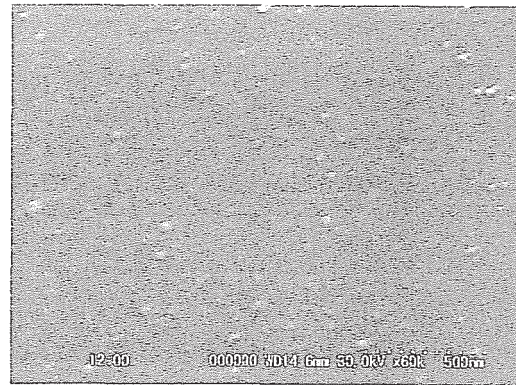


(f) 1600 mTorr

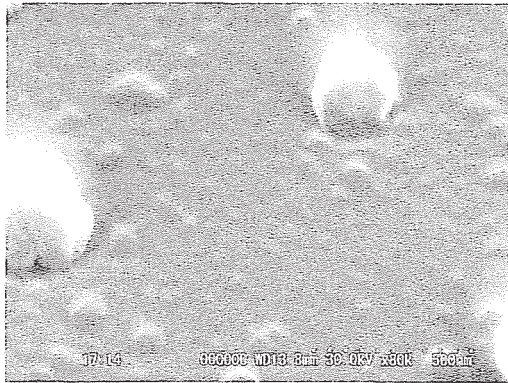
Figure 4.9. Low-magnification ( $\times 250$ ) SEM micrographs of a-C nanoparticles obtained in Ar PAPLD.



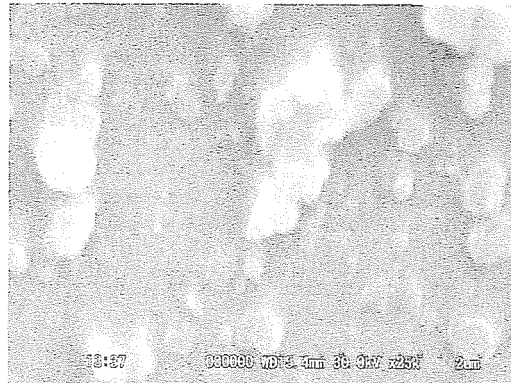
(a) 1.5 mTorr



(b) 30 mTorr

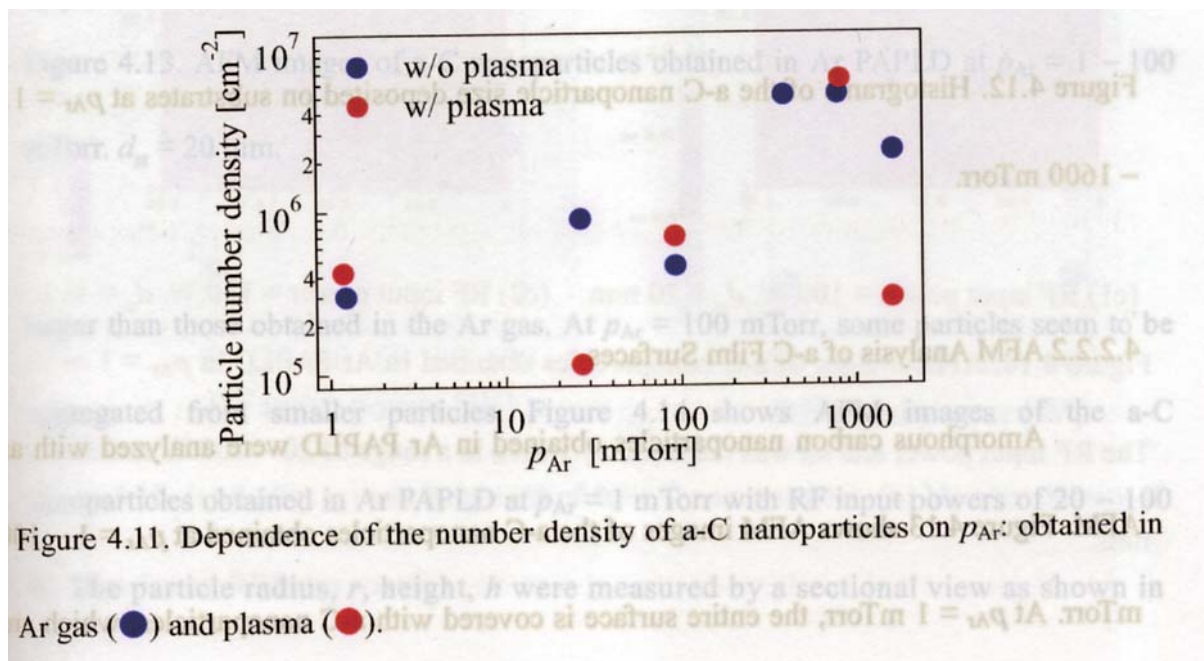


(c) 400 mTorr



(d) 800 mTorr

Figure 4.10. High-magnification ( $\times 25,000 - \times 80,000$ ) SEM micrographs of the particles shown in Figure 4.9. Figure 4.10 (c) was taken from a  $45^\circ$ .



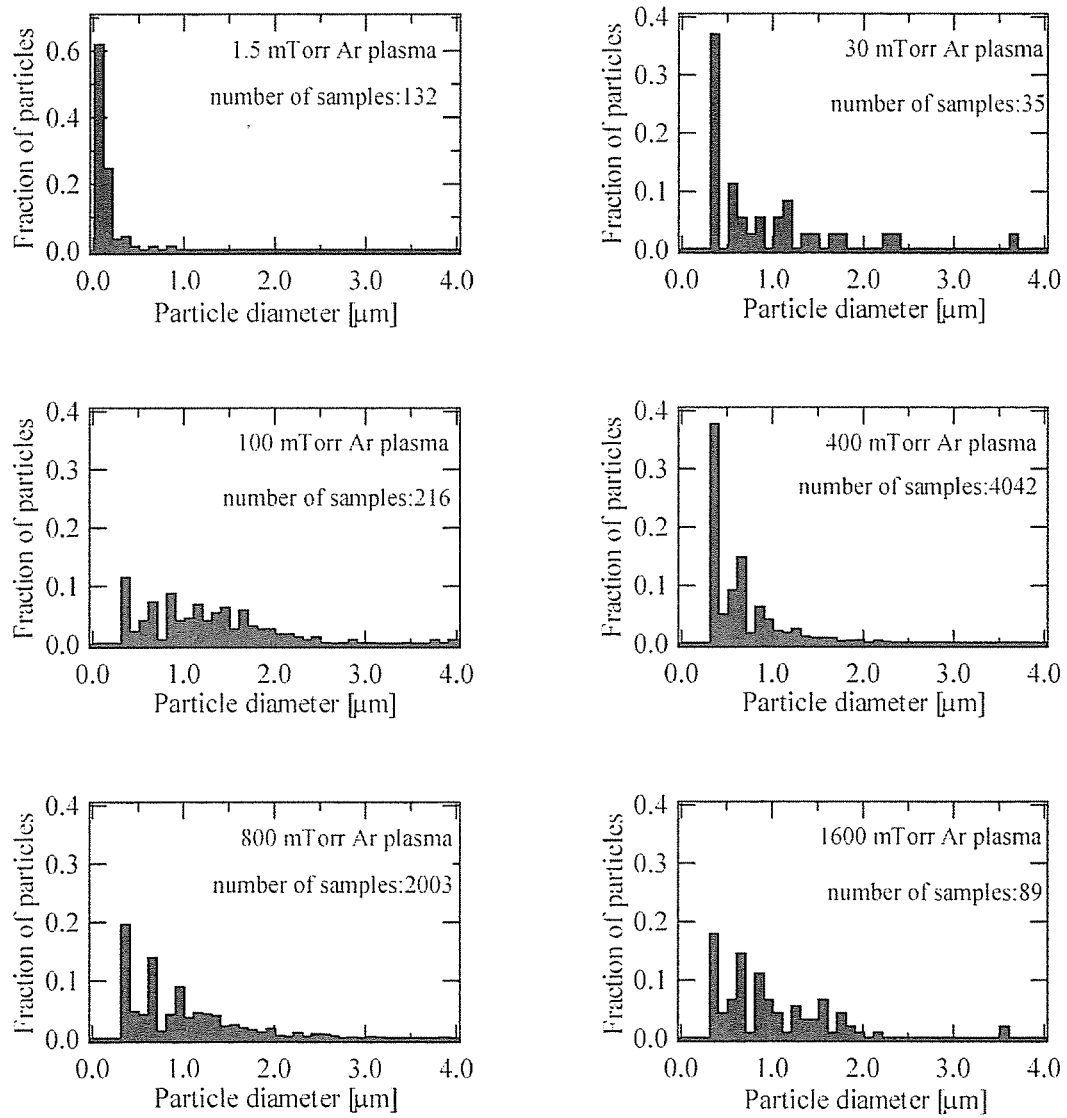
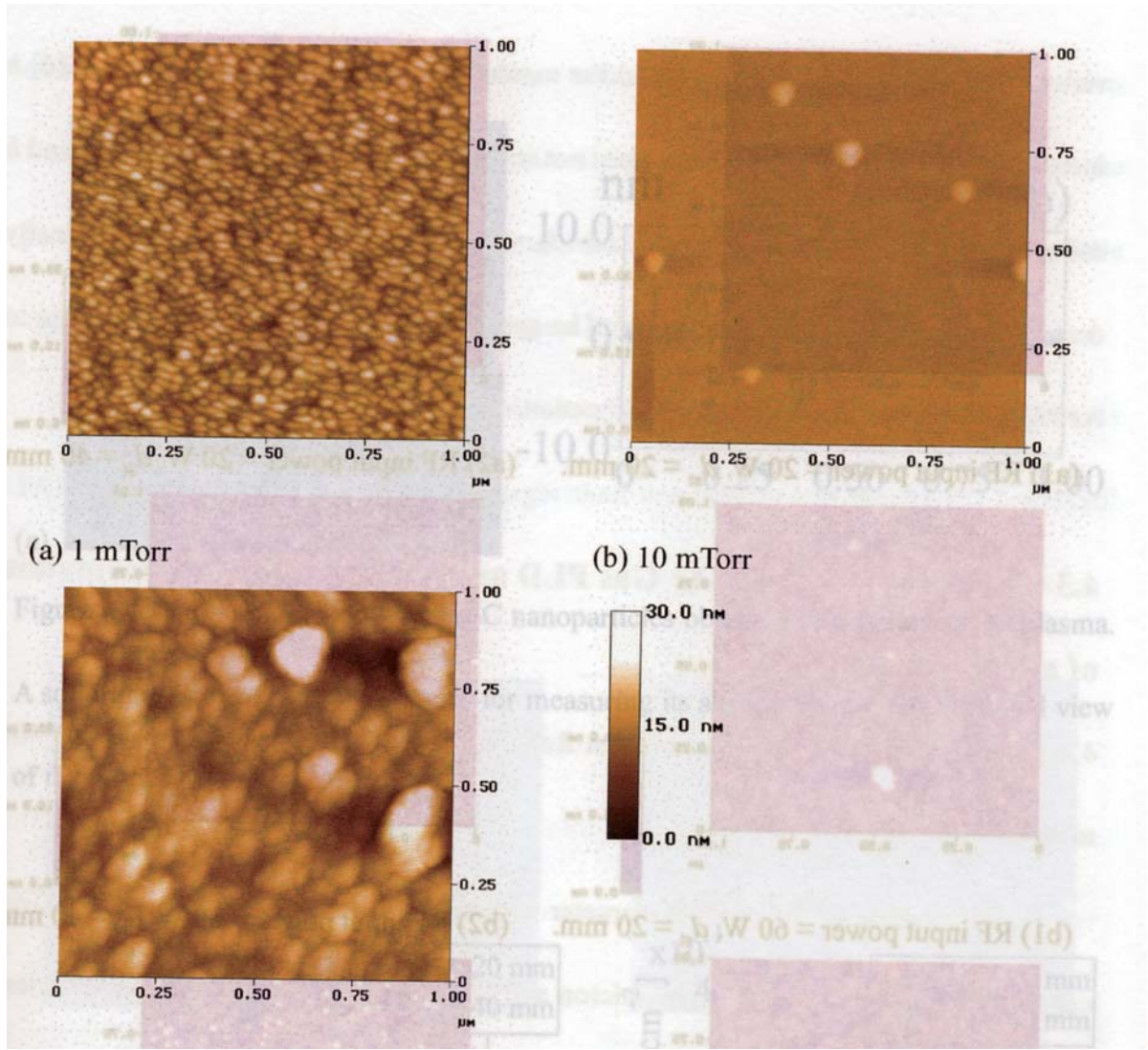


Figure 4.12. Histograms of the a-C nanoparticle size deposited on substrates at  $p_{\text{Ar}} = 1.5$  – 1600 mTorr.

#### 4.2.2.2 AFM Analysis of a-C Film Surfaces

Amorphous carbon nanoparticles obtained in Ar PAPLD were analyzed with an AFM. Figure 4.13 shows AFM images of the a-C nanoparticles obtained at  $p_{\text{Ar}} = 1$  – 100 mTorr. At  $p_{\text{Ar}} = 1$  mTorr, the entire surface is covered with a-C nanoparticles, which are





(c) 100 mTorr

Figure 4.13. AFM images of a-C nanoparticles obtained in Ar PAPLD at  $p_{Ar} = 1 - 100$  mTorr.  $d_{st} = 20$  mm.

larger than those obtained in the Ar gas. At  $p_{Ar} = 100$  mTorr, some particles seem to be aggregated from smaller particles. Figure 4.14 shows AFM images of the a-C nanoparticles obtained in Ar PAPLD at  $p_{Ar} = 1$  mTorr with RF input powers of 20 – 100 W. The particle radius,  $r$ , height,  $h$  were measured by a sectional view as shown in

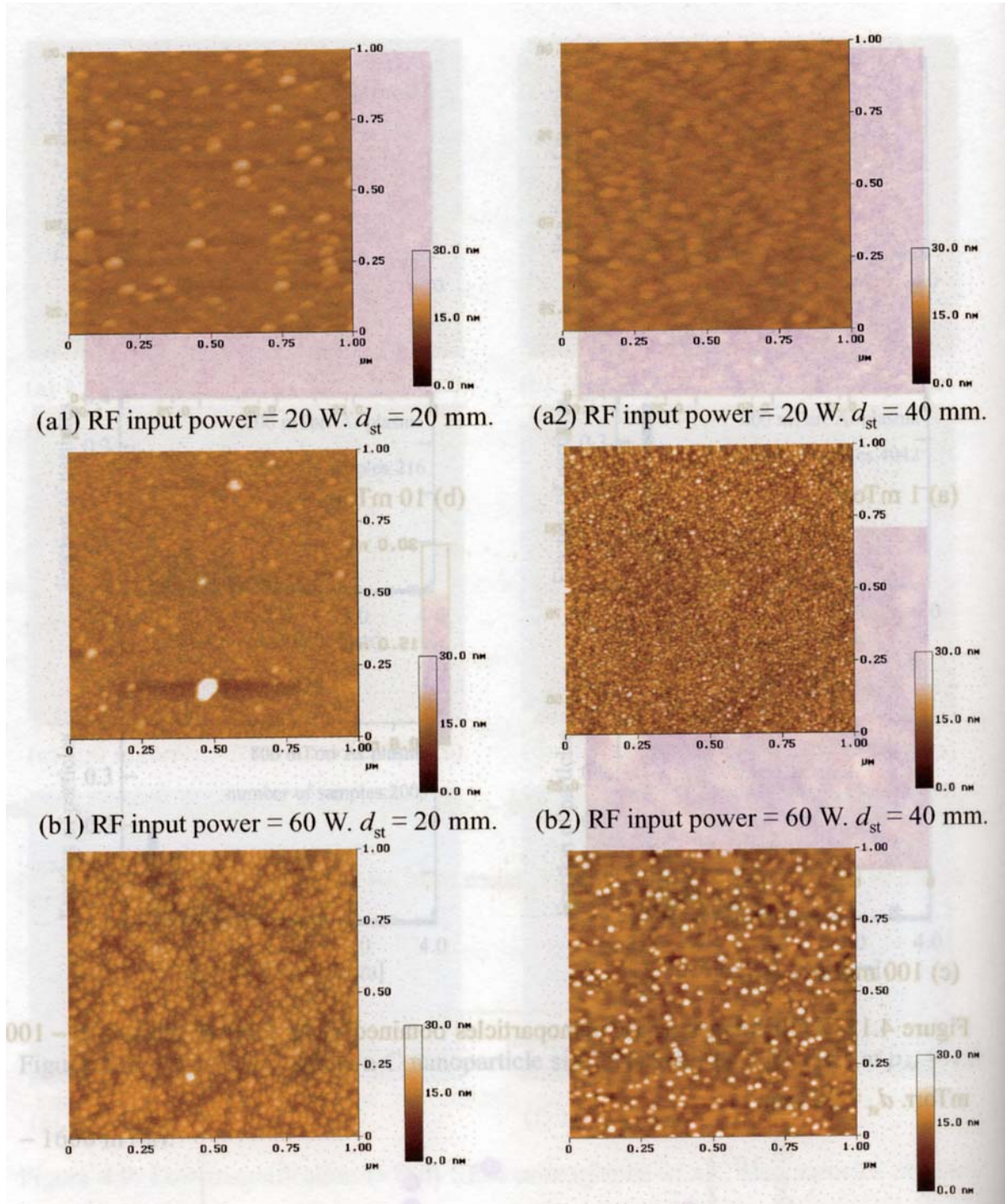


Figure 4.14. AFM images of a-C nanoparticles obtained in Ar PAPLD at  $p_{Ar} = 1$  mTorr.

The RF input power and  $d_{st}$  was respectively varied in a range of 20 – 100 W and 20 – 40 mm.

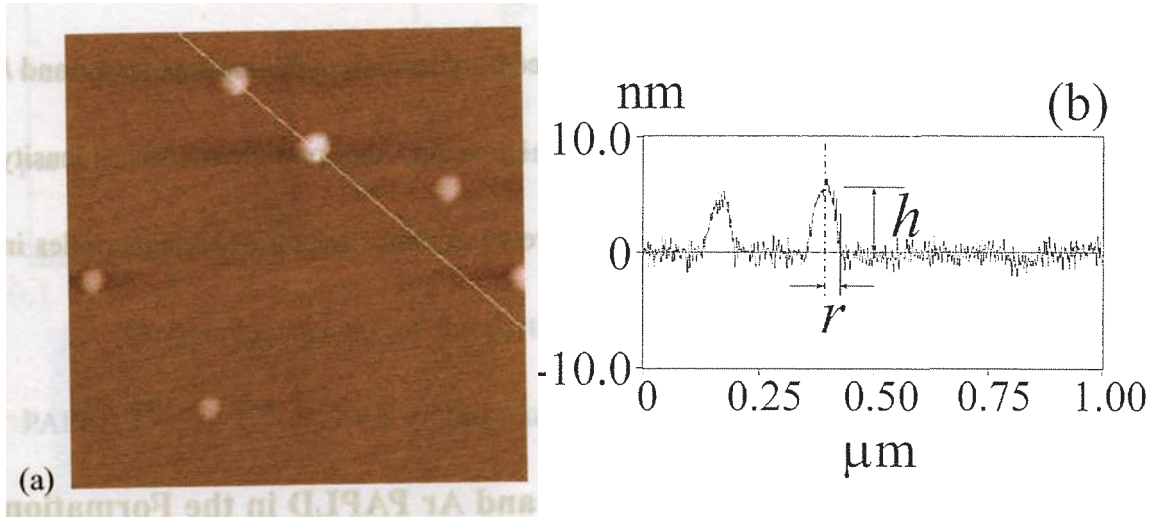


Figure 4.15. (a) An AFM image of a-C nanoparticles obtained in a 10-mTorr Ar plasma.

A solid line cuts out the two particles for measuring its sectional view. (b) Sectional view of the particles.

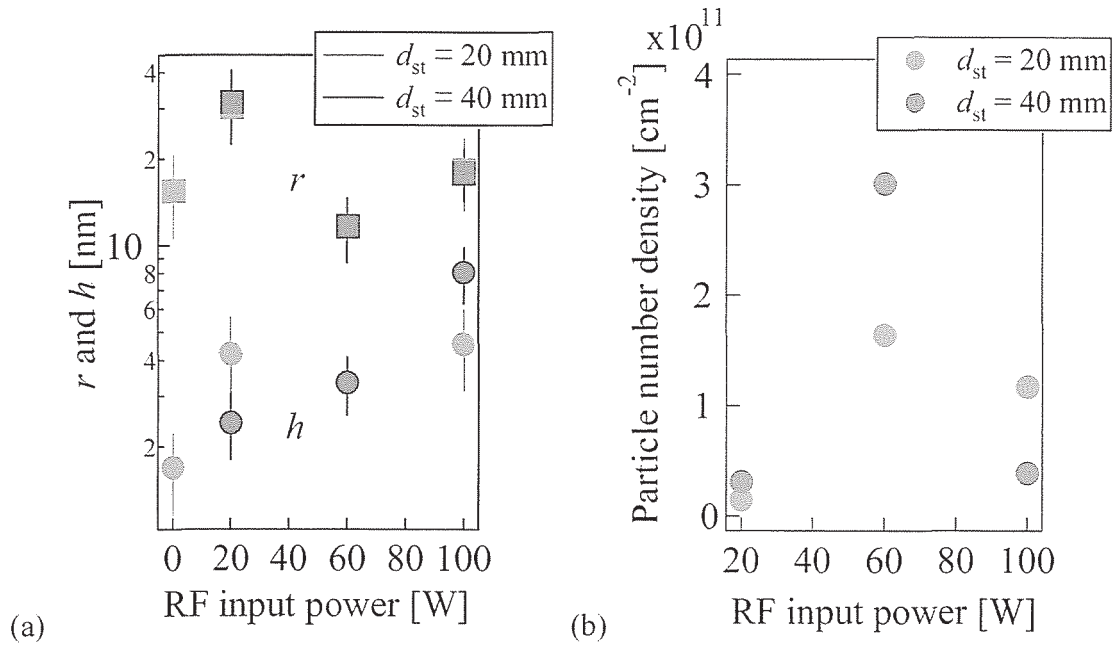


Figure 4.16. (a) Radius ( $r$ ) and height ( $h$ ) of the a-C nanoparticles. (b) Number density of the particles vs. RF input power.



view as shown in Figure 4.15.  $r$ ,  $h$  and the number density are shown in Figure 4.16.  $h$  increased with RF input power, but  $r$  does not seem to depend on RF input power.  $r$  and  $h$  did not show a strong dependence on  $d_{st}$ . However, the particle number density drastically changed on RF input power. The growth mechanism of a-C nanoparticles in Ar PAPLD will be discussed in the next section.

### **4.3 Comparison between Ar Gas PLD and Ar PAPLD in the Formation of a-C Nanoparticles**

#### **4.3.1 Formation of a-C Nanoparticles at Relatively High Ar Gas Pressures ( $p_{Ar} \geq 400$ mTorr)**

Distribution of the particle diameter obtained by Ar PAPLD at  $p_{Ar} = 400$  mTorr can be divided into two categories: micron and 100s nm. The acicular and not spherical particles with a diameter of  $\sim \mu\text{m}$  were seen in both the Ar gas and plasma (see Figures 4.4 (e) and 4.9 (d)). But, the spherical particles of 100s nm in diameter were seen only in the Ar plasma (see Figures 4.5 (d) and 4.10 (c)).

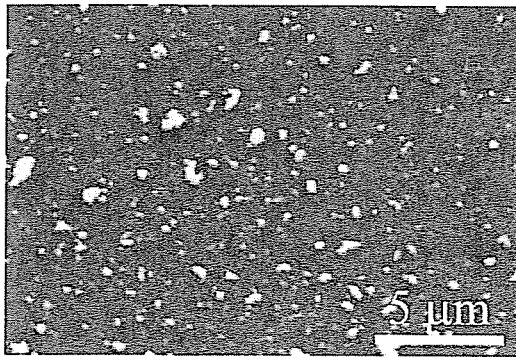
In a similar way of the 400-mTorr case, at  $p_{Ar} = 800$  mTorr, a lot of particles with micron and 100s nm in diameter were obtained in the Ar plasma (see Figure 4.9 (e)). Some micron-sized particles are not spherical but elongated and seem to form by aggregation of the smaller particles (see Figure 4.10 (d)).

Figure 4.17 show SEM micrographs of the a-C nanoparticles obtained in the

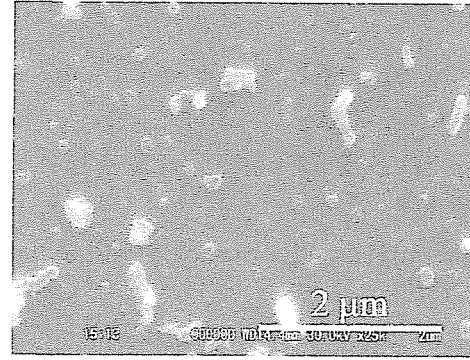


400-mTorr Ar gas and plasma.  $d_{st}$  was set to be 20 mm because no particles and films were deposited on substrate for  $d_{st} = 35$  mm at this pressure due to collisions between the particles in LA plume and Ar gas atoms. Makimura, et al also reported that a plume cannot expand to a long distance in rare gases at pressures  $\geq \sim 1$  Torr [23].

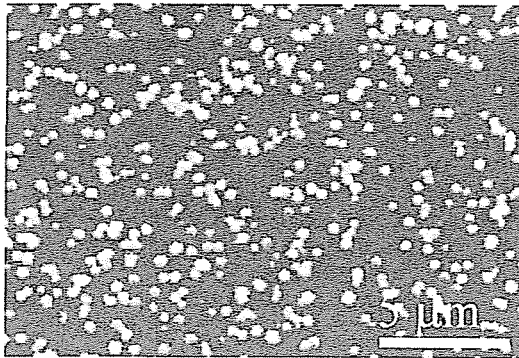
The number density of the particles, which were obtained in the 400-mTorr Ar PAPLD ( $\sim 5.0 \times 10^8 \text{ cm}^{-2}$ ) is slightly larger than that obtained in the Ar gas ( $\sim 4.5 \times 10^8$



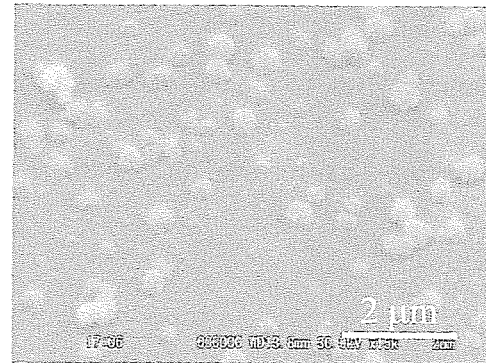
(a1) Ar gas



(a2) Ar gas



(b1) Ar plasma



(b2) Ar plasma

Figure 4.17. SEM micrographs of a-C nanoparticles obtained in (a) Ar gas and (b) Ar plasma at  $p_{Ar} = 400$  mTorr.  $d_{st} = 20$  mm. Figures (a2) and (b2) were taken at an angle of  $45^\circ$  from the substrate.

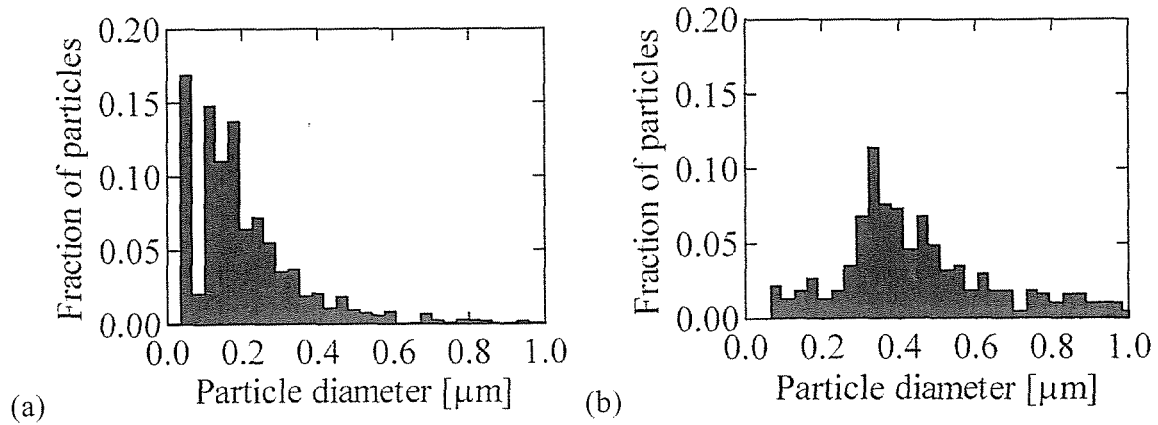


Figure 4.18. Histograms of the a-C nanoparticle size obtained in (a) Ar gas and (b) Ar plasma at  $p_{\text{Ar}} = 400$  mTorr. The RF input power was 60 W.

$\text{cm}^{-2}$ ). But, the shapes of particles are totally different. As shown in Figure 4.17 (b2), almost of all the particles are spherical, and this spherical particle seems to be aggregated by several smaller particles with a diameter of  $\sim 10$  nm.

Figure 4.18 show the histograms of a-C nanoparticle size obtained in Ar gas and plasma. In the Ar gas, more than 70% of the particles were smaller than  $0.3 \mu\text{m}$  in diameter. But, in the plasma, more than 70% of the particles were larger than  $0.3 \mu\text{m}$  in diameter. This result indicates that the plasma played an important role in growing the particles.

#### 4.3.2 Formation of a-C Nanoparticles at Relatively Low Ar Gas Pressures ( $p_{\text{Ar}} \leq 100$ mTorr)

Figure 4.19 show AFM images of the a-C film surface deposited in Ar gas and

plasma at  $p_{\text{Ar}} = 1$  and 100 mTorr. In the 1-mTorr Ar gas, small particles of  $\sim 10$  nm in diameter are seen in parts on the surface. But in the 1-mTorr Ar plasma, the entire surface was covered with a-C nanoparticles. These particles seem to exist without any

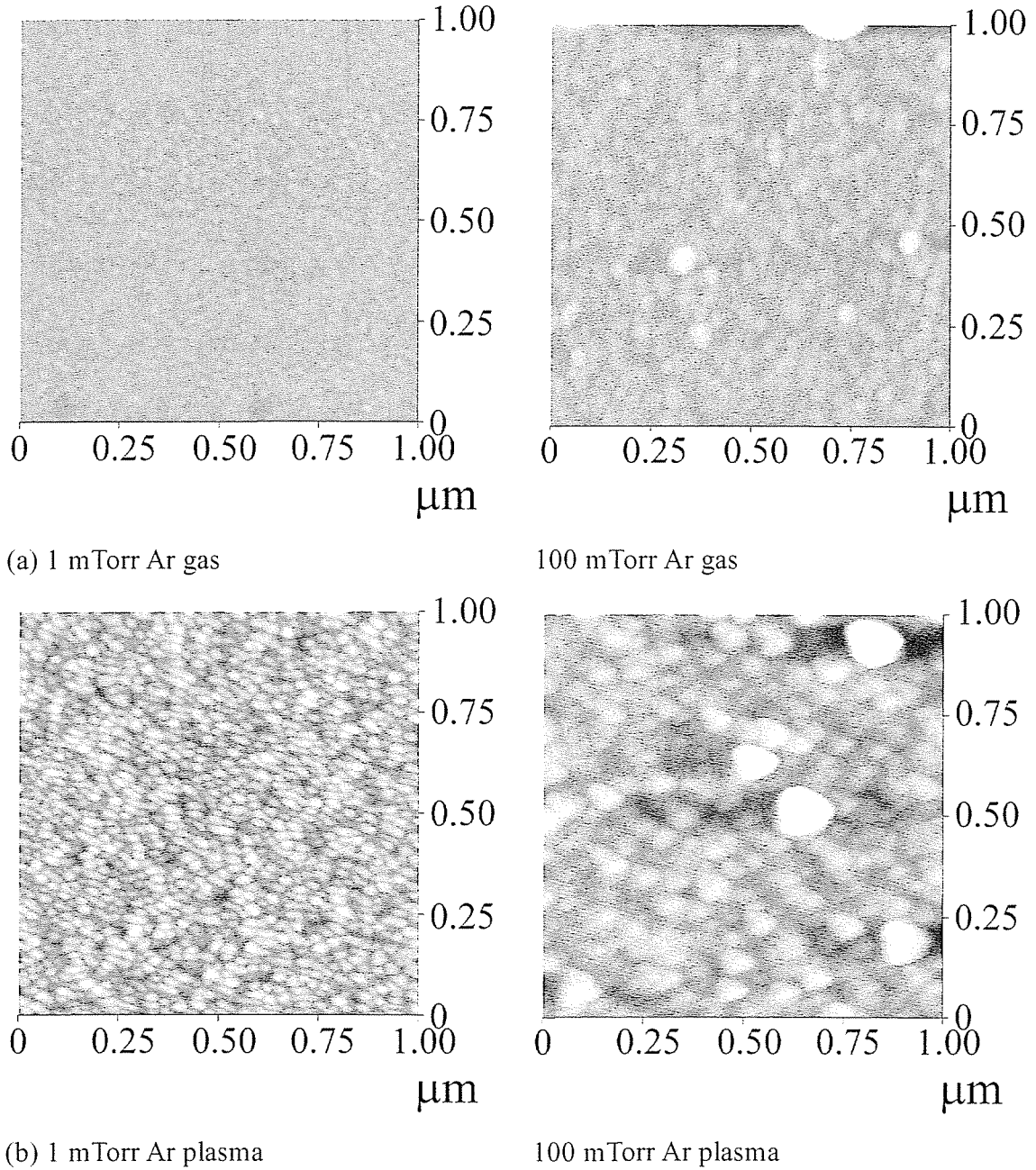


Figure 4.19. AFM images of the a-C nanoparticles obtained in (a) Ar gas and (b) Ar plasma at  $p_{\text{Ar}} = 1$  and 100 mTorr.

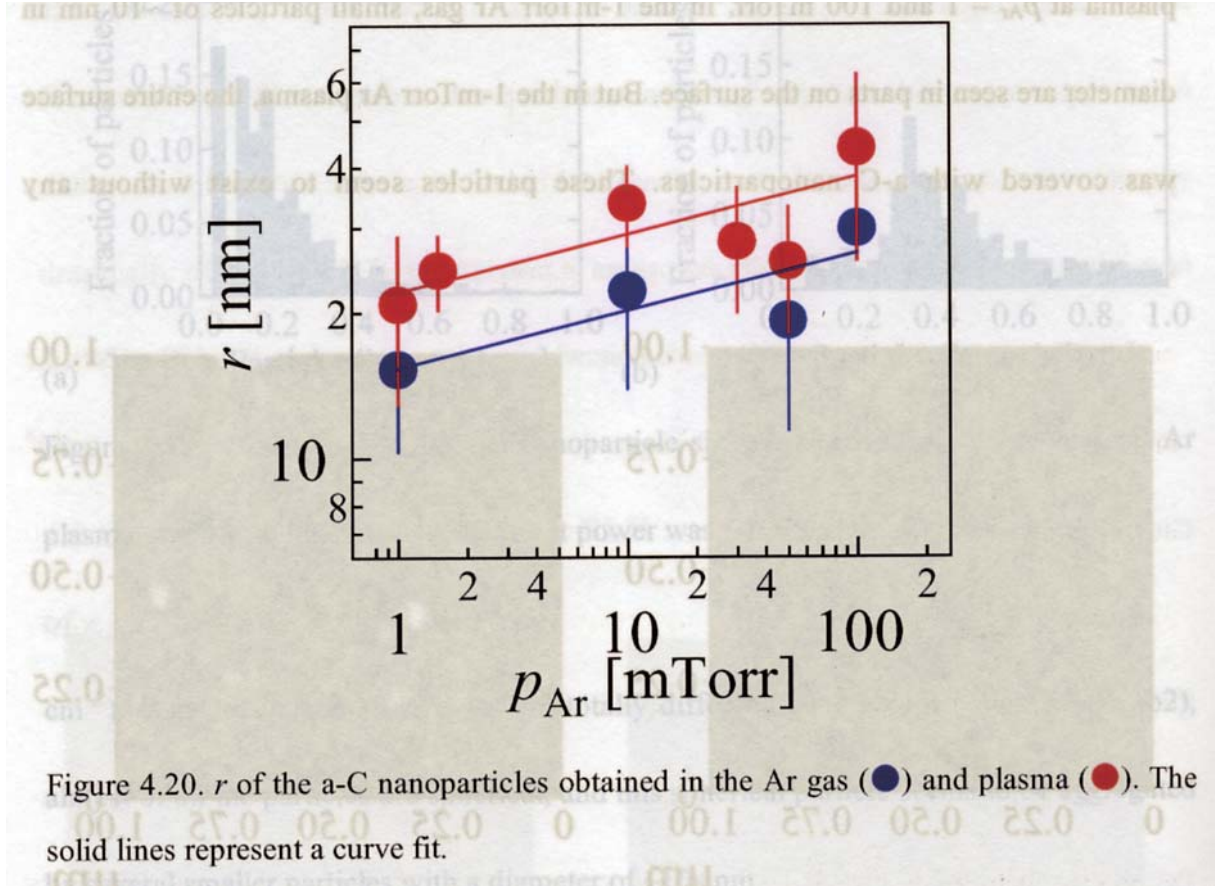


Figure 4.20.  $r$  of the a-C nanoparticles obtained in the Ar gas (●) and plasma (●). The solid lines represent a curve fit.

coalescence. The particle number density  $n_p$  was counted from the AFM images. At  $p_{\text{Ar}} = 1$  mTorr,  $n_p$  in the Ar gas was  $\sim 7.0 \times 10^{10} \text{ cm}^{-2}$ , and  $n_p$  in the Ar plasma was  $\sim 7.8 \times 10^{10} \text{ cm}^{-2}$ . Though appreciable difference in  $n_p$  between the Ar gas and plasma is not seen, the nanoparticle size obtained in the Ar plasma is larger than that in the Ar gas. At  $p_{\text{Ar}} = 100$  mTorr,  $n_p$  is  $\sim 2.2 \times 10^{10} \text{ cm}^{-2}$  in the Ar plasma and  $\sim 3.7 \times 10^{10} \text{ cm}^{-2}$  in the Ar gas, and smaller than those at  $p_{\text{Ar}} = 1$  mTorr. This may be due to the coalescence of smaller nanoparticles.

Figure 4.20 shows the nanoparticle radius  $r$  as a function of  $p_{\text{Ar}}$ .  $r$  increased in proportion with  $p_{\text{Ar}}^{1/8}$  for the Ar gas and  $p_{\text{Ar}}^{1/9}$  for the Ar plasma.  $r$  in the Ar plasma was  $\sim 1.5$  times larger than that in the Ar gas. This result indicates that the plasma promotes the aggregation of a-C nanoparticles effectively.

#### 4.3.3 Growth Model of a-C Nanoparticles by PAPLD

It was shown that growth of a-C nanoparticles was enhanced by applying Ar plasma to PLD. This mechanism is explained by the following discussion performed in RF SiH<sub>4</sub> plasma chemical vapor deposition (CVD) [54-60]. In RF SiH<sub>4</sub> plasmas, Si nanoparticles grow up in the following stage: (1) First, Si atoms are clusterized, and the clusters grow to a few nanometers in the plasma in the first ~100 ms. (2) The particles begin to aggregate with each other by Coulomb attractive force between negatively and positively charged particles, and rapidly grow to a diameter of 50 – 60 nm. (3) Finally, the aggregation process stops, however the particles continue to grow by molecular sticking because almost all of the particles are charged negatively in this stage [58]. This model is illustrated in Figure 4.21. Shiratani, et al revealed that when the silicon particles grew to ~10 nm in diameter, they began to aggregate with each other [60].

As referring this model, growth of a-C nanoparticles in PAPLD is explained as follows: (1) Firstly carbon atoms, molecules and ions ( $C_n$  and  $C_n^+$  ( $n = 1-3$ )) are ablated and begin to nucleate by radical reaction [12]. (2) The nucleated particles continue to grow and become negatively charged ( $C_n^-$ ) in the plasma [58]. (3) Then  $C_n^+$  and  $C_n^-$  are attracted with each other due to Coulomb force and aggregated.

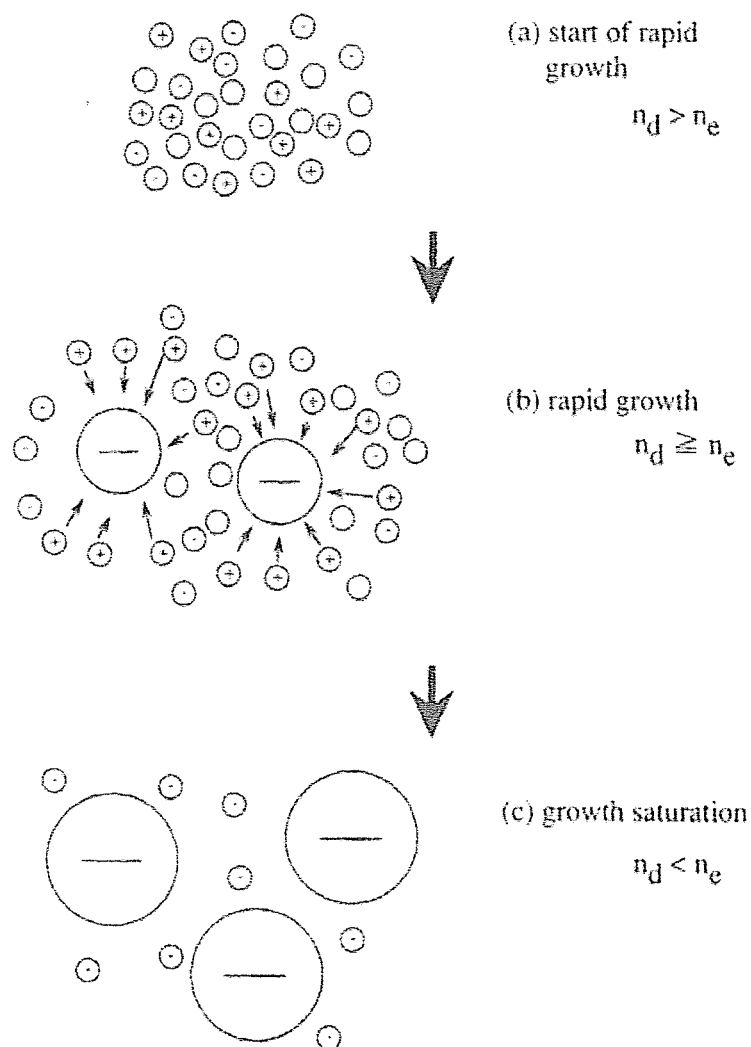


FIG. 5. Coagulation model in rapid growth phase. (a) Negatively charged, positively charged and neutral particulates of nearly the same size coexist at start of rapid growth. Particulate density  $n_d$  is much higher than electron density  $n_e$ . (b) Positively charged small particulates are coagulated selectively with negatively charged larger particulates. (c) Coagulation rate decreases considerably in growth saturation phase, because most particulates are charged negatively.

Figure 4.21. An illustration of aggregation model for nanoparticle growth in  $\text{SiH}_4$  plasma

[60].  $n_d$  and  $n_e$  denote particulate and electron densities, respectively.

## 4.4 Reduction of Micron-Sized Carbon Droplets on substrates by PAPLD

### 4.4.1 Generation and Deposition of Droplets

To fabricate thin films by PLD for commercial use, it is crucial to avoid depositing micron-sized droplets on substrate. Though a number of techniques have been tested for this purpose, the problem still remains. In this section, the reduction of droplets by PAPLD is presented.

The experimental conditions were as follows: laser fluence =  $4 \text{ J/cm}^2$ ;  $d_{\text{st}} = 35 \text{ mm}$ ; laser repetition rate = 30 Hz; deposition time = 30 min;  $T_{\text{sub}} = \text{room temperature}$ . Ar and  $\text{O}_2$  gases were used. Figure 4.22 show SEM micrographs of a-C film surface deposited in vacuum. A lot of particles with diameters of  $\sim 100 \text{ nm}$  are seen on the surface. Some particles are larger than  $1 \mu\text{m}$ . Their shape is abrasive and irregular.

Particles in a laser ablation plume may be categorized as follows [1]: (1) exfoliation from the bumpy target surface due to laser irradiation, (2) solidification of

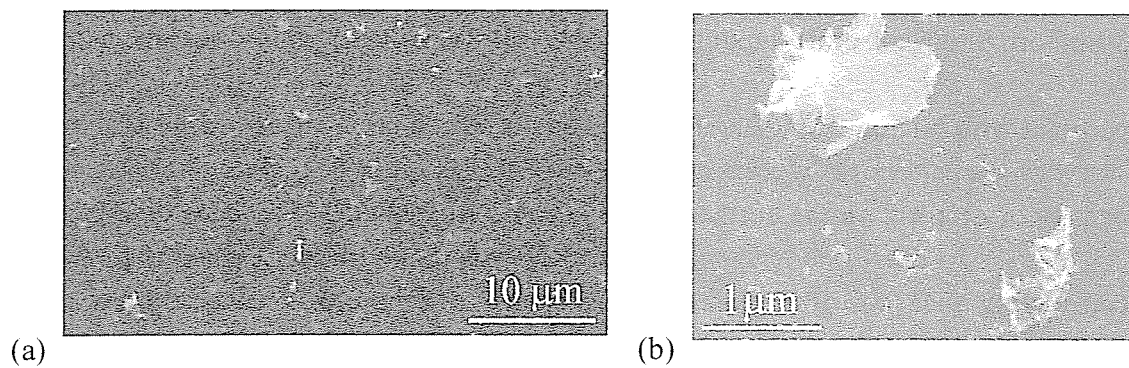


Figure 4.22. SEM images of a-C thin film deposited in vacuum.

molten droplets generated from the super-heated sub-surface layer on the target, and (3) nucleation of ablated atoms due to cooling down by collision with ambient gas atoms during their flight [61]. Let me call the particles generated by (1) and (2) “droplets” and discuss in this section.

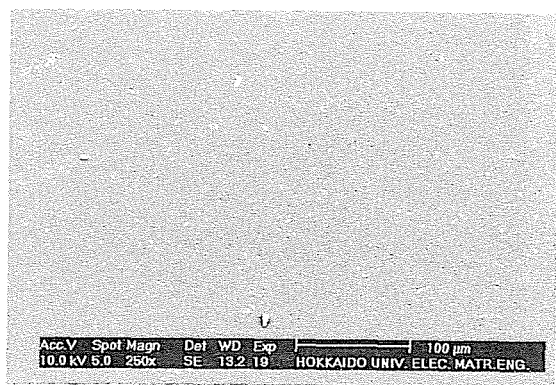
It was reported that when ArF laser ( $\lambda=193$  nm) is used, ablated carbon species are mostly  $C_n$  and  $C_n^+$  with  $n = 1 - 3$  [12, 13]. Then, it is thought that, in vacuum, hardly any nucleation of particles is generated. It seems reasonable that most droplets deposited in vacuum are provided by exfoliation.

Generation of molten droplets from carbon target is less than that from metals and other materials whose melting point is lower than that of carbon. But, at high laser fluence, molten droplets of carbon can be seen as shown in Figure 4.5 (b).

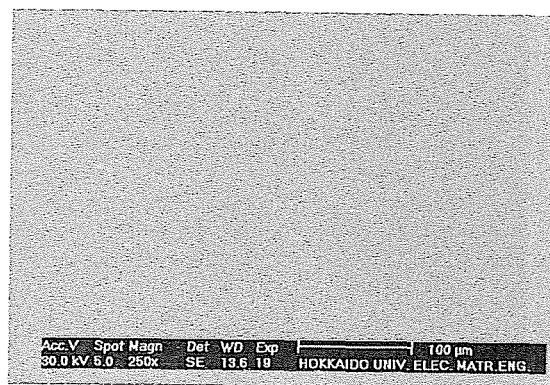
#### 4.4.2 Effect of RF Ar and O<sub>2</sub> Plasma on Reduction of Droplet Number Density on Substrates

Figures 4.23 and 4.24 show SEM micrographs of a-C films deposited in a 30-mTorr Ar plasma at RF input powers of 0 – 60 W. It clearly shows that the number of particles with micron-diameters decreased as the RF input power increased. The number density of droplets on the surface was evaluated from the SEM images of Figure 4.24 considering each a-C film thickness and shown in Figure 4.25. The number density decreased as the RF input power increased.

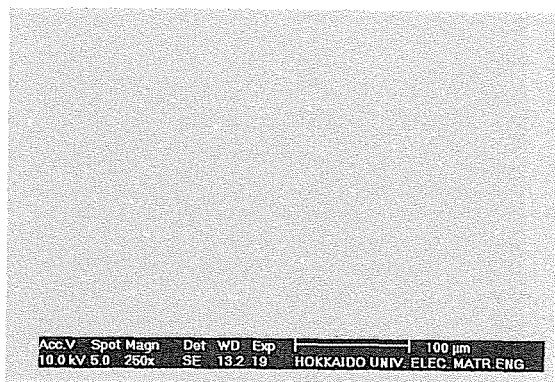




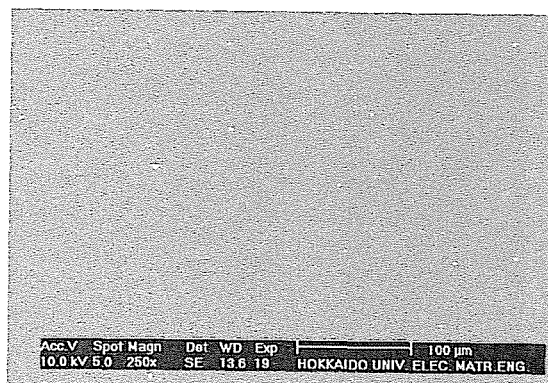
(a) 0 W



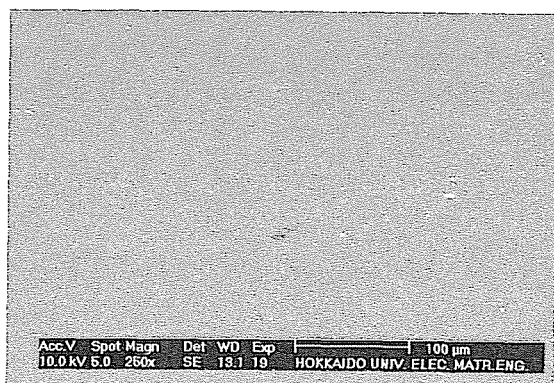
(b) 10 W



(c) 20 W

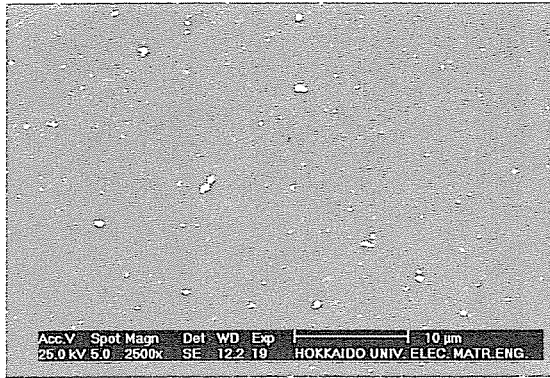


(d) 40 W

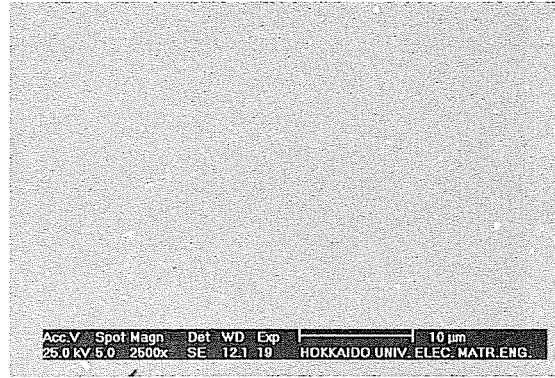


(e) 60 W

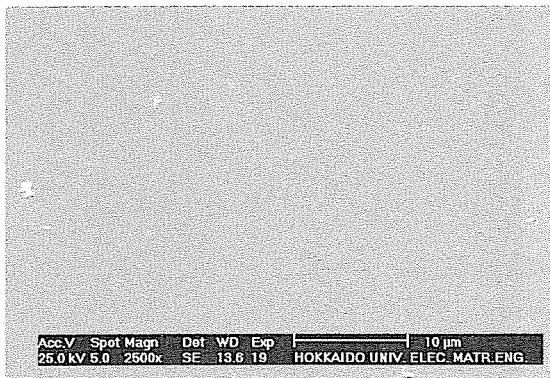
Figure 4.23. Low-magnification ( $\times 250$ ) SEM micrographs of a-C films deposited in a 30-mTorr Ar plasma. The RF input power was varied from 0 to 60 W.



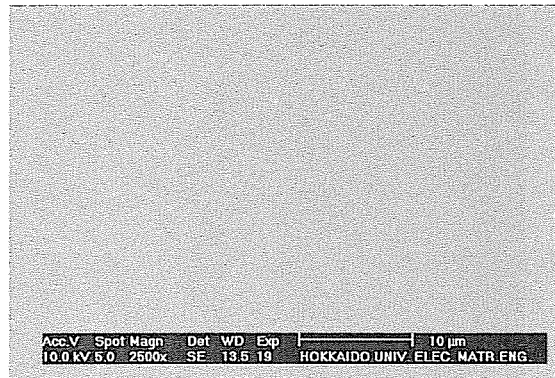
(a) 0 W



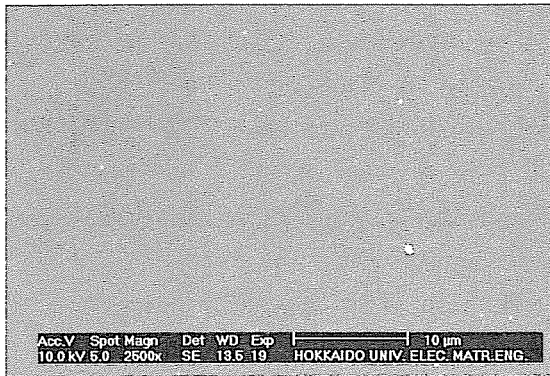
(b) 10 W



(c) 20 W



(d) 40 W



(e) 60 W

Figure 4.24. High-magnification ( $\times 2,500$ ) SEM micrographs of Figure 4.23.

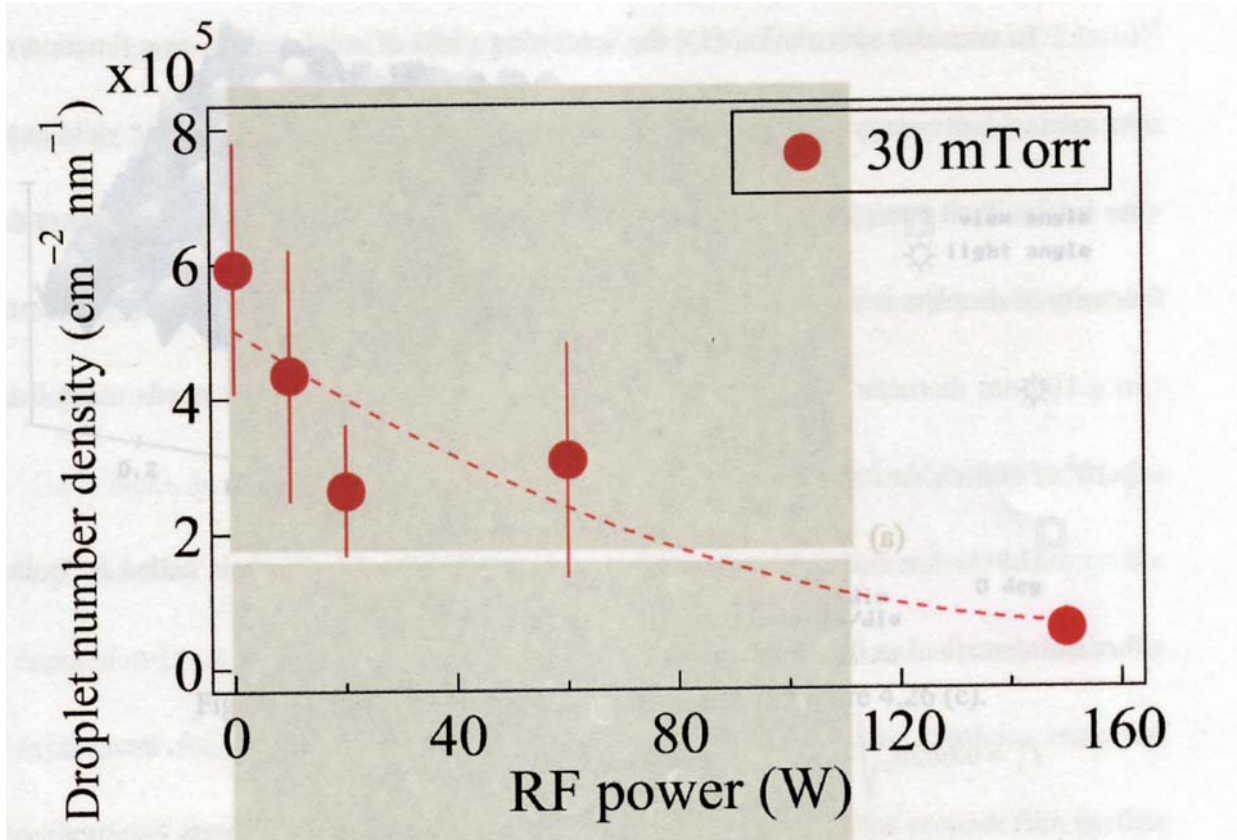


Figure 4.25. Number density of droplets deposited in 30-mTorr Ar plasmas vs. RF input power. The droplets with a diameter  $\geq 1 \mu\text{m}$  were counted, and the number density was evaluated by division of each film thickness.

Effect of plasma on reduction of the droplets was also confirmed by oxygen PAPLD. Figure 4.26 shows SEM micrographs of the films deposited in (a) vacuum, (b) oxygen ( $\text{O}_2$ ) gas and (c)  $\text{O}_2$  plasma at an  $\text{O}_2$  gas pressure,  $p_{\text{O}_2} = 0.4 \text{ mTorr}$  at  $T_{\text{sub}} \sim 400^\circ\text{C}$ . As it is clearly seen, there are a lot of nanoparticles on the film surface obtained in vacuum and  $\text{O}_2$  gas. In particular, about 300-nm-sized particles are seen on the film deposited in the  $\text{O}_2$  gas. In contrast, the film surface deposited in the  $\text{O}_2$  plasma is quite smooth.

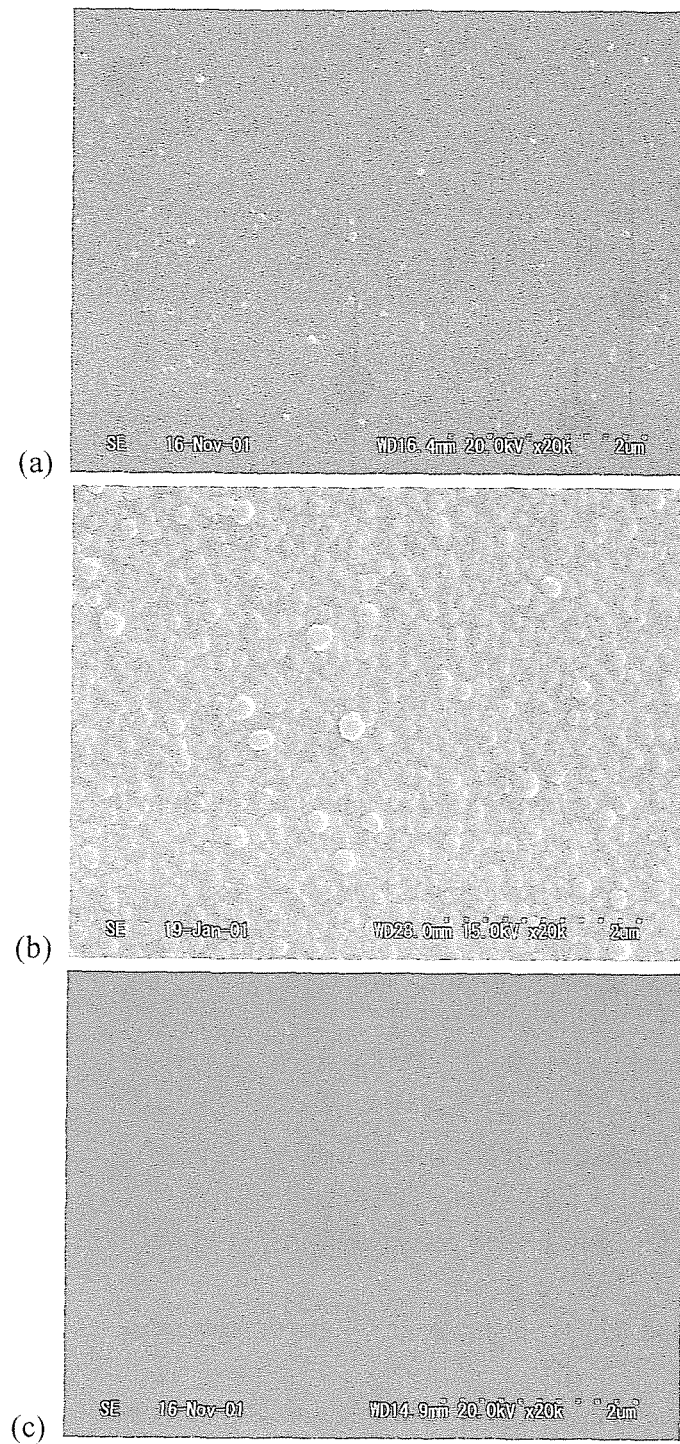


Figure 4.26. SEM micrographs of the a-C film surfaces deposited in (a) vacuum, (b) O<sub>2</sub> gas and (c) O<sub>2</sub> plasma. The experimental results are detailed in Section 4.6.

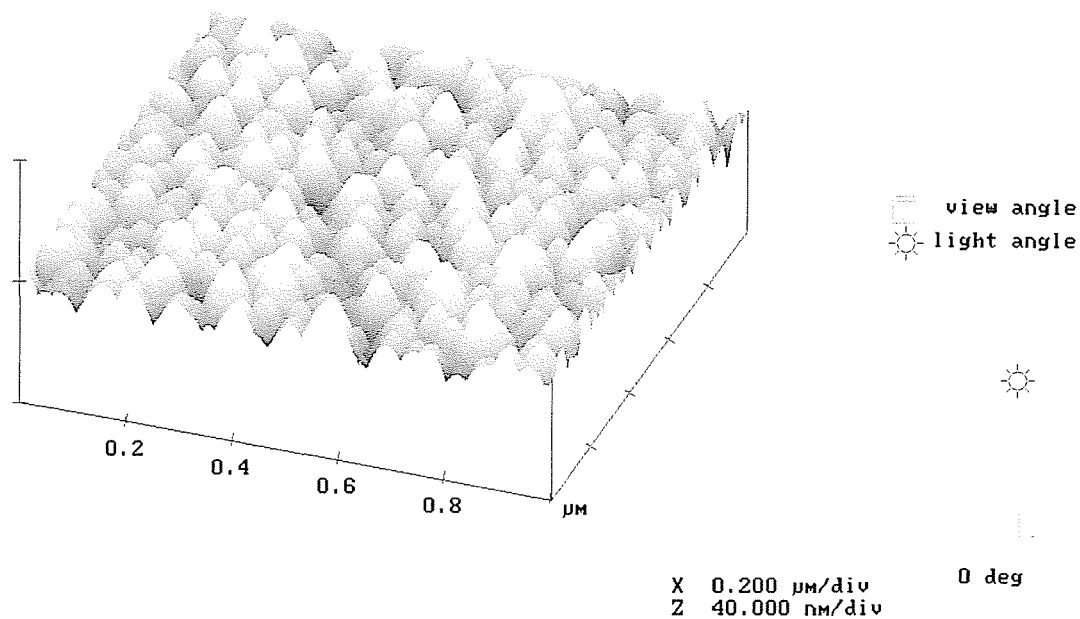


Figure 4.27. AFM image of the film shown in Figure 4.26 (c).

Figure 4.27 shows an AFM image of the film surface shown in Figure 4.26 (c). The imaged area is  $1\text{ }\mu\text{m} \times 1\text{ }\mu\text{m}$ . It is clearly shown that nanoparticles cover the entire surface of the film.

#### 4.4.3 Mechanism of Droplet Reduction by PAPLD

Reduction of droplets on a-C films was demonstrated by Ar and  $\text{O}_2$  PAPLD. A few models can be thought for this reduction: (1) droplets are decomposed due to the bombardment of energetic Ar ions; (2) droplets are etched completely by oxygen radicals generated in the oxygen plasma; and (3) droplets are charged negatively in the plasma and electrostatic force due to a strong electric field in the plasma-sheath region prevents them from depositing on substrates.



To consider speculation (1), the sputtering yield of solid carbon as a function of Ar ion incident energy is referred as shown in Figure 4.28 [62]. The sputtering yield at an Ar ion incident energy of ~400 eV is less than 0.15 atoms/ion. If it is assumed that the density of droplets is the same as that of graphite (2.267 g/cm<sup>3</sup>), number of carbon atoms in a 100-nm diameter droplet is estimated to be 6×10<sup>7</sup> atoms, which needs more than 3×10<sup>8</sup> of 400-eV Ar ions to be broken down.

The Ar ion flux in the region between pre-sheath and sheath is called as Bohm flux and described as the following formula [63]:

$$\Gamma_i = 0.605 n_0 \sqrt{\frac{\kappa T_e}{m_i}}$$

where  $\Gamma_i$  = Bohm flux [m<sup>-2</sup>s<sup>-1</sup>],  $n_0$  = plasma density [cm<sup>-3</sup>],  $\kappa$  = Boltzmann constant = 1.38×10<sup>-23</sup> [J/K],  $T_e$  = electron temperature [eV] and  $m_i$  = mass of Ar ion = 6.64×10<sup>-26</sup> kg.

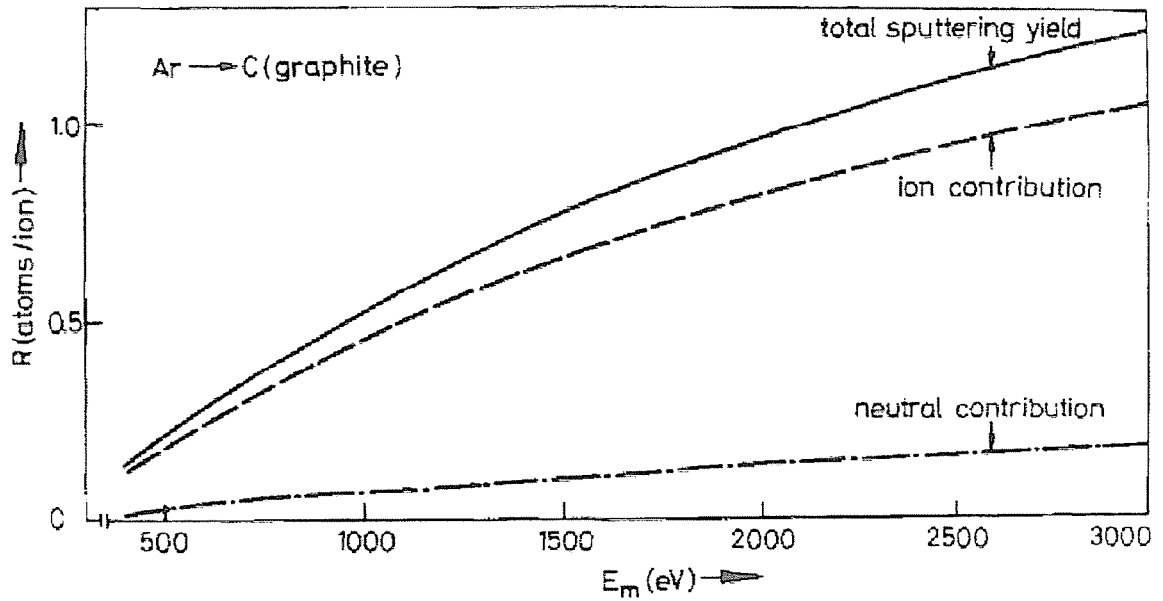


Figure 4.28. Sputtering yield as a function of Ar ion incident energy [62].

If it is assumed that  $n_0 = 1.0 \times 10^9 \text{ cm}^{-3}$  and  $T_e = 5 \text{ eV}$ ,  $I_i$  is calculated to be  $2.1 \times 10^{18} [\text{m}^{-2}\text{s}^{-1}]$ . Consequently,  $6.6 \times 10^4$  Ar ions, whose average kinetic energy must be less than 400 eV because  $T_e$  is 5 eV, irradiate on a surface area of 100 nm circle for 1 s. This may be impossible that the Ar ions break down the droplet in the present deposition time (~60 min).

Next, in order to examine speculation (2), the carbon film deposited in  $\text{O}_2$  gas [e.g., the film shown in Figure 4.26 (b)] was exposed to  $\text{O}_2$  plasma for 30 min (= the deposition time) using the same arrangement of RF coil, target and substrate as in the experiment for the result in Figure 4.26 (c). The ~100-nm-sized particles remained without any appreciable change in size. This result suggests that the smooth film surface was not treated directly with  $\text{O}_2$  plasma, but  $\text{O}_2$  plasma restrained the formation of ~100-nm-sized particles in the plume, and/or did not allow the particles to reach the substrate.

Finally, speculation (3) is examined. In general, particles in plasma acquire charges due to the collection of plasma electrons and ions. Because the electron mobility is much higher than ion one, particles mostly charge negatively. Charges on particle  $Q$  is described as follows:

$$\frac{dQ}{dt} = I_e + I_i$$

where  $I_e$  = electron current flowing into particles in plasma [mA],  $I_i$  = ion one [mA].

Then the charged droplets flowing from the target to substrate in the present

experiment are affected by the following two forces:

$$\text{Gravity force [N]: } \mathbf{F}_g = \frac{4}{3}\pi r^3 \rho g$$

$$\text{Coulomb force [N]: } \mathbf{F}_C = QE$$

where  $r$  = droplet radius [m],  $\rho$  = droplet density [kg/m<sup>3</sup>],  $g$  = acceleration of gravity = 9.806 [m/s<sup>2</sup>],  $E$  = electric field in sheath region [V/m]. These forces restrain negatively charged particles from reaching the substrate. The behavior of droplet in PAPLD is illustrated in Figure 4.29.

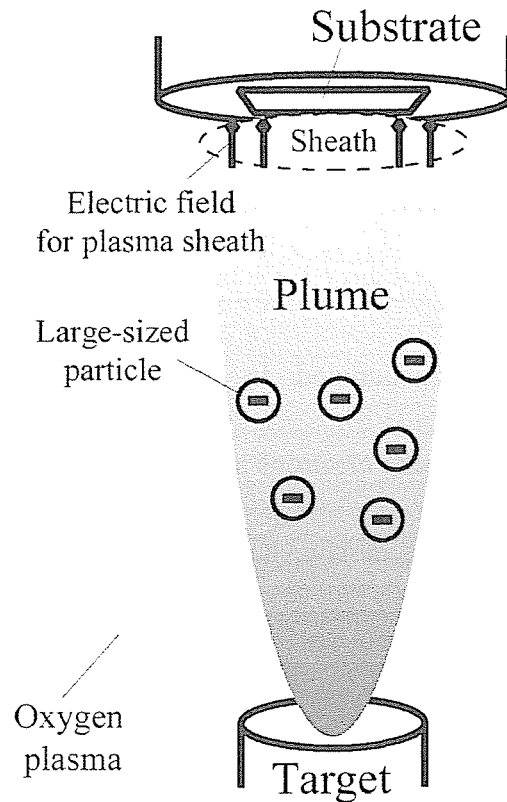


Figure 4.29. An illustration of behavior of negatively charged particles in PAPLD.



Homann, et al measured the charge on a plastic particle with a diameter of 9.4  $\mu\text{m}$  in plasma crystals to be  $Q \sim 8320 \pm 120e$  [64]. Kresten, et al showed that  $Q$  depends on the particle radius,  $Q \sim r^2$  [65]. Following these experimental and theoretical results, the charge  $Q$  on the droplet with a diameter of 10  $\mu\text{m}$  is assumed to be 80,000e and proportional to  $r^2$ . This charge is within a range of the other measurements [66, 67]. Under this assumption, the charge on a 100-nm-diameter droplet would be  $Q \sim 8e$ , and the droplets with a diameter  $\leq 30$  nm do not have any charge.

The velocity of droplets has been measured by a number of groups. For example, Lubben, et al estimated that the majority of Ge droplets, produced by a KrF excimer laser with a typical peak power density of  $5 \times 10^7$  W/cm<sup>2</sup>, had velocities between 25 and 120 m/s [68]. Geohegan determined a peak velocity of 45 – 120 m/s from the time-of-flight emission measurements for YBa<sub>2</sub>Cu<sub>3</sub>O<sub>7-x</sub> and BN systems irradiated by a KrF excimer laser at a fluence of 1.5 J/cm<sup>2</sup> [69]. Referring these experimental data, the droplet flight was calculated in the range of the initial velocity of 5 – 100 m/s, and the tidemark of droplet was obtained as shown in Table 4.2. The electric field strength in the sheath was assumed to be 1 kV/cm. The smaller droplet size and the slower initial velocity are, the lower tidemark becomes. It was shown that some droplets could not reach the substrate.

It was shown that, in PAPLD, the electric field has a strong effect on the droplet motion and reduction of droplets on substrates. Note that this effect is valid in both the Ar and O<sub>2</sub> plasmas. Speculation (3) is more appropriate than (1) and (2). However, in this

Table 4.2. Tidemarks of droplets of 100 nm – 10  $\mu$ m in diameter with an initial velocity = 5 – 100 m/s. The colored area represents that droplet stops prior to reaching the substrate.

Tidemark of droplet [mm]	Droplet initial velocity [m/s]										
	5	10	20	30	40	50	60	70	80	90	100
10000	10.99275	44.95467	181.8024	410.5485	731.1931	1143.736	1648.179	2244.52	2932.759	3712.897	4584.934
9000	9.853028	40.39741	163.5715	369.5302	658.2724	1029.797	1484.105	2021.196	2641.072	3343.73	4129.172
8000	8.713033	35.83176	145.3094	328.439	585.2185	915.6513	1319.736	1797.47	2348.858	2973.896	3672.585
7000	7.570183	31.25753	127.0145	287.2711	512.0348	801.2982	1155.069	1573.339	2056.116	2603.393	3215.177
6000	6.425374	26.67731	108.6853	246.0328	438.7168	686.7409	990.1041	1348.804	1762.844	2232.223	2756.939
5000	5.280423	22.08919	90.32428	204.7161	365.2674	571.9761	824.8415	1123.864	1469.042	1860.378	2297.872
4000	4.130324	17.49314	71.93197	163.33	291.6873	457.0038	659.2795	898.5144	1174.709	1487.862	1837.975
3000	2.985801	12.88914	53.50288	121.8677	217.9747	341.824	493.4166	672.7596	879.8448	1114.672	1377.244
2000	1.839377	8.277197	35.05335	80.33059	144.1324	226.4367	327.2641	446.5954	584.4485	740.8069	915.6856
1000	0.704803	3.682677	16.57205	38.7442	70.17377	110.8608	160.8149	220.0453	288.5332	366.2785	453.2974
900	0.600639	3.222685	14.73228	34.5866	62.76638	99.29515	144.1665	197.3633	258.9113	328.7997	407.0136
800	0.488311	2.762596	12.89211	30.42362	55.36612	87.73398	127.4921	174.6937	229.2882	291.3027	360.7336
700	0.383408	2.302408	11.05156	26.25334	47.97502	76.15325	110.8475	152.0021	199.6689	253.8	314.4392
600	0.280708	1.853096	9.210614	22.10547	40.57272	64.59926	94.17624	129.3344	170.0212	216.311	268.1273
500	0.176348	1.410783	7.369276	17.96261	33.16174	53.03722	77.52679	106.6346	140.4146	178.8004	221.8252
400	0.095472	0.977358	5.527545	13.81886	25.79521	41.45659	60.87092	83.98111	110.7763	141.291	175.535
300	0	0.561807	3.707908	9.674234	18.42711	29.94406	44.22507	61.28134	81.16913	103.821	129.2369
200	0	0.19109	1.955451	5.56272	11.05744	18.42907	27.64361	38.70105	51.60141	66.34466	82.93083
100	0	0	0.382328	1.686207	3.911638	7.058621	11.12716	16.12716	22.11724	29.02888	36.86207

model, as droplet diameter increases, the deceleration is reduced. This may be a reason why PAPLD could not completely avoid deposition of droplets on substrate and a lot of nanoparticles, which would have a much higher velocity than the droplets, deposited on substrates as described in section 4.2.

## 4.5 XPS Analysis of a-C Nanoparticles and Films

### 4.5.1. XPS Analysis

C (1s) XPS spectra of the a-C films deposited in Ar gas and plasma at  $p_{\text{Ar}} = 0 - 100$  mTorr are shown in Figure 4.30. The broken lines respectively indicate the peak binding energy (BE) of crystalline graphite (100%  $\text{sp}^2$ , 284.1 eV) and poly-crystalline diamond (100%  $\text{sp}^3$ , 285.5 eV), which are measured with our XPS instrument. The BEs of the films in both the Ar gas and plasma at  $p_{\text{Ar}} = 1$  mTorr are the closest to the BE of diamond ( $\text{sp}^3$ ), and shift gradually toward the BE of graphite ( $\text{sp}^2$ ) as  $p_{\text{Ar}}$  increases. The C (1s) spectra shown here, except the case of the 1-mTorr Ar gas and vacuum, may represent the bonding

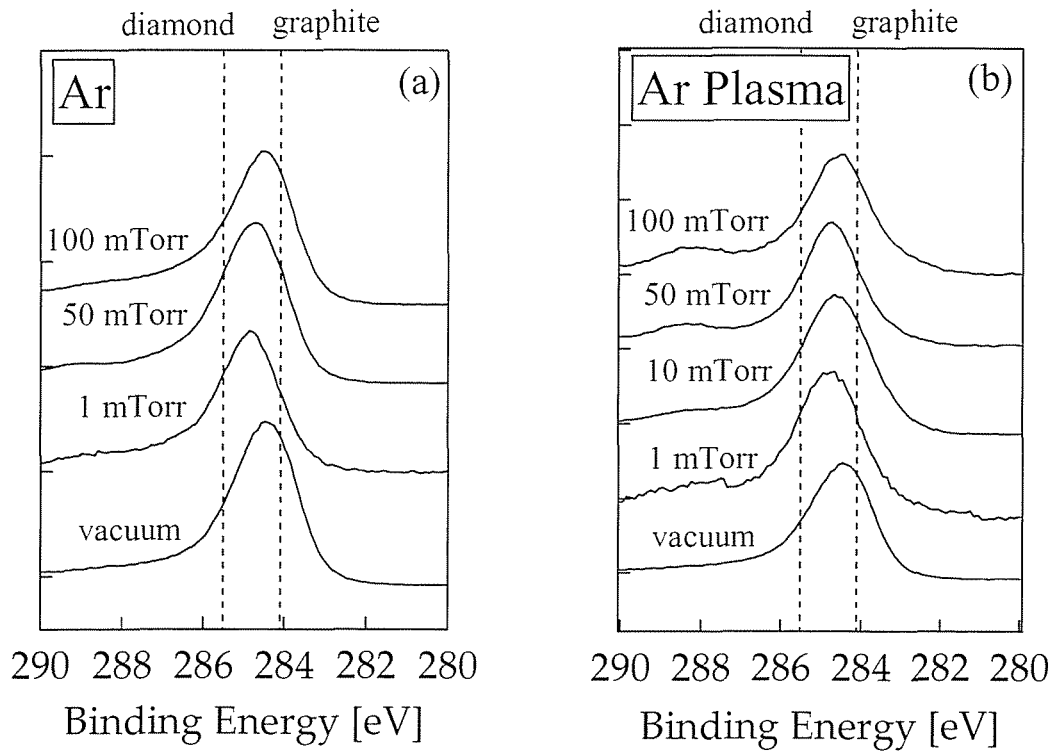


Figure 4.30. C (1s) XPS spectra of a-C films deposited in (a) Ar gas and (b) Ar plasma.

property of a-C nanoparticles because the entire film surface is covered with nanoparticles. In the cases of the vacuum and 1-mTorr Ar gas, the spectra show the average property of the nanoparticles and films.

As Merel, et al [70] and Diaz, et al [71] performed using a Gaussian curve fitting method, the C (1s) spectra were deconvoluted into  $sp^3$ ,  $sp^2$  and carbon oxide components. The aforementioned BEs of  $sp^2$  and  $sp^3$  were used, and full-width at half-maximum (FWHM) of the spectra was properly adjusted. Background component in the spectra was removed according to Shirley's method [72]. An example of the deconvolution is shown in Figure 4.31. The  $sp^3$  and  $sp^2$  contents are respectively obtained by an integration of each component.

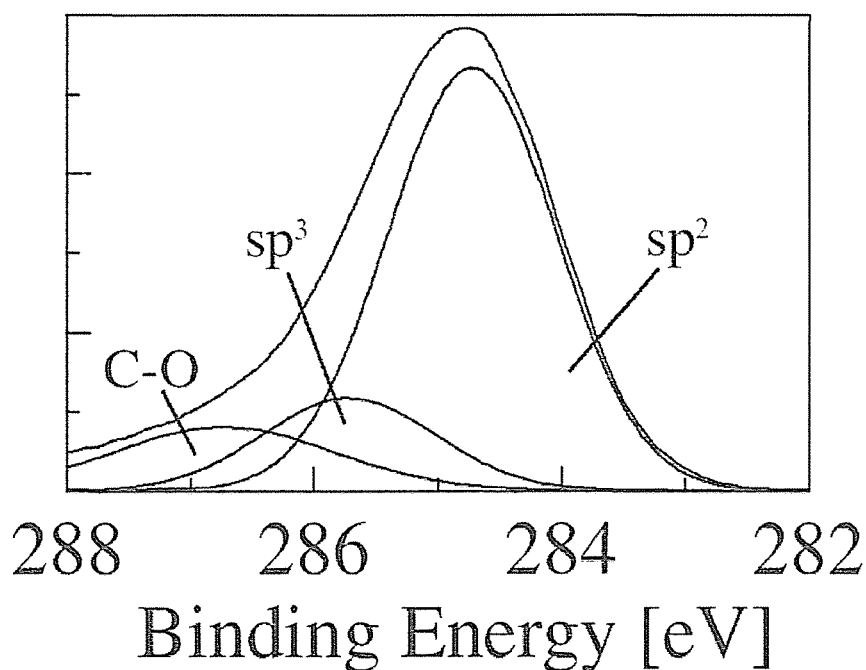
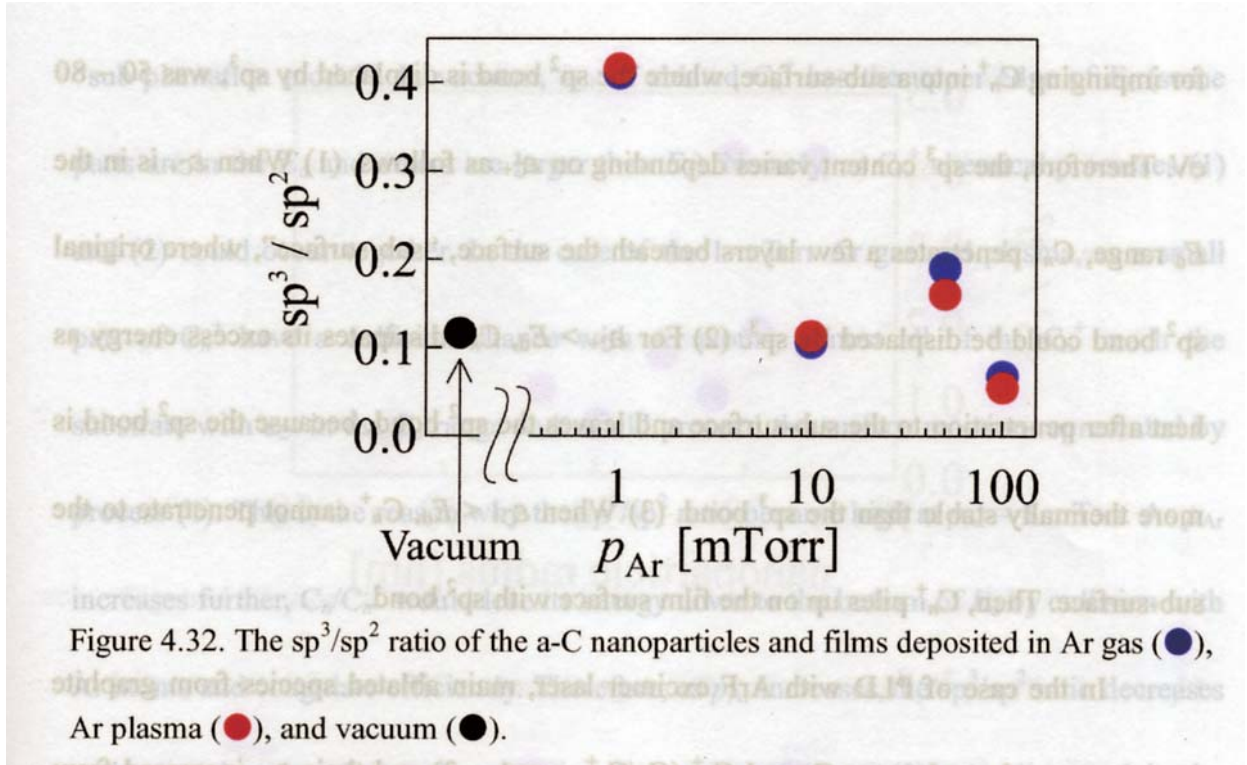


Figure 4.31. An example of the deconvolution of C (1s) spectra by  $sp^2$ ,  $sp^3$  and carbon oxide components.



As shown in Figure 4.32, the ratio of  $sp^3$  content to  $sp^2$  one ( $sp^3/sp^2$  ratio) became the largest  $\sim 0.4$  at  $p_{Ar} = 1$  mTorr and decreased with  $p_{Ar}$ . Any difference in the ratio between the Ar gas and plasma was hardly seen.

#### 4.5.2 Model for Deposition of a-C Nanoparticles and Films by PAPLD

In order to understand the dependence of the  $sp^3/sp^2$  ratio on  $p_{Ar}$ , the following surface chemistry model [73-76] and related data on kinetic energy ( $\varepsilon_{C^+}$ ) of ablated particles ( $C_n^+$  and  $C_n$  ( $n = 1 - 3$ )), which has been reported so far [12-15, 76], is explained.

Merkulov, et al reported that the  $sp^3$  content in a-C films depends on the kinetic energy  $\varepsilon_{C^+}$  of  $C_n^+$  impinging to the substrate [73]. This mechanism could be explained using the following “sub-plantation model” [74-76]. In this model, the energy range,  $E_d$

for impinging  $C_n^+$  into a sub-surface, where the  $sp^2$  bond is displaced by  $sp^3$ , was 50 – 80 eV. Therefore, the  $sp^3$  content varies depending on  $\varepsilon_{C^+}$  as follows. (1) When  $\varepsilon_{C^+}$  is in the  $E_d$  range,  $C_n^+$  penetrates a few layers beneath the surface, “sub-surface”, where original  $sp^2$  bond could be displaced by  $sp^3$ . (2) For  $\varepsilon_{C^+} > E_d$ ,  $C_n^+$  dissipates its excess energy as heat after penetration to the sub-surface and leaves the  $sp^2$  bond, because the  $sp^2$  bond is more thermally stable than the  $sp^3$  bond. (3) When  $\varepsilon_{C^+} < E_d$ ,  $C_n^+$  cannot penetrate to the sub-surface. Then,  $C_n^+$  piles up on the film surface with  $sp^2$  bond.

In the case of PLD with ArF excimer laser, main ablated species from graphite target were carbon clusters,  $C_n$  and  $C_n^+$  ( $C_n/C_n^+$ ,  $n = 1 - 3$ ) and their  $\varepsilon_{C^+}$  increased from 45 eV to 95 eV, as the laser fluence increased from  $2 \times 10^7$  to  $3 \times 10^8$  W/cm<sup>2</sup> [12-15, 45]. According to this result, the present ablated species are  $C_n/C_n^+$  ( $n = 1 - 3$ ) and have  $\varepsilon_{C^+}$  around  $\sim 70$  eV, because the present ArF laser fluence is  $\sim 1.05 \times 10^8$  W/cm<sup>2</sup>. However,  $\varepsilon_{C^+}$  may have wide distribution, e.g. depending on  $n$  (the mass of C clusters). In vacuum,  $C_n/C_n^+$  may reach the substrate without any energy loss, however for  $p_{Ar} \geq 100$  mTorr,  $C_n/C_n^+$  cool down appreciably due to collision with Ar atoms in the plume, because the collision mean free path for  $C_n/C_n^+$  at  $p_{Ar} = 10$  mTorr is estimated to be the same order as the target-substrate distance,  $d_{st}$  ( $= 20$  mm). In this sense, ablated  $C_n/C_n^+$  could grow up by coagulation each other in the plume for  $p_{Ar} \geq 10$  mTorr.

Figure 4.32 shows that the  $sp^3/sp^2$  ratio is  $\sim 0.4$  at  $p_{Ar} = 1$  mTorr and decreases for  $p_{Ar} > 1$  mTorr. I try to explain the tendency in Figure 4.32, taking aforementioned

“sub-plantation model”. In vacuum,  $\varepsilon_{C^+}$  of ablated  $C_n^+$  has the upper edge of  $E_d$  (some parts are in the  $E_d$  and others are larger than  $E_d$ ). Namely, as  $C_n^+$  chemical processes (1) and (2) could occur together. In the case of the 1-mTorr Ar gas and plasma, as a small part of  $C_n^+$  have a collision chance with Ar atoms, almost all of the  $C_n^+$  reach the substrate with  $\varepsilon_{C^+}$  in the  $E_d$  range and would proceed the surface reaction represented by process (1). This is the reason why the  $sp^3/sp^2$  ratio became high at  $p_{Ar} = 1$  mTorr. As  $p_{Ar}$  increases further,  $C_n/C_n^+$  would lose its energy down to the bottom of  $E_d$  by collision with Ar atoms and coagulate efficiently. Therefore, as  $p_{Ar}$  increases, the  $sp^3/sp^2$  ratio decreases with  $p_{Ar}$  (changing the surface reaction from process (1) to (3)). As discussed in the above, a “sub-plantation model” could explain the growth process of a-C nanoparticles.

#### 4.5.3. Correlation between the AFM and XPS Results

In order to examine the correlation between the AFM and XPS analyses, the results of Figures 4.20 and 4.32 were combined. The  $sp^3/sp^2$  ratio was plotted as a function of the particle radius,  $r$  as shown in Figure 4.33. It is noticed that the  $sp^3/sp^2$  ratio decreases monotonously with an increase of  $r$ , and that the ratio obtained in the Ar plasma is larger than that in the Ar gas. As the collision frequency increases between  $C_n/C_n^+$  and Ar atoms as  $p_{Ar}$  increases,  $\varepsilon_{C^+}$  of  $C_n/C_n^+$  decreases. Consequently, aggregation of nanoparticles with lower  $\varepsilon_{C^+}$  would occur more frequently. Therefore, larger nanoparticles contain higher  $sp^2$  content comparing with smaller ones, as discussed in a

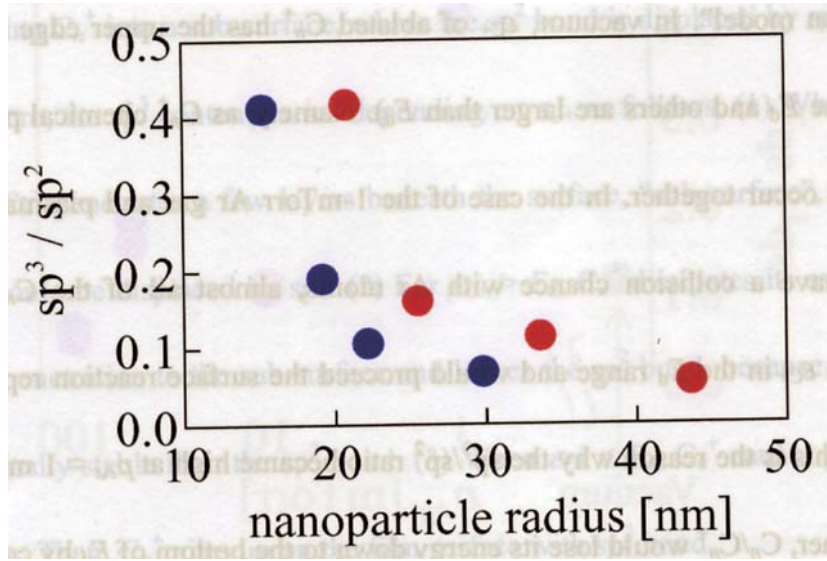


Figure 4.33. The  $sp^3/sp^2$  ratio of the a-C nanoparticles as a function of the nanoparticle radius: obtained in the Ar gas (●) and Ar plasma (●).

“sub-plantation model”. The  $\varepsilon_{C^+}$  of  $C_n^+$  in the plasma may be larger than that in the Ar gas because the electric field in the sheath region accelerates positively charged particles toward the substrate unlike the case of negatively charged droplets as explained in Section 4.4.3.

## 4.6 Deposition of a-C Films by O<sub>2</sub> PAPLD

### 4.6.1 AFM Analysis of a-C Films

SEM micrographs of the a-C films deposited in (a) vacuum, (b) O<sub>2</sub> gas and (c) O<sub>2</sub> plasma are shown in Section 4.4 (Figure 4.26). The difference in surface morphology and chemical composition is discussed in this section.



PLD in gas phase is well known as a fabrication technique of nanoparticles [1, 23]. Here, it is thought that ablated atoms and molecules cool down due to collisions with ambient gas atoms and/or molecules and condense into nanoparticles. In  $O_2$  gas, carbon nanoparticles with a diameter of  $\sim 100$  nm were formed as shown in Figure 4.26 (b). On the other hand, on the film deposited in  $O_2$  plasma, no  $\sim 100$ -nm-diameter particles are seen, even at the same  $p_{O_2}$  as in the case of  $O_2$  gas [see Figure 4.26 (c)].

Figure 4.34 show AFM images of the films shown in Figure 4.26. The film deposited

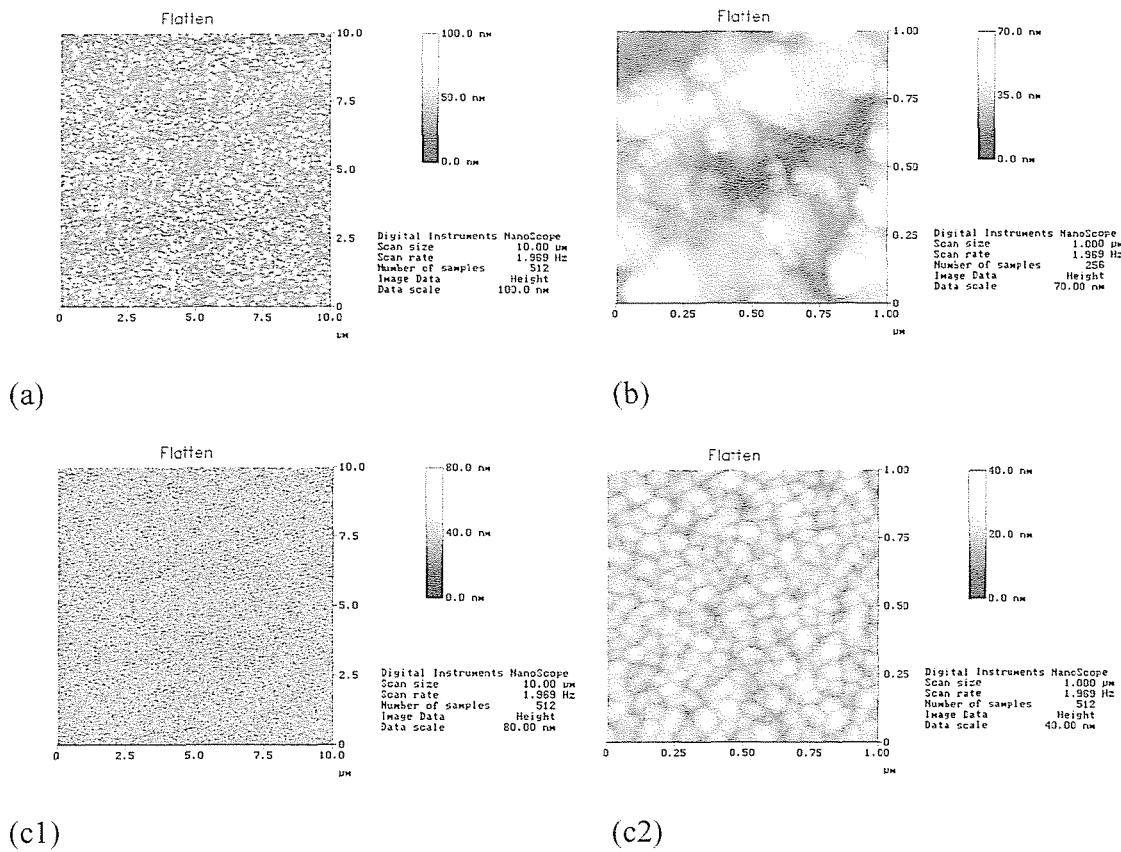


Figure 4.34. AFM images of the a-C films deposited in (a) vacuum, (b)  $O_2$  gas, and (c)  $O_2$  plasma at  $T_{sub} \sim 400^\circ C$ . The  $O_2$  gas pressure,  $p_{O_2}$  was 0.4 mTorr.

in vacuum at  $T_{\text{sub}} \sim 410^\circ\text{C}$  contains a lot of nanoparticles and is different from that deposited at room temperature (see e.g. Figure 4.8 (a)). This result is similar to that by Yoshitake et al [15]. These convex structures were not formed by deposition of nanoparticles grown in the plume, but are composed of migrated carbon clusters which impinged into the film subsurface since this surface was obtained at  $\sim 410^\circ\text{C}$  [15, 77]. AFM analysis of the film deposited in  $\text{O}_2$  gas showed it contains a lot of particles with a wide range of diameter from  $\sim 10$  to  $\sim 100$  nm. This ensures the SEM analysis as shown in Figure 4.26 (b). On the other hand, the film deposited in  $\text{O}_2$  plasma, was found to contain a lot of nanoparticles by the AFM analysis, which were not seen by the SEM.

#### 4.6.2 Raman Spectroscopy of a-C Films

Figure 4.35 shows Raman spectra of the films deposited in (a) vacuum, (b)  $\text{O}_2$  gas and (c)  $\text{O}_2$  plasma of 0.4 mTorr at  $T_{\text{sub}}$  between  $25^\circ\text{C}$  and  $480^\circ\text{C}$ . The Raman spectra of disordered graphite show two quite sharp modes, the  $G$  peak around  $1580 - 1600 \text{ cm}^{-1}$  and the  $D$  peak around  $1350 \text{ cm}^{-1}$ , usually assigned to zone center phonons of  $E_{2g}$  symmetry and  $K$ -point phonons of  $A_{1g}$  symmetry, respectively [78-81]. While all of the spectra obtained at  $T_{\text{sub}} = 25^\circ\text{C}$  show a similar feature, difference in the spectra appears as  $T_{\text{sub}}$  increases. The spectra in Figures 4.35 (a) and (b) above  $T_{\text{sub}} \sim 350^\circ\text{C}$  clearly show the two peaks at  $\sim 1590 \text{ cm}^{-1}$  (indicating crystalline graphite,  $G$ ) and  $\sim 1350 \text{ cm}^{-1}$  (indicating disordered nanometer-size graphite,  $D$ ). This structure represents a typical

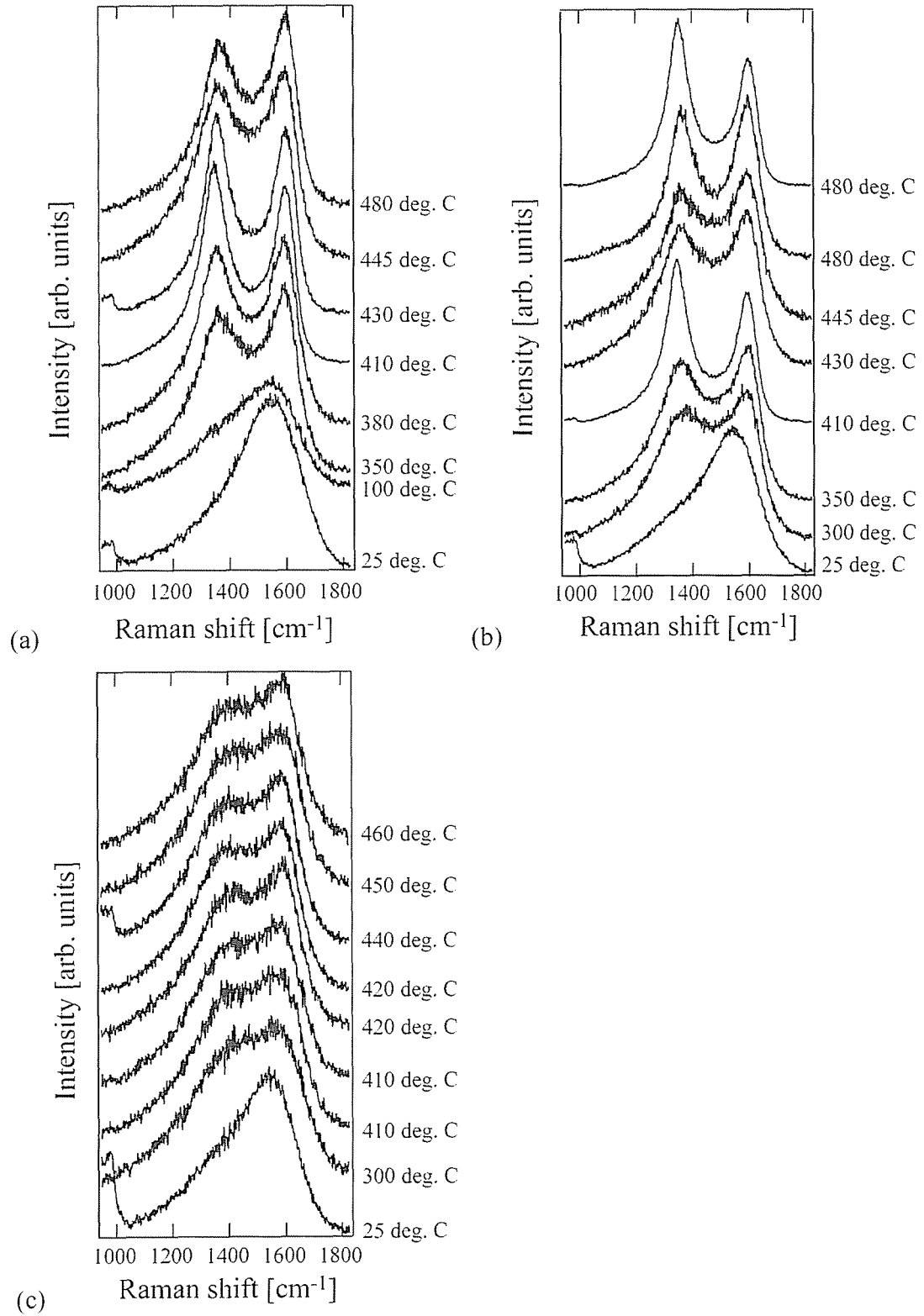


Figure 4.35. Raman spectra of the a-C films deposited in (a) vacuum, (b)  $O_2$  gas and (c)  $O_2$  plasma at  $T_{\text{sub}}$  between  $25^\circ\text{C}$  and  $480^\circ\text{C}$ .

property of glassy carbon [82]. The appearance of D peak indicates disordered graphite. When number of defects in the crystalline graphite increases and the size is reduced below 2 nm, the intensity of D peak starts to decrease [7]. Hence, the Raman spectra of a-C show one broad peak, and consequently, all of the spectra in Figure 4.35 (c) correspond to that of a-C films. These results appear to be consistent with those obtained from the XPS analysis described later.

#### 4.6.3 XPS analysis of a-C films

Figure 4.36 shows C (1s) XPS spectra of the films obtained in (a) vacuum, (b) O<sub>2</sub> gas and (c) O<sub>2</sub> plasma at  $T_{\text{sub}}$  between 25°C and 480°C. The resolution of XPS spectra is 0.1 eV. Broken lines at 284.1 eV and 285.5 eV correspond to the peak binding energies (BEs) of crystalline graphite and poly-crystalline diamond, respectively. As  $T_{\text{sub}}$  increases, the BEs of the films deposited in the each ambient changes as follows: (1) in vacuum, the BE approaches the BE of graphite; (2) in O<sub>2</sub> gas, the BE approaches similarly to the case of (1); and (3) in O<sub>2</sub> plasma, the BE firstly approaches the BE of graphite at  $T_{\text{sub}}$  between 25°C and ~300°C, then goes back to the BE of diamond at  $T_{\text{sub}}$  between ~300°C and ~430°C, and finally approaches the BE of graphite above  $T_{\text{sub}} = \sim 430^\circ\text{C}$ . The BE of the film deposited in O<sub>2</sub> plasma at  $T_{\text{sub}} \sim 410^\circ\text{C}$  is closest to that of diamond.

The  $\text{sp}^3/\text{sp}^2$  ratio of the a-C films was evaluated as it was performed in Section 4.5.1. In this analysis, the C (1s) spectra were decomposed into “diamond (100%  $\text{sp}^3$

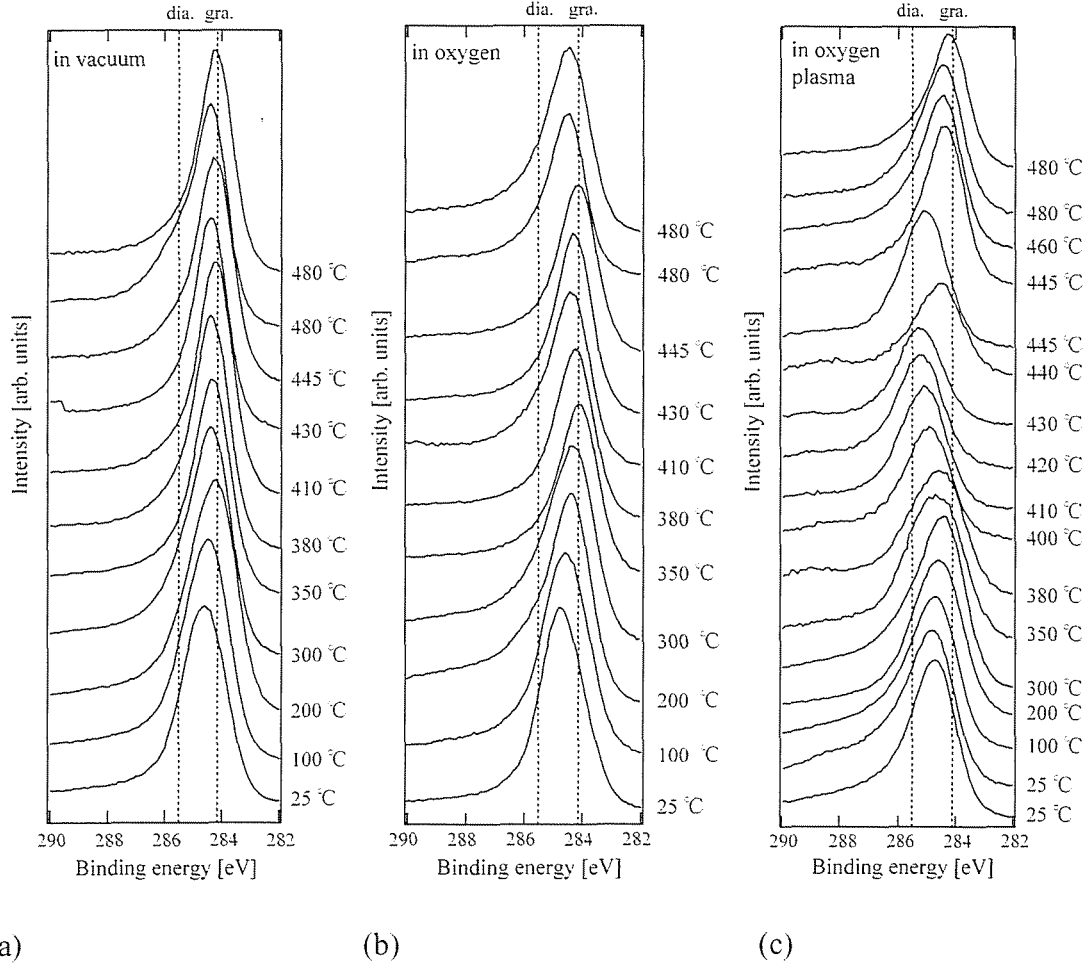


Figure 4.36. C (1s) XPS spectra of the a-C films deposited in (a) vacuum, (b) O<sub>2</sub> gas and (c) O<sub>2</sub> plasma.

carbon)”, “graphite (100% sp<sup>2</sup> carbon)” and “unidentified” components using their BEs and full-widths at half maxima (FWHMs = 1.1 eV for graphite and diamond). The BE and FWHM of “unidentified” were adjusted to fit the spectra. Figure 4.37 shows the (a) sp<sup>3</sup> and (b) sp<sup>2</sup> contents of the films as a function of  $T_{\text{sub}}$ . Opposite variation on  $T_{\text{sub}}$  was seen between the sp<sup>3</sup> and sp<sup>2</sup> contents, then the result of sp<sup>3</sup> content is described here. In vacuum and in O<sub>2</sub> gas, the sp<sup>3</sup> content decreases gradually with  $T_{\text{sub}}$  and no appreciable

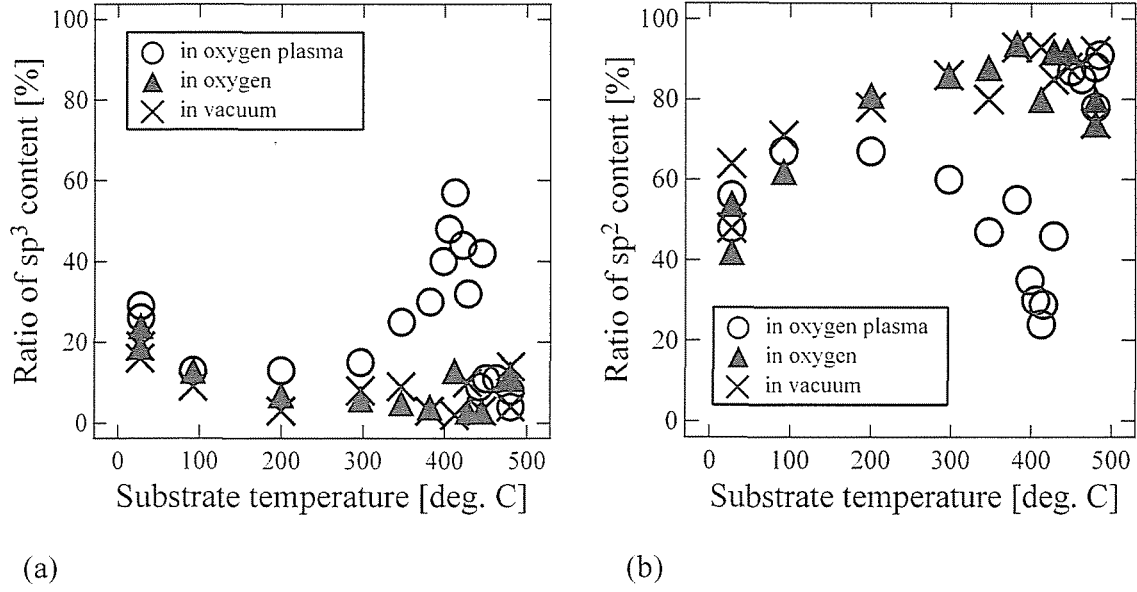


Figure 4.37. (a)  $sp^3$  and (b)  $sp^2$  contents as a function of  $T_{sub}$ .

differences are seen. While, in the  $O_2$  plasma, though the  $sp^3$  content decreases with  $T_{sub}$  below  $100^\circ C$ , it increases with  $T_{sub} > 100^\circ C$  and reaches a maximum value of 58% at  $T_{sub} = 410^\circ C$ . For  $T_{sub} > 410^\circ C$ , the  $sp^3$  content rapidly drops with  $T_{sub}$  and the  $sp^3$  content becomes only a 2 – 3% in any ambient  $T_{sub} > 450^\circ C$ .

It is difficult to explain why the distinct peak of the  $sp^3$  content appears at  $T_{sub} = 410^\circ C$  in  $O_2$  PAPLD. However, the following previously reported results will help us to understand this peak. (1) In the microwave plasma-enhanced CVD experiment, the number of  $sp^3$  bond decreases with increasing  $T_{sub}$ , and addition of  $O_2$  gas significantly influences the growth of diamond films below  $500^\circ C$ , through the etching of nondiamond carbon compounds with O atoms and active species [18, 19]. Another example is the oxidization effect observed at around  $500 - 600^\circ C$  [20]. (2) Deposition of

a-C from appropriate energy ion beams ( $\sim 100$  eV) promotes  $sp^3$  bonding [76], (3) The deposition rate of the films in  $O_2$  PAPLD at  $T_{\text{sub}} \sim 400^\circ\text{C}$  ( $\sim 0.7$  nm/min) was lower than that in other ambients ( $\sim 1.5$  nm/min for in vacuum and  $\sim 1.3$  nm/min for in  $O_2$  gas) at the same  $T_{\text{sub}} \sim 400^\circ\text{C}$ . This may indicate selective etching of nondiamond carbon compounds [18, 19].

Based on the results presented above, we conclude that appropriate energy impinging onto the substrate for  $C_n^+$  due to sheath formation was obtained in  $O_2$  PAPLD at  $410^\circ\text{C}$ . More efficient etching of nondiamond components would shift the favorable  $T_{\text{sub}}$  for  $O_2$  addition in PLD and CVD [18, 20]. The growth mechanism of a-C by  $O_2$  PAPLD is discussed in detail in next section.

#### 4.6.4. Mechanism of a-C Film Deposition by $O_2$ PAPLD

The  $sp^3$  and  $sp^2$  contents of the a-C films deposited in vacuum,  $O_2$  gas and  $O_2$  plasma were evaluated by XPS and are shown in Figure 4.37. As  $T_{\text{sub}}$  increased, the  $sp^3$  content obtained in vacuum and  $O_2$  gas decreased, but the  $sp^2$  content increased. The  $sp^3$  content became less than 10% above  $T_{\text{sub}} = 200^\circ\text{C}$ . Introduction of  $O_2$  gas did not show any change in the  $sp^3$  content. These results are explained by a “sub-plantation model” [74-76, 83, 84]. Generally in PLD, ablated clusters become reduced in size as the wavelength of ablation laser shortens [14, 83, 85]. When ArF excimer laser ( $\lambda = 193$  nm) is used, ablated carbon clusters are dominantly small, such as  $C_{1-3}^+$  [12-15, 76] and

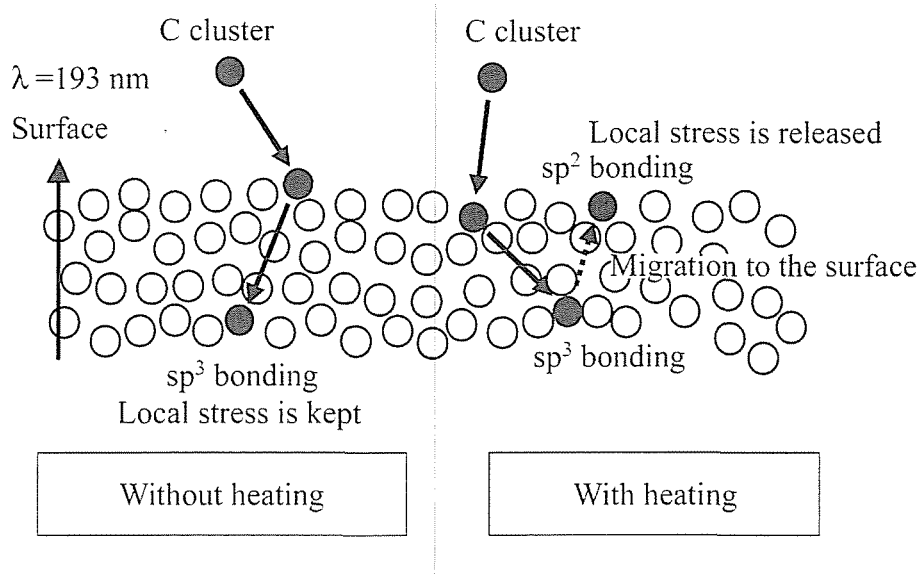


Figure 4.38. Formation process of  $sp^3$  and  $sp^2$  bonds in a-C films explained by sub-plantation model [15].

enough energetic to achieve crystal growth of thin film [15]. When these small clusters are impinged onto substrate surface, they could reach sub-surface and generate internal stress, and then  $sp^3$  bond is formed as illustrated in Figure 4.38. However, when substrate is heated, the cluster in sub-surface tends to migrate the substrate surface and releases its internal surface, and then  $sp^2$  bond, which is thermally more stable than  $sp^3$  one, is formed.

Unlike the results in vacuum and  $O_2$  gas, the  $sp^3$  content of the films deposited in  $O_2$  plasma increased with  $T_{sub}$  between  $\sim 200$  and  $\sim 430^\circ C$ , reached a maximum (58%) at  $T_{sub} \sim 410^\circ C$ , and then decrease  $T_{sub} \geq \sim 430^\circ C$ . It is thought that oxygen radicals, which are generated in  $O_2$  plasma and etch  $sp^2$  selectively, obtain a high energy from substrate



as  $T_{\text{sub}}$  increased. To explain the effect of  $T_{\text{sub}}$  in  $\text{O}_2$  PAPLD, the following processes are considered: (1) graphitization of a-C, (2) enhancement of the migration of oxygen radicals on the film surface and (3) enhancement of  $\text{sp}^2$  etching by the radicals. In the present experiment, these effects would result in a high  $\text{sp}^3$  content at  $T_{\text{sub}} \sim 410^\circ\text{C}$ .

It is reported that the  $\text{sp}^3$  content of a-C films depends on laser fluence as shown in Figure 4.39 [86]. The laser fluence in this study is  $\sim 2.1 \text{ J/cm}^2$  ( $\sim 1 \times 10^8 \text{ W/cm}^2$ ) or less at which the  $\text{sp}^3$  content is  $\sim 30\%$  and not a maximum [86]. The laser fluence of  $2.1 \text{ J/cm}^2$  would not be an optimal value. Due to the limitation of the experimental setup in this study, the fluence could not be raised above  $2.1 \text{ J/cm}^2$ . However, the effect of  $\text{O}_2$  plasma on increase of  $\text{sp}^3$  content in a-C films was confirmed by comparing to the results in  $\text{O}_2$

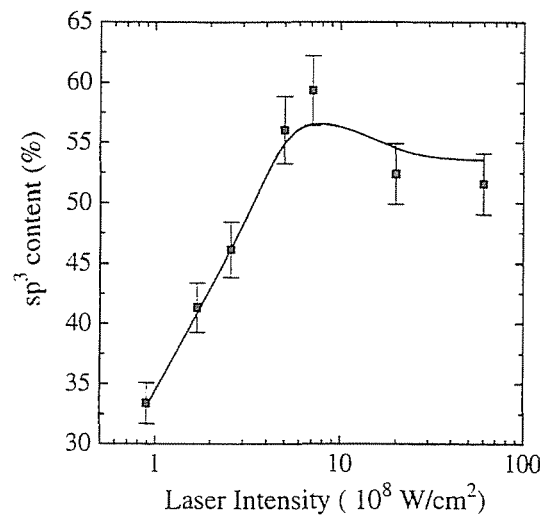


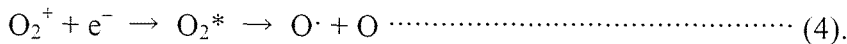
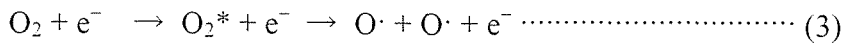
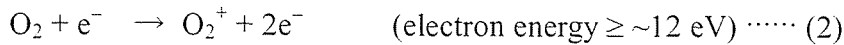
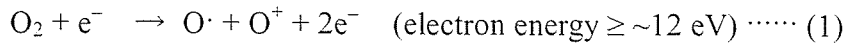
Fig. 2. Variation of the  $\text{sp}^3$  carbon atoms content of the DLC coatings, deposited at  $25^\circ\text{C}$ , as a function of laser intensity.

Figure 4.39. Variation of the  $\text{sp}^3$  content of the a-C films deposited at  $25^\circ\text{C}$ , as a function of laser fluence [86].

gas and in vacuum.

The oxygen content in the a-C films was evaluated by XPS analysis, in which the areas of C (1s) and O (1s) spectra were calculated taking into account the relative sensitivity factors. As a result, the oxygen contents of the films deposited in vacuum, in O<sub>2</sub> gas and in O<sub>2</sub> plasma are ~6%, ~10% and 20%, respectively. These values did not change on  $T_{\text{sub}}$ . In C (1s) XPS spectra, the BE of C-O bond is located between 287 and 289 eV [16]. This peak is ~2.5 eV higher than that of diamond (285.5 eV), and therefore does not affect on the deconvolution of C (1s) spectra by sp<sup>2</sup> and sp<sup>3</sup> significantly. Though the film deposited in O<sub>2</sub> plasma contained oxygen at ~20%, no strong C-O peak was seen as shown in Figure 4.36 (c).

Figure 4.40 shows the optical emission spectra at the graphite target surface in O<sub>2</sub> plasma (a) without and (b) with laser ablation. Emission peaks of atomic oxygen and O<sub>2</sub><sup>+</sup> were observed in Figure 4.40 (a). These species are formed in plasma through the following electron impact dissociation (1), electron impact ionization (2) and secondary processes (3 and 4) [87]:



The production rate of O<sub>2</sub><sup>+</sup> could be higher than that of O<sup>+</sup> because O<sup>+</sup> did not appear in

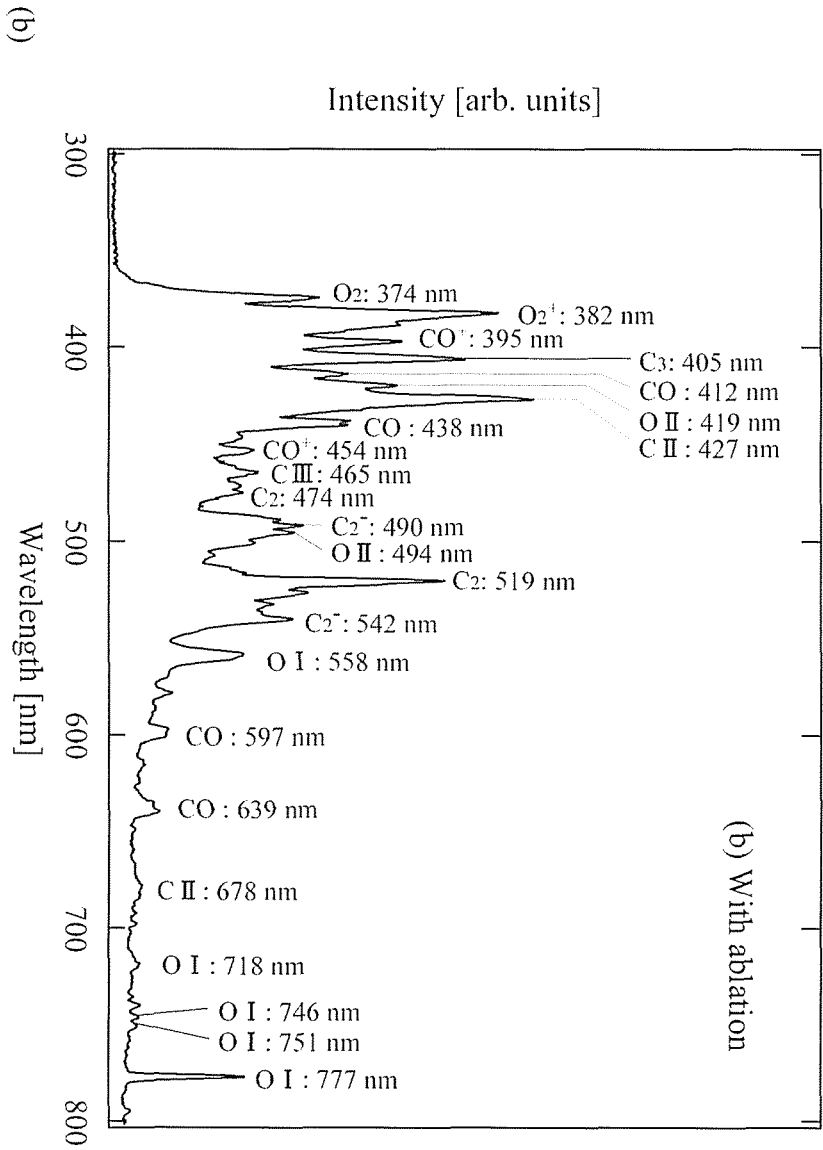
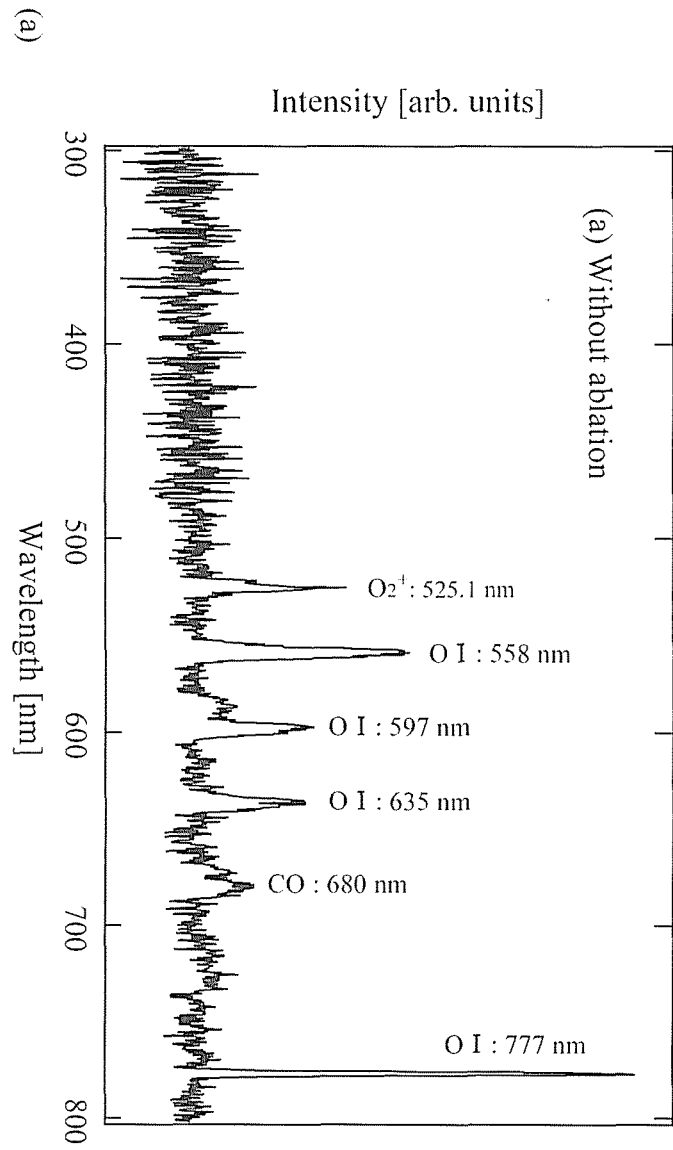


Figure 4.40. Optical emission spectra at the graphite target surface in  $O_2$  plasma: (a) without and (b) with laser ablation.

the emission spectra. The emission of CO comes from the etching of graphite by oxygen radicals. With laser ablation, the emission peaks,  $C_2$ ,  $C_2^-$ ,  $C_3$ ,  $C^+$ ,  $C^{2+}$ , atomic oxygen, CO,  $O_2^+$ ,  $O^+$  and  $CO^+$  were observed as shown in Figure 4.40 (b).

It is thought that these CO and  $CO^+$  peaks are attributed to etching of  $sp^2$  by oxygen radicals. The deposition rate of a-C films obtained in (a) vacuum, (b)  $O_2$  gas and (c)  $O_2$  plasma as a function of  $T_{sub}$  is shown in Figure 4.41. An average of the rates over  $T_{sub}$  range are respectively  $\sim 1.6$  nm/min for vacuum, 1.2 nm/min for  $O_2$  gas and 1.0 nm/min for  $O_2$  plasma. It is speculated that, by introducing  $O_2$  gas, ablated carbon clusters were diffused due to collisions with  $O_2$  gas molecules, and therefore the deposition rate decreased as compared to the case in vacuum. Further decrease in the deposition rate by  $O_2$  PAPLD due to the effect of  $sp^2$  etching by oxygen radicals.

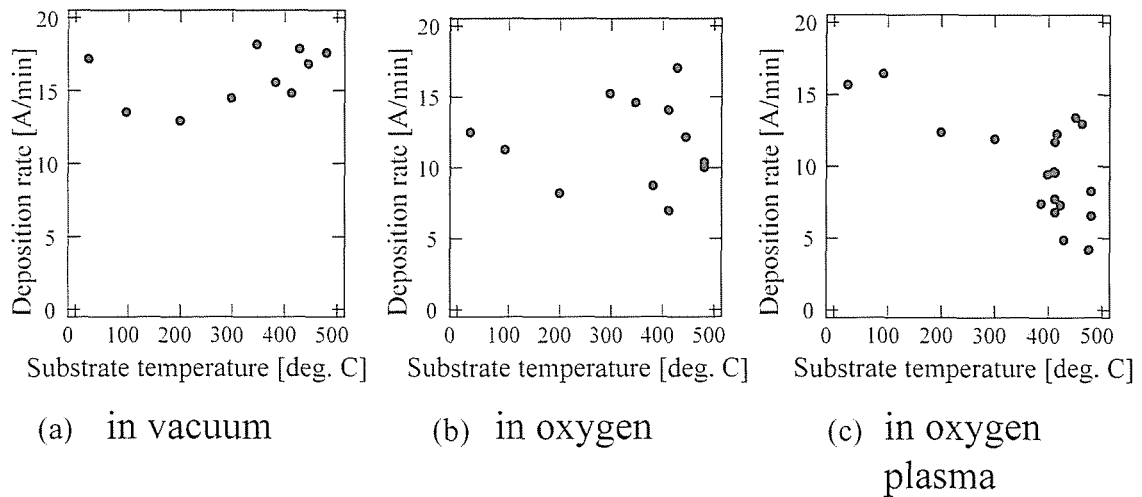


Figure 4.41. Deposition rate of a-C films obtained in (a) vacuum, (b)  $O_2$  gas and (c)  $O_2$  plasma as a function of  $T_{sub}$ .

## Chapter 5

### Syntheses of Carbon Nanotubes (CNTs) and Nanofibers (CNFs) by PLD

In this chapter, growth of carbon nanotubes (CNTs) and nanofibers (CNFs) by PLD using ArF excimer laser ( $\lambda = 193$  nm) is presented. Most laser ablation experiments for CNT growth have been performed using an Nd: YAG laser ( $\lambda = 532$  or  $1064$  nm) except the recent report by KrF excimer laser ( $\lambda = 248$  nm) [88]. The dependence of CNT growth on the laser wavelength has not been studied adequately. As the ArF laser generates more energetic and smaller carbon cluster,  $C_n^+$  ( $n = 1 - 3$ ) than that obtained by visible and infrared laser [12], CNT growth process would be different from the case that the longer wavelength laser is used. Smaller  $C_n^+$  ( $n = 1 - 3$ ) ablated cluster would tell us CNT growth mechanism.

#### 5.1 Growth of CNTs in a laser oven apparatus

##### 5.1.1 Observation of CNTs by SEM and TEM

The experimental setup and procedure are described in Chapter 2. After LA of a graphite target containing 1 at. % Ni and minute amount of Y (Ni/Y/C target) with a repetition rate of 10 Hz for 60 minutes at  $T = 1100^\circ\text{C}$ , carbon soot mostly deposited in area (3) where the CNT content in the raw soot was  $\sim 60\%$ . The carbon soot was analyzed

Table 5.1. The experimental condition for CNT growth.

Base pressure	$1 \times 10^{-3}$ Torr
Ablation laser	ArF excimer laser ( $\lambda = 193$ nm, pulse duration=20 ns)
Laser fluence	2, 3 J/cm <sup>2</sup>
Repetition rate	10, 50 Hz
Target	Ni (1 at. %)/Y/C, Pure graphite
Ambient gas	Ar
Gas pressure	400 – 600 Torr
Gas flow rate	600 – 900 sccm
Furnace temperature	800 – 1100°C
Process time	120 min

with SEM and TEM. Figure 5.1 show SEM and TEM micrographs of the CNTs deposited at an Ar gas flow rate of 750 sccm. Their diameters are ranging between 20 and 50 nm,

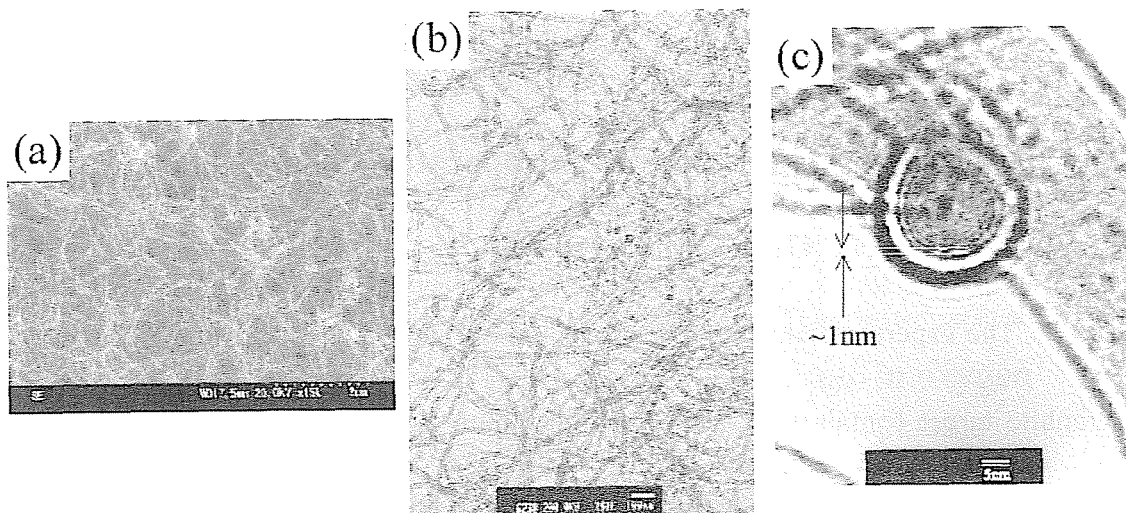


Figure 5.1. Micrographs of the CNTs deposited in area (3) by (a) SEM, (b) and (c) TEM.

Ar gas flow rate and laser repetition rate were 750 sccm and 10 Hz, respectively.

and the lengths are longer than 1  $\mu\text{m}$ . The magnified photograph in Figure 5.1 (c) shows that the tube is of a multi-walled structure with a several layers. Spacing between the layers was measured to be  $\sim 1$  nm.

#### 5.1.2 EDX analysis of CNTs

In this experiment, catalyst metal particles were not observed in the TEM micrographs except for the case as shown in Figure 5.2. Chemical components of the CNTs and catalysts were measured by an energy dispersive X-ray analyzer (EDX, H-700, JEOL. Ltd) and listed in Table 5.2. The contents of Ni and Y in the CNTs as shown in



Figure 5.2. TEM micrograph of CNTs. The white arrow indicates catalyst particle.

Table 5.2. EDX analyses of CNTs as shown in Figures 5.1 (b) and 5.2.

Elements	Chemical components	
	Figure 5.1 (b) (at. %)	Figure 5.2. (White arrow) (Weight %)
C	88.74	88.95
O	10.59	10.35
Ni	0.07	0.67
Y	0.00	0.02

Figure 5.1 (b) was below 0.1 at. % and  $\sim 0$  at. %, respectively. These values are significantly lower than those in the CNTs ( $\sim 4$ -5 at. %), which was obtained by an LA of 4.2 at. % Ni / 1 at. % Y / graphite target [89, 90]. However, it had been confirmed that when a pure graphite target was used, no CNT was synthesized.

To make sure how much contents of Ni and Y are in the Ni/Y/C target, SEM analyses of the target surface before and after LA were performed and shown in Figure 5.3. On the virgin surface as shown in Figure 5.3 (a), a lot of Ni/Y particles with a size of  $\sim 1 \mu\text{m}$  are embedded in graphite. Number density of the particles is roughly counted to be  $\sim 5 \times 10^6 \text{ cm}^{-2}$ . After LA of this target with a repetition rate of 10 Hz for 120 minutes, the target surface became a columnar shape as shown in Figure 5.3 (b). However, the most Ni/Y particles with a spherical shape remain. It is thought that the particles melted and then congealed on the target surface. The particle number density in Figure 5.3 (b) is



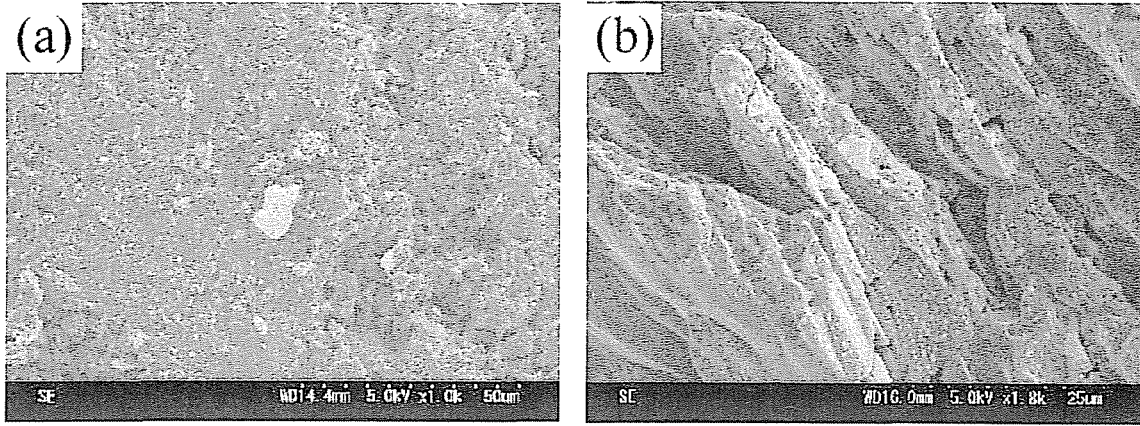


Figure 5.3. SEM micrographs of the surfaces of Ni/Y/C target: (a) before and (b) after LA at a repetition rate of 10 Hz for 120 minutes.

$\sim 5 \times 10^7 \text{ cm}^{-2}$ , which is about 10 times larger than that before the LA. These results suggest that the Ni and Y vaporized only partly by LA. It seems reasonable if we consider the difference of the optical reflectance  $r$  of Ni ( $r_{\text{Ni}} \sim 0.28$ ) at an incident light wavelength,  $\lambda = 248 \text{ nm}$  and graphite ( $r_{\text{g}} \sim 0.05$ ) at  $\lambda = 193 \text{ nm}$  [91]. In the case of Ni, the  $r_{\text{Ni}}$  at  $\lambda = 248 \text{ nm}$  [92] was referred because the value at  $\lambda = 193 \text{ nm}$  was not available. It is thought that the content of catalysts in this experiment could be less than that for optimal condition. However, even with small amount of Ni/Y, multi-walled CNT grew with a length of longer than  $1 \mu\text{m}$ .

### 5.1.3 Difference in Ablation Lasers and Laser Fluences

When a long-wavelength laser (e.g. Nd: YAG laser,  $\lambda = 532$  or  $1064 \text{ nm}$ ) is used for CNT growth in laser oven apparatus, most carbon soot is deposited on a collector located

behind a target due to Ar gas flow and thermophoretic force [27, 93]. On the contrary, in the present experiment, most carbon soot was deposited in area (3), in front of the target. This difference may be explained as follows. In the case of LA by ArF excimer laser, the  $C_n^+$  size  $n$  was mainly  $n = 1 - 3$  [12], and their kinetic energy reached  $\sim 80$  eV at a laser fluence of  $3 \text{ J/cm}^2$  [45]. Considering these facts, one presumes that the energetic  $C_n^+$  flew farther from the target, then was pushed back by the Ar gas flow, and finally deposited in area (3) [93]. However, the heavier  $C_n^+$ , but with small amount, was dragged backward by the Ar gas flow and deposited in area (4) – (6). The laser fluence affected also the initial kinetic energy of  $C_n^+$ .

#### 5.1.4 Raman Spectroscopy

Raman spectroscopy is a convenient and strong tool for analyses of CNT structures, for instance, the diameter, chirality and crystal quality. Raman spectra of the CNTs synthesized at Ar gas flow rates of 600, 750 and 900 sccm are shown in Figure 5.4. G and D peaks clearly appear. As the D mode is forbidden in perfect graphite, appearance of this peak shows that the CNT contains some defect in crystalline structure. At 750 sccm, the ratio of D peak intensity to G peak ( $I_D/I_G$ ) is  $\sim 1$ , which is the lowest among the CNTs and similar to that of multi-walled CNTs synthesized in a plasma enhanced CVD system [95].

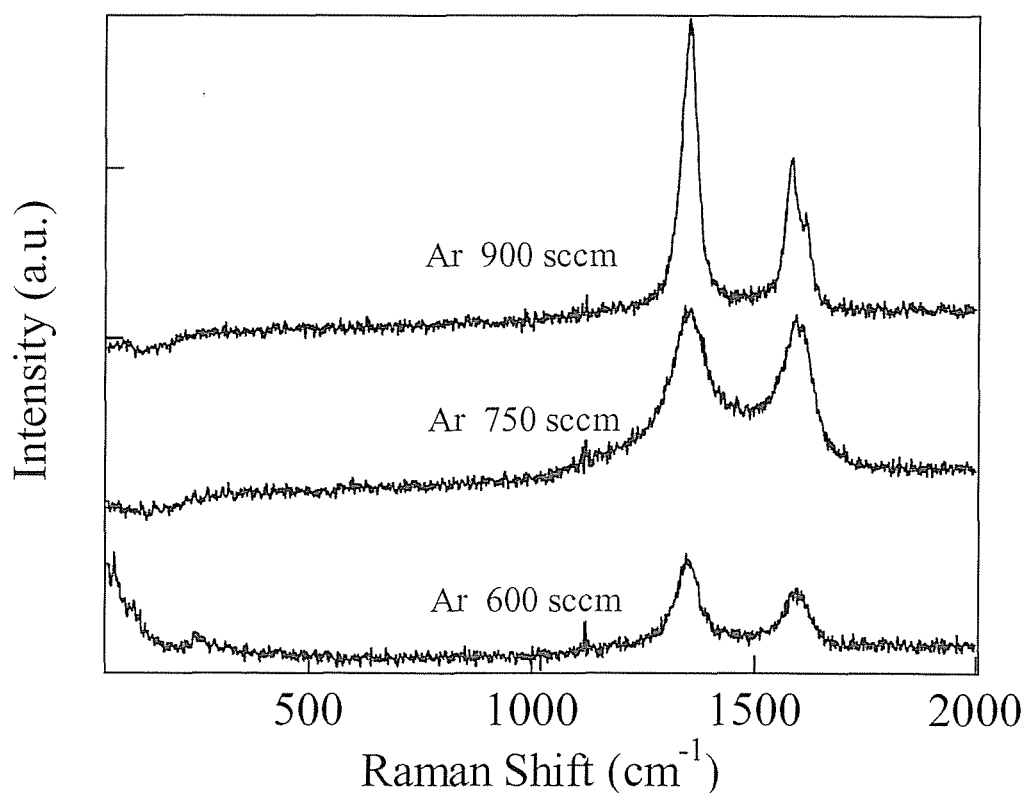


Figure 5.4. Raman spectra of the CNTs synthesized at different Ar gas flow rates. The laser repetition rate was 10 Hz.

#### 5.1.5 Effect of Laser Repetition Rate on CNT Length

When a laser repetition rate was increased, CNTs got longer. TEM micrographs of the CNTs obtained at the laser repetition rate of 50 Hz are shown in Figure 5.5. A relatively long ( $> 3 \mu\text{m}$ ) and straight CNT was obtained in area (3) as shown in Figure 5.5 (a). The CNT obtained in area (5) where furnace temperature  $T$  is estimated to be  $\sim 800^\circ\text{C}$  had a similar structure to that synthesized at the repetition rate of 10 Hz and deposited in area (3) ( $T = 1000^\circ\text{C}$ ) (see Figure 5.1 (b)).

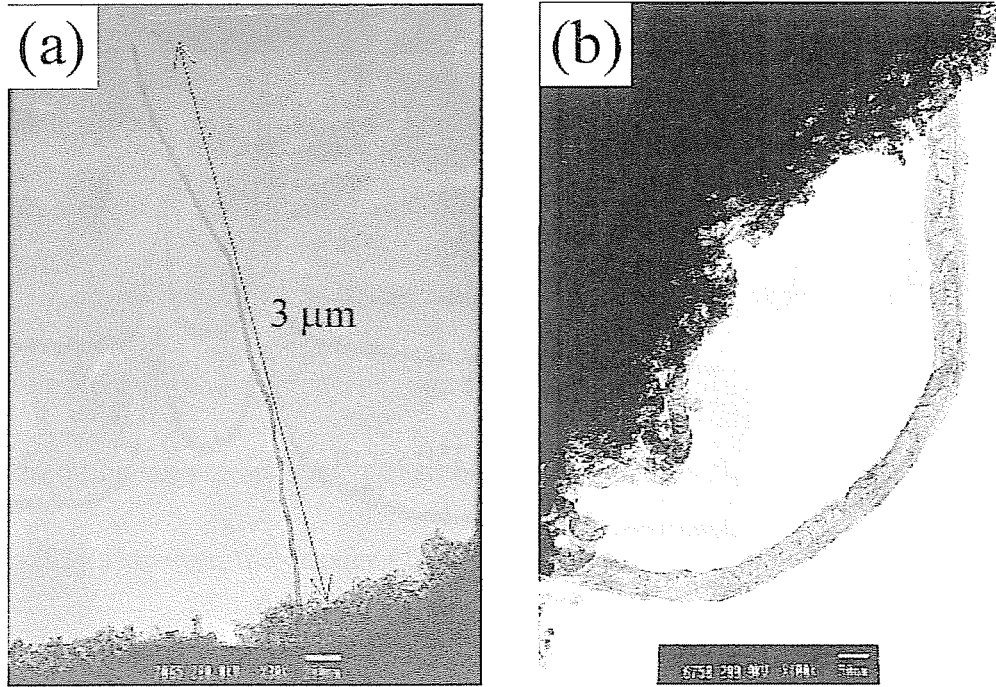


Figure 5.5. TEM micrographs of the CNTs deposited at a laser repetition rate of 50 Hz in two different areas, (a) area (3) and (b) area (5), where  $T$  is  $1000^{\circ}\text{C}$  and  $\sim 800^{\circ}\text{C}$ , respectively.

If it is assumed that the CNT growth mechanism in the present experiment is similar to that in the previous experiments by an Nd: YAG laser, it would be explained as follows. First, carbon and metal (Ni/Y) catalysts are vaporized from the Ni/Y/C target by ArF laser ablation and form high temperature plasma. Temperature of  $\text{C}_2$  vibration state in the plasma was  $\sim 6000^{\circ}\text{C}$ , when KrF excimer laser ( $\lambda = 248 \text{ nm}$ ) was used [96]. The plasma was gradually cooled down by the collision with Ar gas. Then, carbon clusters,  $\text{C}_n$  and metals are condensed to liquid-phase nanoparticles, and carbon atoms are finally separated out from the nanoparticles as forming CNTs when the temperature of nanoparticles

becomes below C-Ni eutectic temperature (1326°C) [94].

Puretzky, et al estimated the onset of CNT growth as ~2 ms after laser ablation and the growth rate of between ~0.6 and 5.1  $\mu\text{m/s}$  for their experimental condition [97]. By shortening the time interval between the laser shots (100 ms for a repetition rate of 10 Hz and 20 ms for 50 Hz),  $C_n$  and catalysts are continuously supplied. This would help to prolong CNTs. In the present experiment, area (3) may be an appropriate distance from the target to maintain  $T \sim 1000^\circ\text{C}$  and continuous supply of the  $C_n$  and catalysts. Consequently, most CNT was mainly deposited in this area.

## 5.2 CNF Growth on Metal-Catalyzed Substrates

### 5.2.1 Observation of CNFs by SEM and TEM

The experimental setup and procedure are described in Section 2.2. Table 5.3 shows the experimental condition. SEM micrographs of the CNFs on Ni/SiO<sub>2</sub>/Si and Fe/SiO<sub>2</sub>/Si substrates placed at -30 mm are shown in Figure 5.6. Figure 5.7 shows a TEM micrograph of CNFs grown in this experimental setup. The diameters of CNFs on Ni/SiO<sub>2</sub>/Si and Fe/SiO<sub>2</sub>/Si substrates were ~150 nm and ~80 nm, respectively. The number density of CNFs on Ni/SiO<sub>2</sub>/Si substrate was ~2 times higher than that on Fe/SiO<sub>2</sub>/Si one. The both CNFs were > 100  $\mu\text{m}$  in length. Diameter of the present CNFs is a few times larger than the CNTs obtained in a gas-phase as described in Section 5.1 (~20 - 50 nm). These CNFs were obtained from the Ni/Y/C target. However, the CNFs

Table 5.3. The experimental condition for CNF growth.

Base pressure	$1 \times 10^{-3}$ Torr
Ablation laser	ArF excimer laser ( $\lambda = 193$ nm, pulse duration=20 ns)
Laser fluence	2 J/cm <sup>2</sup>
Repetition rate	50 Hz
Target	Ni (1 at. %)/Y/C, Pure graphite
Ambient gas	Ar
Gas pressure	500 Torr
Gas flow rate	600 sccm
Furnace temperature	1100°C
Catalyst	Fe (with a thickness of 300 nm), Ni (1-350 nm)
Substrate	Si with a 200-nm SiO <sub>2</sub> layer (SiO <sub>2</sub> /Si)
Substrate position	+30 mm, -30 mm and -60 mm from the target surface (+: upstream of the Ar gas flow, -: indicates downstream)
Process time	120 min

grown did not show any difference when a pure graphite target was used.

The structure of CNFs grown is investigated by TEM as shown in Figure 5.7. The CNFs seem to be amorphous unlike CNTs, which is of tubular structure with graphene layers.

In CVD growth of CNTs, it is essential to control the diameters of CNTs by catalyst film thickness because film thickness is strongly correlated with sizes of catalytic nanoparticles, which are encapsulated in CNTs [98]. Thin Ni films with a range of thicknesses 1 – 350 nm were tested in this experiment. The diameters of CNFs

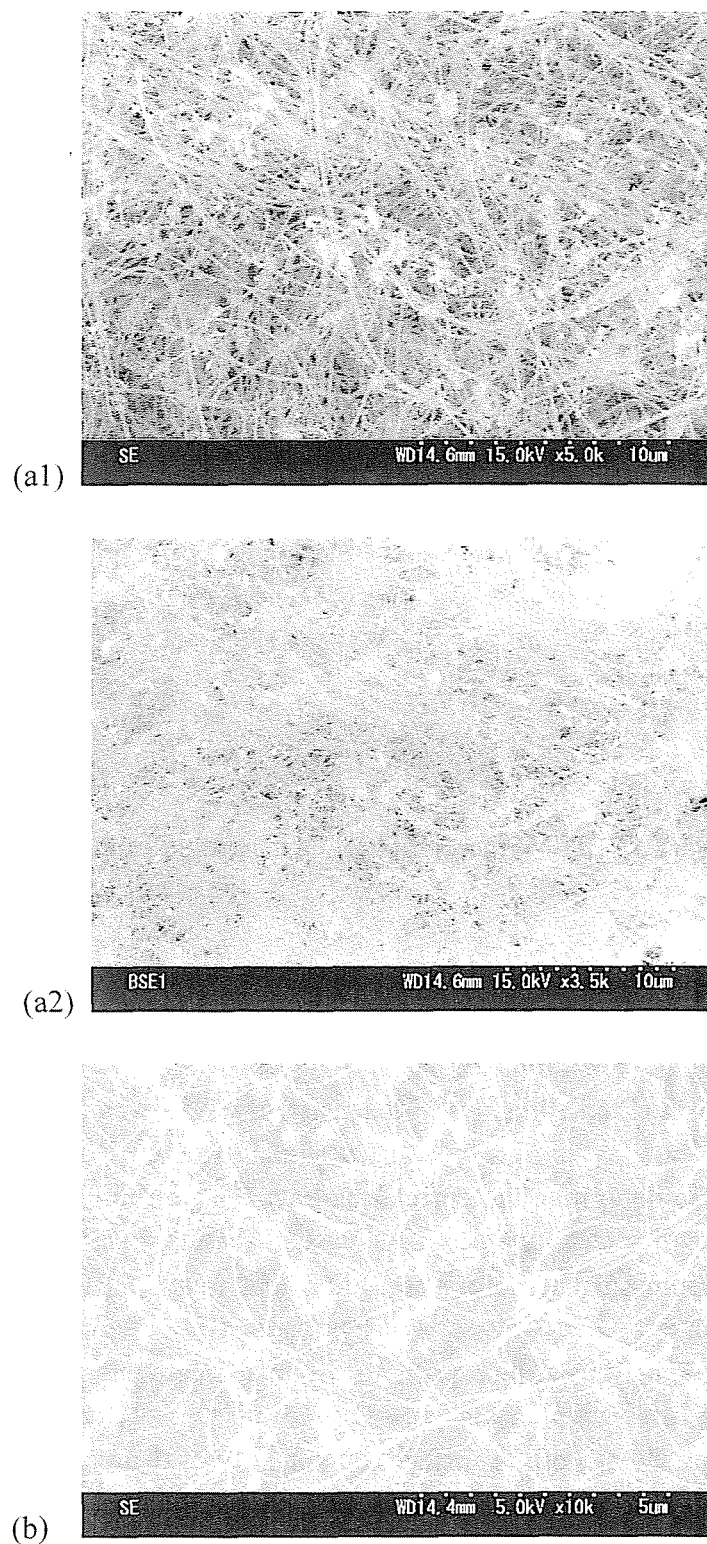


Figure 5.6. SEM micrographs of the CNFs grown on (a) Ni/SiO<sub>2</sub>/Si and (b) Fe/SiO<sub>2</sub>/Si substrates. (a2) backscattered electron image of (a1). The thicknesses of Ni and Fe films are 350 nm and 300 nm, respectively. The Ni/Y/C target was used.



Figure 5.7. TEM micrograph of CNFs grown from Pd/Ni catalyst.

decreased with a decrease in film thickness as shown in Figure 5.8. CNFs were grown on 1-nm and 3-nm-thick Ni films, but the density of CNFs was too low and the uniformity was not good. To determine the correlation between film thickness and particle size, the 5-nm-thick Ni film surface before and after heat treatment ( $T = 1100^{\circ}\text{C}$ ) was scanned with an AFM. The film surface prior to the heat treatment was quite smooth, and the root-mean square (RMS) of the surface roughness was  $\sim 1$  nm. The RMS increased to  $\sim 40$  nm after the heat treatment. It is speculated that metal nanoparticles are formed by the migration and aggregation of metal atoms deposited on substrate. An Ni film thickness of 3 nm was thought to be too small for the formation of metal nanoparticles with sufficient



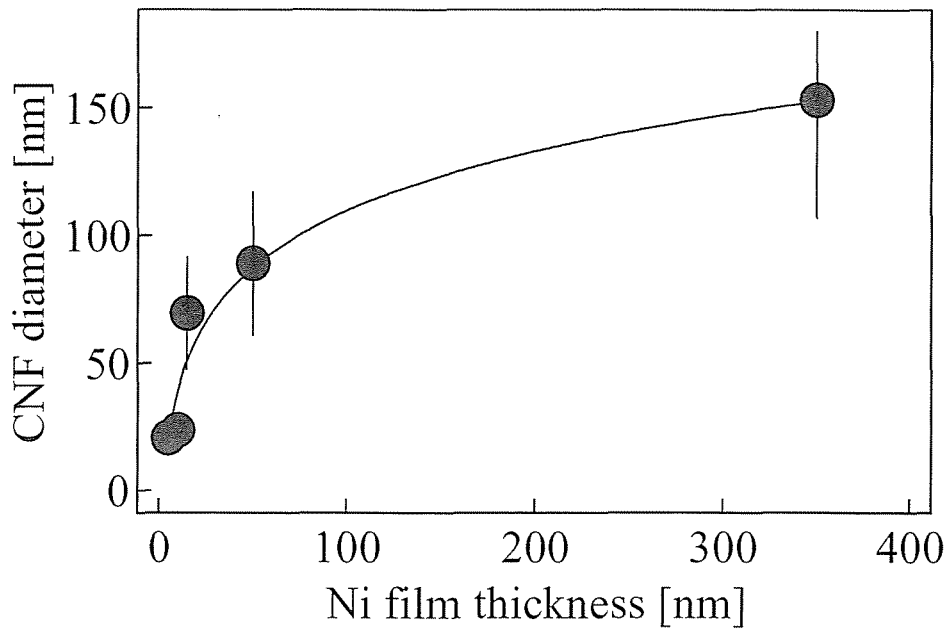


Figure 5.8. Dependence of CNF diameter of Ni film thickness.

density in the present experiment.

CNT growth experiment was performed with a  $T$  range of 800 – 1100°C, and CNTs could be grown only at  $T \geq 1000^\circ\text{C}$ . Below this temperature, almost all of the deposits on substrates were amorphous carbon nanoparticles.

Figure 5.6 (a2) clearly shows that the CNFs contain catalyst particles in their tips. However, the CNTs on Fe/SiO<sub>2</sub>/Si substrate shown in Figure 5.6 (b) do not seem to hold them. There are some differences in the diameter, the number density and the shape of the tip of CNFs grown on between Ni/SiO<sub>2</sub>/Si and Fe/SiO<sub>2</sub>/Si substrates. These results may indicate that the catalyst effect of Ni and Fe on CNF growth is different. In the case of plasma CVD process using C<sub>2</sub>H<sub>2</sub> gas, it was reported that Ni catalyst yielded higher growth rate and the larger diameter of CNT than Fe did [98, 99]. Lee, et al explained this

difference by the fact that the diffusion coefficient of carbon in bulk Ni ( $1.6 \times 10^{-7} \text{ cm}^2\text{s}^{-1}$ ) is higher than that in Fe ( $1.1 \times 10^{-7} \text{ cm}^2\text{s}^{-1}$ ) [99].

Though the substrates were placed at three different positions, CNFs were grown mainly at the edge of the substrate placed only at  $-30 \text{ mm}$ . As Sen, et al and Puretzky, et al observed dynamics of carbon clusters ( $C_n$ ) generated from a metal-catalyzed graphite target by laser ablation,  $C_n$  firstly goes against Ar gas flow, then was pushed back, and finally deposited at certain position downstream the target as forming CNT [93, 97]. Taking into account these observations, the present CNF growth process is speculated that ablated  $C_n$  firstly reached the substrate surface, and then dissolved into the catalytic metal, and CNF was finally separated from the saturated metal particle [39]. The position at  $-30 \text{ mm}$  may be appropriate to have enough carbon feedstock from the graphite ablation plume.

### 5.2.2 Optical Emission Spectroscopy of Ablation Plume of Ni/Y/C Target

To investigate ablated species from Ni/Y/C target, optical emission spectroscopy was performed in the Ar gas pressures of  $0 - 600 \text{ Torr}$  at room temperature (RT) and  $1000^\circ\text{C}$  as shown in Figure 5.9. The background emission from the electric furnace was removed. The emission band of  $C_2$  ( $A^3\Pi_g$ ) and the emission lines of CII ( $^2P^\circ$ ), YI ( $y^2D_{3/2}^\circ$ ), YII ( $z^1D_2^\circ$ ) and ArI ( $4p^1[1/2, 3/2], 4p[1/2, 3/2, 5/2]$ ) were detected [50, 51, 100]. The wide bands of  $C_3$  ( $\tilde{A}^1\Pi_u$ ) were detected at  $405 \text{ nm}$ ,  $410 \text{ nm}$  and  $431 \text{ nm}$  [50, 100]. Ni

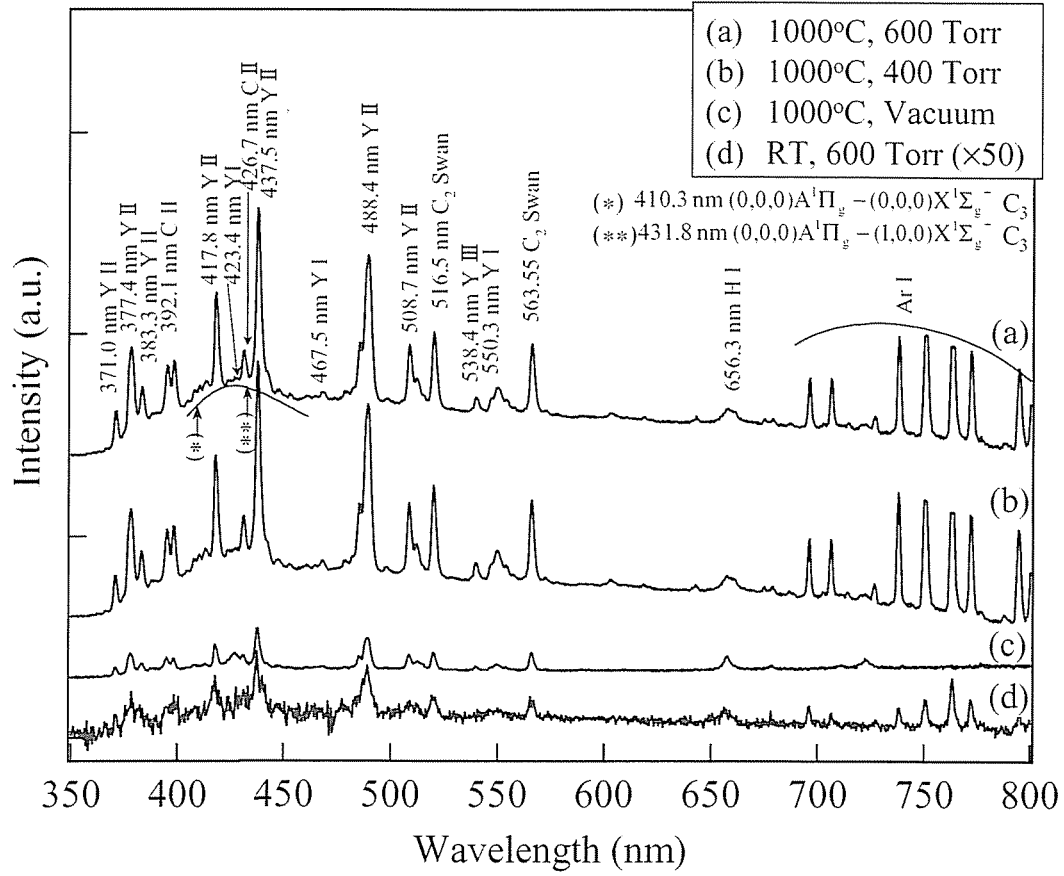


Figure 5.9. Optical emission spectra of the laser ablation plume of Ni/Y/C target in Ar gas at a pressure range of 0 – 600 Torr at  $T = \text{RT}$  and 1000°C.

was not observed in this spectrum since the intense lines of Ni lie in UV region [50]. The emission intensity of  $C_3$  ( $\tilde{A}^1\Pi_u$ ) increased as  $p_{\text{Ar}}$  and  $T$  increased. For the atomic and ionic emission lines of C, the emission intensity at 1000°C was  $\sim 100$  times higher than that at room temperature, however, the structure in the spectrum did not change. The  $C_3$  ( $\tilde{A}^1\Pi_u$ ) emission bands could give information about the formation of carbon clusters in the ablation plume.

## Chapter 6

### Conclusions

In this thesis, laser ablation of graphite assisted with RF plasma was used for carbon nanomaterial processing, such as carbon nanoparticles, amorphous carbon films. Growth of carbon nanotubes and nanofibers was achieved by the present ArF excimer laser ablation of graphite. In this chapter, the results obtained in this study are summarized.

- (1) Current waveform of the laser ablation plume was measured by an oscilloscope. It was shown that “fast” and “slow” waveforms were observed, which originate from electrons and positive carbon ions ( $C_n^+$ ), respectively. The velocity of electrons was measured to be  $\sim 2 \times 10^5$  m/sec and 20 times higher than that of  $C_n^+$ .
- (2) Optical emission spectra of the laser ablation plume in vacuum, Ar gas and Ar plasma were measured by a photonic multichannel analyzer. The spectra obtained in the Ar gas and plasma showed the emission lines of Ar atoms and ions as well as those of carbon atoms, ions and molecules. The electron temperature of ablation plume was estimated from the emission line intensities. It was confirmed that the plasma raised the electron temperature of ablation plume.
- (3) Amorphous carbon particles were deposited on silicon substrates by gas-phase and

plasma-assisted pulsed laser depositions at Ar gas pressures of 1 – 1600 mTorr. The particle size obtained in the Ar gas increased with the power of 1/8 as Ar gas pressure increased, and that prepared in the Ar plasma was 1.5 times larger than the case in the Ar gas. The carbon (1s) XPS spectra showed that formation of the particles could be, qualitatively, explained by a “sub-plantation model”. The  $sp^3/sp^2$  carbon ratio decreased monotonously with an increase of particle size, and that the  $sp^3/sp^2$  ratio obtained in the Ar plasma was larger than that in the Ar gas.

- (4) In Ar plasma-assisted pulsed laser deposition, it was confirmed that the number of micron-sized carbon droplets deposited on substrates decreased as RF plasma input power increased. This reduction could be explained by the negative charge on droplet and electrostatic force induced in a strong electric field in the plasma sheath.
- (5) Effects of the oxygen plasma and substrate temperature in oxygen plasma-assisted pulsed laser deposition on the content of  $sp^3$  bond in amorphous carbon films were examined. The film surface deposited in oxygen plasma of 0.4 mTorr was composed of nanometer-sized particles, although on the surface prepared in oxygen gas, particles with diameters of approximately 300 nm were grown. The maximum  $sp^3$  content of the film was 58% in the oxygen plasma at  $T_{\text{sub}} = 410^\circ\text{C}$ , though the  $sp^3$  content deposited in vacuum and  $\text{O}_2$  gas decreased monotonically with the increase of  $T_{\text{sub}}$  below  $450^\circ\text{C}$ .
- (6) Multi-walled carbon nanotubes (CNTs) were successfully synthesized inside of a quartz

tube operating at 1000°C by a short-wavelength pulsed ArF laser ( $\lambda=193\text{nm}$ ) ablation. The CNT was confirmed to be multi-walled tubes (diameter =  $\sim 20\text{ nm}$  and length =  $\sim 1\text{ }\mu\text{m}$ ) by TEM and Raman spectroscopy. Catalytic Ni/Y particles were not seen among the CNTs in TEM images. However, EDX analysis showed a very low level of Ni ( $< 0.1\text{ at. \%}$ ), which is considerably lower than the Ni content produced by previous laser ablation techniques. It was also confirmed that when a catalyst free target was used, no CNT was generated by ArF laser ablation. Prolongation of the CNT by increasing the laser repetition rate up to 50 Hz was demonstrated.

- (7) By the laser ablation of graphite in a laser oven apparatus (laser-thermal chemical vapor deposition), carbon nanofibers (CNFs) were grown on Ni- and Fe-catalyzed  $\text{SiO}_2/\text{Si}$  substrates placed inside an alumina tube of the apparatus at operating temperature above 1000°C by feeding with carbon. The number density of CNTs obtained on Ni catalytic metal was higher than that on Fe catalytic metal. The diameter of CNTs was controlled by Ni film thickness.

## **Author's Publications Related to the Present Work**

- (1) Growth of carbon nanotubes on Fe or Ni-coated Si substrate by feeding with carbon from a graphite ablation plume, *Applied Physics A*, Vol. 79, pp. 1331-1333 (2004)
- (2) Preparation of carbon nanoparticles by a plasma assisted PLD method -size and binding energy-dependence on ambient gas pressure and plasma condition-, *Thin Solid Films*, Vol. 415, pp. 15-20 (2002)
- (3) Preparation of double layer film of boron and carbon by pulsed laser deposition, *Applied Surface Science*, Vol. 197-198, pp. 603-606 (2002)
- (4) Deposition of fine carbon particles using pulsed ArF laser ablation assisted by inductively coupled plasma, *Thin Solid Films*, Vol. 374, pp. 287-290 (2000)

## Bibliography

1. D.B. Chrisey and G.K. Hubler Eds., "Pulsed Laser Deposition of Thin Films", John Wiley & Sons, Inc. (1994).
2. D. Dijkkamp, T. Venkatesan, X.D. Wu, S.A. Shaheen, N. Jisrawi, Y.H. Min-Lee, W.L. McLean and M. Croft, "Preparation of Y-Ba-Cu oxide superconductor thin films using pulsed laser evaporation from high  $T_c$  bulk material", Appl. Phys. Lett., 51 (1987) 619-621.
3. H.W. Kroto, J.R. Heath, S.C. O'Brien, R.F. Curl, R.E. Smalley, "C-60-Buckminsterfullerene", Nature, 318 (1985) 162-163.
4. R.F. Curl and R.E. Smalley, "Fullerenes", Sci. Am., 265 (1991) 54-63.
5. C. Niu, Y.Z. Lu and C.M. Lieber, "Experimental realization of the covalent solid carbon nitride", Science, 261 (1993) 334-337.
6. J. Robertson, "Hard amorphous (diamond-like) carbons", Prog. Solid State Chem., 21 (1991) 199-333.
7. A.C. Ferrari and J. Robertson, "Interpretation of Raman spectra of disordered and amorphous carbon", Phys. Rev. B, 61 (2000) 14095-14107.
8. F. Qian, R.K. Singh, S.K. Dutta and P. P. Pronko, "Laser deposition of diamondlike carbon films at high intensities", Appl. Phys. Lett., 67 (1995) 3120-3122.
9. S. Aoqui, K. Ebihara and Y. Yamagata, "Diamond-like carbon film preparation and surface coatings of oxide superconducting and ferroelectric films", Carbon, 36 (1998) 591-594.
10. R. Silva, G.A.J. Amaratunga, J. Robertson and W. I. Milne Eds, "Amorphous Carbon—State of the Art", World Scientific, Singapore (1998).
11. C. Wang, A. Garcia, D.C. Ingram, M. Lake and M.E. Kordesch, "Cold Field-Emission from CVD Diamond Films Observed in Emission Electron-Microscopy", Electron. Lett., 27 (1991) 1459-1461.
12. J.J. Gaumet, A. Wakikusa, Y. Shimizu and Y. Tamori, "Energetics for Carbon Clusters Produced Directly by Laser Vaporization of Graphite –Dependence on Laser Power and Wavelength", J. Chem. Soc. Faraday Trans., 89 (1993) 1667-1670.
13. K. Yamamoto, Y. Koga, S. Fujiwara, F. Kokai and R.B. Heimann, "Dependence of the  $sp^3$  bond fraction on the laser wavelength in thin carbon films prepared by pulsed laser deposition", Appl. Phys. A, 66 (1998) 115-117.



14. P.T. Murray and D.T. Peeler, "Pulsed-Laser Deposition of Carbon-Films –Dependence of Film Properties on Laser Wavelength", J. Electron. Mater., 23 (1994) 855-859.
15. T. Yoshitake, T. Nishiyama, H. Aoki, K. Suizu, K. Takahashi and K. Nagayama, "Carbon Thin Films Prepared by Pulsed Laser Deposition", T. IEE Japan, 119-A (1999) 1147-1155 (in Japanese).
16. Y. Taki and O. Takai, "XPS structural characterization of hydrogenated amorphous carbon thin films prepared by shielded arc ion plating", Thin Solid Films, 316 (1998) 45-50.
17. R. Kalish, Y. Lifshitz, K. Nugent and S. Praver, "Thermal stability and relaxation in diamond-like-carbon. A Raman study of films with different  $sp^3$  fractions (ta-C to a-C)", Appl. Phys. Lett., 74 (1999) 2936-2938.
18. Y. Liou, R. Weimer, D. Knight and R. Messier, "Effect of oxygen in diamond deposition at low substrate temperatures", Appl. Phys. Lett., 56 (1990) 437-439.
19. P.K. Bachmann, D. Leers and D.U. Wiechert, "Post-depositional diamond etching", Diam. Relat. Mater., 2 (1993) 683.
20. P. Storer, Y.Q. Cai, S.A. Canney, S.A.C. Clark, A.S. Khiefets, I.E. McCarthy, S. Utteridge, M. Vos and E. Weigold, "Surface characterization of diamond-like amorphous carbon foils by (e, 2e) spectroscopy and transmission electron energy loss spectroscopy", J. Phys. D, 28 (1995) 2340.
21. T. Yoshitake, T. Nishiyama and K. Nagayama, "The role of hydrogen and oxygen gas in the growth of carbon thin films by pulsed laser deposition", Diamond Relat. Mater., 9 (2000) 689-692.
22. M. Yoshimoto, K. Yoshida, H. Maruta, Y. Hishitani, H. Koinuma, S. Nishio, M. Kakihana and T. Tachibana, "Epitaxial diamond growth on sapphire in an oxidizing environment", Nature, 399 (1999) 340-342.
23. T. Makimura, Y. Kunii and K. Murakami, "Light Emission from Nanometer-Sized Silicon Particles Fabricated by the Laser Ablation Method", Jpn. J. Appl. Phys., 35 (1996) 4780-4784.
24. T. Yoshida, S. Takeyama, Y. Yamada and K. Mutoh, "Nanometer-sized silicon crystallites prepared by excimer laser ablation in constant pressure inert gas", Appl. Phys. Lett., 68 (1996) 1772-1774.
25. Y. Yamada, N. Suzuki, T. Makino and T. Yoshida, "Stoichiometric indium oxide thin films prepared by pulsed laser deposition in pure inert background gas", J. Vac. Sci. Technol., A 18 (2000) 83-86.

26. T. Guo, P. Nikolaev, A. Thess, D.T. Colbert and R.E. Smalley, "Catalytic growth of single-walled nanotubes by laser vaporization", *Chem. Phys. Lett.*, 243 (1995) 49-54.
27. A. Thess, R. Lee, P. Nikolaev, H.J. Dai, P. Petit, J. Robert, C.H. Xu, Y.H. Lee, S.G. Kim, A.G. Rinzler, D.T. Colbert, G.E. Scuseria, D. Tomanek, J.E. Fischer and R.E. Smalley, "Crystalline Ropes of Metallic Carbon Nanotubes", *Science*, 273 (1996) 483-487.
28. T.J. Goodwin, V.J. Leppert, S.H. Risbud, I.M. Kennedy and H.W.H. Lee, "Synthesis of gallium nitride quantum dots through reactive laser ablation", *Appl. Phys. Lett.*, 70 (1997) 3122-3124.
29. D. Li, Y. Liu, H. Yang and S. Qian, "Femtosecond nonlinear optical properties of carbon nanoparticles", *Appl. Phys. Lett.*, 81 (2002) 2088-2090.
30. J. Yu, E.G. Wang and X.D. Bai, "Electron field emission from carbon nanoparticles prepared by microwave-plasma chemical-vapor deposition", *Appl. Phys. Lett.*, 78 (2001) 2226-2228.
31. M.P. Siegal, D.L. Overmyer, R.J. Kottenstette, D.R. Tallant and W.G. Yelton, "Nanoporous-carbon films for microsensor preconcentrators", *Appl. Phys. Lett.*, 80 (2002) 3940-3942.
32. G.X. Chen, M.H. Hong, Q. He, W.Z. Chen, H.I. Elim, W. Ji and T.C. Chong, "Formation, structure and nonlinear optical properties of carbon nanoparticles synthesized by pulsed laser ablation", *Appl. Phys. A*, 79 (2004) 1079-1082.
33. S. Iijima, "Helical microtubules of graphitic carbon", *Nature*, 354 (1991) 56-58.
34. S. Iijima and T. Ichihashi, "Single-shell carbon nanotubes of 1-nm diameter", *Nature*, 363 (1993) 603-605.
35. C.H. Olk and J.P. Heremans, "Scanning tunneling spectroscopy of carbon nanotubes", *J. Mater. Res.*, 9 (1994) 259-262.
36. M.S. Dresselhaus, G. Dresselhaus and Ph. Avouris Eds., "Carbon Nanotubes: Synthesis, Structure, Properties and Applications", Springer-Verlag Berlin Heidelberg (2001) pp. 5, 30-34, 391-420.
37. C. Journet, W.K. Maser, P. Bernier, A. Loiseau, M.L. Delachapelle, S. Lefrant, P. Deniard, R. Lee and J.E. Fischer, "Large-scale production of single-walled carbon nanotubes by the electric-arc technique", *Nature*, 388 (1997) 756-758.
38. J. Kong, A.M. Cassell and H. Dai, "Chemical vapor deposition of methane for single-walled carbon nanotubes", *Chem. Phys. Lett.*, 292 (1998) 567-574.

39. M. Endo, "The growth mechanism of vapor-grown carbon fibers", PhD thesis, University of Orleans, Orleans, France (1975) (in French).
40. M. Endo, PhD thesis, Nagoya University, Japan (1978) (in Japanese).
41. S. Iijima, "Direct observation of the tetrahedral bonding in graphitized carbon black by high resolution electron microscopy", *J. Cryst. Growth*, 50 (1980) 675-683.
42. A. Oberlin, M. Endo and T. Koyama, "High resolution electron microscope observations of graphitized carbon fibers", *Carbon*, 14 (1976) 133-135.
43. A. Oberlin, M. Endo and T. Koyama, "Filamentous growth of carbon through benzene decomposition", *J. Cryst. Growth*, 32 (1976) 335-349.
44. A.V. Melechko, V.I. Merkulov, T.E. McKnight, M.A. Guillorn, K.L. Klein, D.H. Lowndes and M.L. Simpson, "Vertically aligned carbon nanofibers and related structures: Controlled synthesis and directed assembly", *J. Appl. Phys.*, 97 (2005) 041301.
45. D.H. Lowndes, V.I. Merkulov, A.A. Puretzky, D.B. Geohegan, G.E. Jellison, Jr., C.M. Rouleau and T. Thundat, "Amorphous diamond films deposited by pulsed-laser ablation: The optimum carbon-ion kinetic energy and effects of laser wavelength", *Mat. Res. Soc. Symp. Proc.*, 526 (1998) 325-330.
46. S. Ohtsubo, T. Minamikawa, Y. Yonezawa, A. Morimoto and T. Shimizu, "Thermal Analysis of Target Surface in the Ba-Y-Cu-O Film Preparation by Laser Ablation Method", *Jpn. J. Appl. Phys.*, 29 (1990) L73-L76.
47. J. Muramoto, Y. Nakata, T. Okada and M. Maeda, "Observation of Nano-Particle Formation Process in a Laser-Ablated Plume Using Imaging Spectroscopy", *Jpn. J. Appl. Phys.*, 36 (1997) L563-L565.
48. F. Kokai and Y. Koga, "Time-of-flight mass spectrometric studies on the plume dynamics of laser ablation of graphite", *Nucl. Instr. and Meth. in Phys. Res. Sec. B*, 121 (1997) 387-391.
49. G. Koren and J.T.C. Yeh, "Emission spectra and etching of polymers and graphite irradiated by excimer lasers", *J. Appl. Phys.*, 56 (1984) 2120-2126.
50. NIST Atomic Spectra Database, <http://physics.nist.gov/PhysRefData/ASD/>
51. R.W.B. Pearse and A.G. Gaydon, "The identification of molecular spectra", 4<sup>th</sup> edition Chapman and Hall (1976) pp. 82-86.
52. B. Holzapfel, B. Roas, L. Schultz, P. Bauer and G. Saemann-Ischenko, "Off-axis laser deposition of  $\text{YBa}_2\text{Cu}_3\text{O}_{7-\delta}$  thin films", *Appl. Phys. Lett.*, 61 (1992) 3178-3180.

53. Scion Corporation (Scion Image for Windows),  
[http://www.scioncorp.com/pages/scion\\_image\\_windows.htm](http://www.scioncorp.com/pages/scion_image_windows.htm)
54. L. Boufendi and A. Bouchoule, "Particle nucleation and growth in a low-pressure argon-silane discharge", *Plasma Sources Sci. Technol.*, 3 (1994) 262-267.
55. Y. Watanabe, M. Shiratani, T. Fukuzawa, H. Kawasaki, Y. Ueda, S. Singh and H. Ohkura, "Contribution of short lifetime radicals to the growth of particles in SiH<sub>4</sub> high frequency discharges and the effects of particles on deposited films", *J. Vac. Sci. Technol.*, A 14 (1996) 995-1001.
56. C. Couteille, C. Hollenstein, J.-L. Dorier, P. Gay, W. Schwarzenbach, A. A. Howling, E. Bertran, G. Viera, R. Martins and A. Mararico, "Particle agglomeration study in rf silane plasmas: *In situ* study by polarization-sensitive laser light scattering", *J. Appl. Phys.*, 80 (1996) 2069-2078.
57. U. Kortshagen and U. Bhandarkar, "Modeling of particulate coagulation in low pressure plasmas", *Phys. Rev. E*, 60 (1999) 887-898.
58. Y. Watanabe, M. Shiratani, H. Kawasaki, S. Singh, T. Fukuzawa, Y. Ueda and H. Ohkura, "Growth processes of particles in high frequency silane plasmas", *J. Vac. Sci. Technol.*, A 14 (1996) 540-545.
59. M. Shiratani, T. Fukuzawa and Y. Watanabe, "Particle Growth Kinetics in Silane RF Discharges", *Jpn. J. Appl. Phys.*, 38 (1999) 4542-4549.
60. M. Shiratani, H. Kawasaki, T. Fukuzawa, T. Yoshioka, Y. Ueda, S. Singh and Y. Watanabe, "Simultaneous *in situ* measurements of properties of particulates in rf silane plasmas using a polarization-sensitive laser-light-scattering method", *J. Appl. Phys.*, 79 (1996) 104-109.
61. T. Makimura, Y. Kunii, N. Ono and K. Murakami, "Silicon nanoparticles embedded in SiO<sub>2</sub> films with visible photoluminescence", *Appl. Surf. Sci.*, 127-129 (1998) 388-392.
62. J. Ullmann, G. Schmidt and W. Scharff, "Diamond-like amorphous carbon films prepared by r.f. sputtering in argon", *Thin Solid Films*, 214 (1992) 35-43.
63. M.A. Lieberman, A.J. Lichtenberg, "Principles of plasma discharges and materials processing", Wiley (1994).
64. A. Homann, A. Melzer and A. Piel, "Measuring the charge on single particles by laser-excited resonances in plasma crystals", *Phys. Rev. E*, 59 (1999) R3835-R3838.
65. H. Kresten, H. Deutsch, G.M.W. Kroesen, "Charging of micro-particles in plasma-dust interaction", *International Journal of Mass Spectrometry*, 233 (2004) 51-60.

66. E.B. Tomme, D.A. Law, B.M. Annaratone, J.E. Allen, "Parabolic Plasma Sheath Potentials and their Implications for the Charge on Levitated Dust Particles", *Physical Review Letters*, 85 (2000) 2518-2521.
67. G.A. Hebner, M.E. Riley, "Measurement of attractive interactions produced by the ion wakefield in dusty plasmas using a constrained collision geometry", *Physical Review E*, 68 (2003) 046401.
68. D. Lubben, S.A. Barnett, K. Suzuki, S. Gorbatskin and J. E. Greene, "Laser-induced plasmas for primary ion deposition of epitaxial Ge and Si films", *J. Vac. Sci. Technol.*, B 3 (1985) 968-974.
69. D.B. Geohegan, "Imaging and blackbody emission spectra of particulates generated in the KrF-laser ablation of BN and YBa<sub>2</sub>Cu<sub>3</sub>O<sub>7-x</sub>", *Appl. Phys. Lett.*, 62 (1993) 1463-1465.
70. P. Merel, M. Tabbal, M. Chaker, S. Moisa and J. Margot, "Direct evaluation of the  $sp^3$  content in diamond-like-carbon films by XPS", *Appl. Surf. Sci.*, 136 (1998) 105-110.
71. J. Diaz, G. Paolicelli, S. Ferrer and F. Comin, "Separation of the  $sp^3$  and  $sp^2$  components in the C1s photoemission spectra of amorphous carbon films", *Phys. Rev. B*, 54 (1996) 8064-8069.
72. D.A. Shirley, "High-Resolution X-Ray Photoemission Spectrum of the Valence Bands of Gold", *Phys. Rev. B*, 5 (1972) 4709-4714.
73. V.I. Merkulov, D.H. Lowndes, G.E. Jellison, Jr., A.A. Puretzky and D.B. Geohegan, "Structure and optical properties of amorphous diamond films prepared by ArF laser ablation as a function of carbon ion kinetic energy", *Appl. Phys. Lett.*, 73 (1998) 2591-2593.
74. Y. Lifshitz, S.R. Kasi and J.W. Rabalais, "Subplantation Model for Film Growth From Hyperthermal Species: Application to Diamond", *Phys. Rev. Lett.*, 62 (1989) 1290-1293.
75. Y. Lifshitz, S.R. Kasi and J.W. Rabalais, "Subplantation model for film growth from hyperthermal species", *Phys. Rev. B*, 41 (1990) 10468-10480.
76. J. Robertson, "Deposition mechanisms for promoting  $sp^3$  bonding in diamond-like carbon", *Diamond Relat. Mater.*, 2 (1993) 984-989.
77. M. Chhowalla, A.C. Ferrari, J. Robertson and G.A.J. Amaratunga, "Evolution of  $sp^2$  bonding with deposition temperature in tetrahedral amorphous carbon studied by Raman spectroscopy", *Appl. Phys. Lett.*, 76 (2000) 1419-1421.

78. F. Tuinstra and J.L. Koenig, "Raman Spectrum of Graphite", *J. Chem. Phys.*, 53 (1970) 1126-1130.
79. R.J. Nemanich and S.A. Solin, "First- and second-order Raman scattering from finite-size crystals of graphite", *Phys. Rev. B*, 20 (1979) 392-401.
80. P. Lespade, R. Al-Jishi and M.S. Dresselhaus, "Model for Raman scattering from incompletely graphitized carbons", *Carbon*, 20 (1982) 427-431.
81. P. Lespade, A. Marchard, M. Couzi and F. Cruege, "Caracterisation de materiaux carbonés par microspectrometrie Raman", *Carbon*, 22 (1984) 375-385 (in French).
82. D.G. McCulloch, S. Praver and A. Hoffman, "Structural investigation of xenon-ion-beam-irradiated glassy carbon", *Phys. Rev. B*, 50 (1994) 5905-5917.
83. T. Yoshitake, T. Nishiyama, H. Aoki, K. Suizu, K. Takahashi and K. Nagayama, "The effects of substrate temperature and laser wavelength on the formation of carbon thin films by pulsed laser deposition", *Diamond Relat. Mater.*, 8 (1999) 463-467.
84. J. Robertson, J. Gerber, S. Sattel, M. Weiler, K. Jung and H. Ehrhardt, "Mechanism of bias-enhanced nucleation of diamond on Si", *Appl. Phys. Lett.*, 66 (1995) 3287-3289.
85. M. Jelínek, V. Olšan, L. Soukup, D. Charalabidis, E. Hontzopoulos and E. Georgiou, "Some properties of carbon films deposited by laser ablation", *Diamond Relat. Mater.*, 3 (1994) 1128-1131.
86. M. Tabbal, P. Mérel, M. Chaker, M.A. El Khakani, E.G. Herbert, B.N. Lucas and M.E. O'Hern, "Synthesis of diamond-like-carbon coatings by pulsed laser deposition: optimization of process parameters", *Surf. Coat. Tech.*, 116-119 (1999) 452-455.
87. E.J.H. Collart, J.A.G. Baggerman and R.J. Visser, "On the role of atomic oxygen in the etching of organic polymers in a radio-frequency oxygen discharge", *J. Appl. Phys.*, 78 (1995) 47-54.
88. N. Braidý, M.A. El Khakani and G.A. Botton, "Single-wall carbon nanotubes synthesis by means of UV laser vaporization", *Chem. Phys. Lett.*, 354 (2002) 88-92.
89. W.K. Maser, A.M. Benito, E. Muñoz, G.M. de Val, M.T. Martínez, Á. Larrea and G.F. de la Fuente, "Production of carbon nanotubes by CO<sub>2</sub>-laser evaporation of various carbonaceous feedstock materials", *Nanotechnology*, 12 (2001) 147-151.
90. P.C. Eklund, B.K. Pradhan, U.J. Kim, Q. Xiong, J.E. Fischer, A.D. Friedman, B.C. Holloway, K. Jordan and M.W. Smith, "Large-Scale Production of Single-Walled Carbon Nanotubes Using Ultrafast Pulses from a Free Electron Laser", *Nano Lett.*, 2 (2002) 561-566.

91. E.A. Taft and H.R. Philipp, "Optical Properties of Graphite", *Phys. Rev.*, 138 (1965) A197-A202.
92. X. Xu, G. Chen and K.H. Song, "Experimental and numerical investigation of heat transfer and phase change phenomena during excimer laser interaction with nickel", *Int. J. Heat Mass Transfer*, 42 (1999) 1371-1382.
93. R. Sen, Y. Ohtsuka, T. Ishigaki, D. Kasuya, S. Suzuki, H. Kataura and Y. Achiba, "Time period for the growth of single-wall carbon nanotubes in the laser ablation process: evidence from gas dynamic studies and time resolved imaging", *Chem. Phys. Lett.*, 332 (2000) 467-473.
94. H. Kataura, Y. Kumazawa, Y. Maniwa, Y. Ohtsuka, R. Sen, S. Suzuki and Y. Achiba, "Diameter control of single-walled carbon nanotubes", *Carbon*, 38 (2000) 1691-1697.
95. M. Sveningsson, R.-E. Morjan, O.A. Nerushev, Y. Sato, J. Backstrom, E.E.B. Campbell and F. Rohmund, "Raman spectroscopy and field-emission properties of CVD-grown carbon-nanotube films", *Appl. Phys. A*, 73 (2001) 409-418.
96. Y. Yamagata, A. Sharma, J. Narayan, R.M. Mayo, J.W. Newman and K. Ebihara, "Optical emission study of ablation plasma plume in the preparation of diamond-like carbon films by KrF excimer laser", *J. Appl. Phys.*, 86 (1999) 4154-4159.
97. A.A. Puretzky, D.B. Geohegan, H. Schittenhelm, X. Fan and M.A. Guillorn, "Time-resolved diagnostics of single wall carbon nanotube synthesis by laser vaporization", *Appl. Surf. Sci.*, 197-198 (2002) 552-562.
98. Z.P. Huang, D.Z. Wang, J.G. Wen, M. Sennett, H. Gibson and Z.F. Ren, "Effect of nickel, iron and cobalt on growth of aligned carbon nanotubes", *Appl. Phys. A.*, 74 (2002) 387-391.
99. C.J. Lee, J. Park and J.A. Yu, "Catalyst effect on carbon nanotubes synthesized by thermal chemical vapor deposition", *Chem. Phys. Lett.*, 360 (2002) 250-255.
100. I. Čermák, M. Förderer, I. Čermáková, S. Kalhofer, H. Stopka-Ebeler, G. Monninger and W. Krätschmer, "Laser-induced emission spectroscopy of matrix-isolated carbon molecules: Experimental setup and new results on C<sub>3</sub>", *J. Chem. Phys.*, 108 (1998) 10129-10142.